

©2015

Rut Rivera-Beltrán

ALL RIGHTS RESERVED

BISMUTH FERRITE BASED THIN FILMS, NANOFIBERS, AND FIELD
EFFECT TRANSISTOR DEVICES

by

RUT RIVERA – BELTRAN

A Dissertation submitted to the

Graduate School-New Brunswick

Rutgers, The State University of New Jersey

In partial fulfillment of the requirements

For the degree of

Doctor of Philosophy

Graduate Program in Materials Science and Engineering

Written under the direction of

Prof. Ahmad Safari

And approved by

New Brunswick, New Jersey

January, 2015

ABSTRACT OF THE DISSERTATION

Bismuth Ferrite Based Thin Films, Nanofibers and Field Effect Transistor Devices

By RUT RIVERA – BELTRAN

Dissertation Director:

Prof. Ahmad Safari

In this research an attempt has been made to explore bismuth ferrite thin films with low leakage current and nanofibers with high photoconductivity. Thin films were deposited with pulsed laser deposition (PLD) method. An attempt has been made to develop thin films under different deposition parameters with following target compositions: i) $0.6\text{BiFeO}_3\text{-}0.4(\text{Bi}_{0.5}\text{K}_{0.5})\text{TiO}_3$ (BFO-BKT) and ii) bi-layered $0.88\text{Bi}_{0.5}\text{Na}_{0.5}\text{TiO}_3\text{-}0.08\text{Bi}_{0.5}\text{K}_{0.5}\text{TiO}_3\text{-}0.04\text{BaTiO}_3/\text{BiFeO}_3$ (BNT-BKT-BT/BFO). BFO-BKT thin film shows suppressed leakage current by about four orders of magnitude which in turn improve the ferroelectric and dielectric properties of the films. The optimum remnant polarization is $19\text{ }\mu\text{C.cm}^{-2}$ at the oxygen partial pressure of 300 mtorr. The BNT-BKT-BT/BFO bi-layered thin films exhibited ferroelectric behavior as: $P_r = 22.0\text{ }\mu\text{C.cm}^{-2}$, $E_c = 100\text{ kV.cm}^{-1}$ and $\epsilon_r = 140$. The leakage current of bi-layered thin films have been reduced two orders of magnitude compare to un-doped bismuth ferrite.

Bismuth ferrite nanofibers were developed by electrospinning technique and its electronic properties such as photoconductivity and field effect transistor performance

were investigated extensively. Nanofibers were deposited by electrospinning of sol-gel solution on SiO₂/Si substrate at driving voltage of 10 kV followed by heat treatment at 550 °C for 2 hours. The composition analysis through energy dispersive detector and electron energy loss spectroscopy revealed the heterogeneous nature of the composition with Bi rich and Fe deficient regions. X-ray photoelectron spectroscopy results confirmed the combination of Fe³⁺ and Fe²⁺ valence state in the fibers. The photoresponse result is almost hundred times higher for a fiber of 40 nm diameter compared to a fiber with 100 nm diameter. This effect is described by a size dependent surface recombination mechanism. A single and multiple BFO nanofibers field effect transistors devices were fabricated and characterized. Bismuth ferrite FET behaves as p-type semiconductor. The carrier mobility for a single nanofiber FET was found as 0.2 cm²/V.s at 100 V driving voltage, while the carrier mobility of multiple nanofibers FET was maintained at 10 V driving voltage.

The results of this study present the versatility of BFO in the form of thin films and nanofibers for different electronic applications such as ferroelectric memories, transistor and light sensor.

Acknowledgments

First, I would like to thank God for allowing me to reach this point in my career and for giving me the strength to succeed. “God, thank you for always strength my inner man to overcome the most challenge situations and obstacles ”. I would also like to thank my advisor, Prof. Safari for not only being a great mentor but a father, mother, brother and even more than a friend. Working in his group gave me the freedom and support to follow my curiosity and develop new ideas in my project. I would also like to express my gratitude to my thesis committee members: Prof. Chhowalla, Prof. Klein and Dr. Abazari. Thanks to all of them for the guidance and invaluable comments to complete this task. Many thanks to Dr. Wielunski and Dr. Yakshinskiy for helping with RBS measurements and data analysis, to Dr. Tom Emge for XRD analysis in the Chemistry Department, Mahsa Sina and Rajesh Kappera for TEM imaging and device characterization respectively.

Once I moved to Rutgers, far from my family and love ones a new life began. Many months of loneliness, tears and very tough times occurred. It was hard to stand, to go further but God sent me very important people to take care of me during the valley. Mercedes the MSE building janitor, being the only Spanish speaking person, close to my culture, took care of all my needs in the building. Even in moments when my tears could not be stopped, she was present to encourage and make me strong. Mehdi, Elaheh, Hulya, Berra, Cecilia, Damien you are great friends, and classmates, I will appreciate the memorable moments we shared. To all my friends from Puerto Rico here, at Rutgers, especially to Mayda and Ernesto; thank you for your friendship. Yeslin, I appreciate your

friendship very much and will keep our relationship in my heart throughout the years. Thank you for the phone calls, encouraging words, trust and confidence.

To my family-parents, brothers, grandparents, cousins and uncles... thanks to all of you for the motivation and for believing in me. To my fiancé, friend and soul-mate in the far distance for three years and now my husband, Heraldo, thank you for standing beside me. It was tough to be far from each other but in the midst of the difficulties, in the good and bad times, you always found the way to express your love and care. I love you, because you love me! Thank you because you gave the best of yourself to make me feel strong, happy and loved all the time. Now you are here to finish this race along with me and appreciate all what you have done.

Finally, and most important, I would like to dedicate this thesis to my Parents, Iris and José. Being the youngest of three siblings and the only girl put me in a position to develop a closer relationship and bond with them. Thank you for respecting me, for being my number one fan, for believing me. Even though it was hard for you when I decided to move from home, you always supported and guided me to achieve the best in my career. I still remember doing Skype with Mom, while I was studying, after leaving the lab at one o'clock in the morning and you were there to walk me home through the phone. You always have been there for me, never complaining about the late hours, the lack of sleep or anything. I may felt Dad was not phone-calling so often, but he will be aware of what was happening. At the right moment he called and says the right words to make me feel better and encourage me to keep going forward. Dad always had the love and wisdom to touch my heart and give me the peace I was looking for. Thank you for being present in each step of my life and career. **Love you Mom & Dad!**

Table of Contents

ABSTRACT	ii
ACKNOWLEDGEMENTS	iv
TABLE OF CONTENTS	vi
LIST OF FIGURES	x
LIST OF TABLES	xix
1 Research Objectives and Scope of the Dissertation	
1.1 Statement of the problem	1
1.2 Objectives	4
1.3 Thesis organization	5
1.4 References	7
2 Introduction and Background	
2.1 Introduction	8
2.2 Dielectric materials	9
2.3 Piezoelectricity	13
2.4 Ferroelectric materials	15
2.5 Ferromagnetism.....	21
2.6 Multiferroic phenomenon and materials	24
2.7 Semiconductor materials	27
2.8 Summary	35
2.9 References.....	36

3 Literature Review

3.1 Introduction	37
3.2 Bismuth ferrite	38
3.3 Bismuth ferrite nanostructures	44
3.3.1 Zero dimension (0D, Nanoparticles)	46
3.3.2 One dimension (1D, Nanowires, Nanotubes)	49
3.3.3 Two dimension (2D, Thin films)	52
3.4 Summary	62
3.5 References	63

4 Characterization and Equipment Tools

4.1 Introduction	66
4.2 X-ray diffraction	67
4.3 Rutherford backscattering spectrometry	70
4.4 Raman spectroscopy	72
4.5 Electron microscope: transmission electron microscope and scanning electron microscope	76
4.6 Electron energy loss spectroscopy	79
4.7 Electrical Characterization	81
4.7.1 Current vs voltage & current vs time	82
4.7.2 Ferroelectric and dielectric measurements	83
4.8 Summary	83
4.9 References	84

5 Bismuth Ferrite Thin Films by Sol-Gel

5.1 Introduction	94
5.2 Experimental procedure	95
5.3 Results and discussion	97
5.4 Summary	105
5.5 References	106

6 Bismuth Ferrite Thin Films by Pulsed Laser Deposition

6.1 Introduction	99
6.2 Experimental procedure	100
6.2.1 Powder and target preparation	100
6.2.2 Laser deposition system	103
6.2.3 Pulsed laser deposition standard procedure	104
6.2.4 Deposition of bottom electrode	107
6.2.5 Deposition of top electrode	107
6.3 Bismuth ferrite based thin films	108
6.3.1 Bismuth ferrite	108
6.3.2 Effect of oxygen pressure on $0.6\text{BiFeO}_3\text{-}0.4(\text{Bi}_{0.5}\text{K}_{0.5})\text{TiO}_3$	111
6.3.3 $\text{BiFeO}_3/(\text{Bi}_{0.5}\text{Na}_{0.5})\text{TiO}_3\text{-(Bi}_{0.5}\text{K}_{0.5})\text{TiO}_3\text{-BaTiO}_3$ bi-layered	122
6.3.4 Summary	127
6.3.5 References	128

7	Bismuth Ferrite Nanofibers by Electrospinning	
7.1	Introduction	130
7.2	Experimental procedure	131
7.2.1	Electrospinning setup	131
7.2.2	Standard operation procedure	133
7.2.3	Sol gel solution preparation	135
7.3	Fabrication and characterization of bismuth ferrite nanofibers	136
7.3.1	Optimization of solution and processing conditions	137
7.3.2	Characterization of bismuth ferrite nanofibers	140
7.3.3	Nanofibers with different diameters	144
7.3.3.1	Grain size	147
7.3.3.2	Valence state	148
7.3.3.3	Chemical composition	149
7.4	Electrical properties of BFO nanofibers	152
7.4.1	Single nanofibers	152
7.4.2	Size dependent on the photoconductivity of multiple-nanofibers	154
7.5	Bismuth ferrite field effect transistor devices with single and multiple nanofibers devices	159
7.6	Summary	163
7.7	References	164
8	Conclusions	166
9	Suggestion for future work	171

List of Figures

Figure 2.1 A parallel plate capacitor (a) when a vacuum is present and (b) when a dielectric material is inserted.....	10
Figure 2.2 Polarization mechanisms leading to dielectric polarization/displacement....	11
Figure 2.3 Variation of dielectric constant with frequency of alternating electric field. Electronic, ionic, orientation and space charge contributions to the dielectric constant are indicated	12
Figure 2.4 The crystal structure of barium titanate (perovskite structure). (a) Above Curie temperature the cell is cubic and (b) below the Curie temperature is tetragonal with Ba^{2+} and Ti^{4+} ions shifted relative to the O^{2-} ions	16
Figure 2.5 Temperature dependence of the dielectric constant in barium titanate.....	17
Figure 2.6 Barium titanate phase transition below T_C	17
Figure 2.7 Typical hysteresis loop	19
Figure 2.8 (a) ionic displacement in two 180° ferroelectric domains, (b) domain structure is showing several 180° domains of different sizes and (c) 180° domain wall with a width of $\sim 0.2 - 0.3 \text{ nm}$	20
Figure 2.9 Order arrangements of electron spins	21
Figure 2.10 A magnetization hysteresis loop for a ferromagnetic material. Insets: domain structures at various magnetic fields	22

Figure 2.11 The origin of ferromagnetic domains. (a) single domain as a consequence of the magnetic “poles” formed on the surfaces, (b) the magnetic is energy is reduced approximately one half by dividing the crystal into two domains magnetized in opposite directions, (c) with N domains the magnetic energy is reduced to approximately 1/N of the magnetic energy of a single domain, (d) and (e) in such domain arrangement the magnetic energy is zero	23
Figure 2.12 Multiferroic combined the properties of ferroelectrics and magnets	24
Figure 2.13 The energy band structure for (a) metal, (b) insulator and (c) semiconductor	28
Figure 2.14 Extrinsic semiconductor (a) n-type: an impurity atom such as phosphorus with five valence electrons may substitute for a silicon atom resulting in an extra bonding electron, (b) p-type: an impurity atom such as boron with three valence electrons may substitute for silicon atom resulting in a deficiency of a one valence electron	30
Figure 2.15 For a <i>p-n</i> rectifying junction representation of electron and hole distributions for (a) non electrical potential, (b) forward bias and (c) reverse bias	32
Figure 2.16 Photoexcitation in semiconductors	35
Figure 3.1 (a) Hysteresis loop measured at 15 kHz showing high remnant polarization $\sim 55 \mu\text{C}/\text{cm}^2$, and (b) magnetic hysteresis loop for 70 nm BFO film with an appreciable saturation magnetization of $150 \text{ emu}/\text{cm}^3$, and a coercive field of 200 Oe. NOTE: The in-plane loop is shown in blue, and the out-of-plane loop is in red	38
Figure 3.2 Perovskite crystal structure of bulk BiFeO_3	39

Figure 3.3 Schematic representation of bismuth ferrite spin cycloid. The canted antiferromagnetic spins (blue and green) give rise to a net magnetic moment (purple arrows) that is spatially averaged out to zero due to the cycloidal rotation	41
Figure 3.4 (a) 71° domain boundary with continuous oxygen octahedral rotations, (b) 109° domain boundary with continuous oxygen octahedral rotation centered on the FeO_2 plane, and (c) 180° domain boundary with continuous oxygen octahedral rotations	43
Figure 3.5 (a) Topography of BFO thin films with roughness (rms) of 0.5 nm, (b) In-plane PFM image of a written domain pattern in a mono-domain BFO (110) film showing all three types of domain wall, that is, 71° (blue), 109° (red) and 180° (green), and (c) corresponding c-AFM image showing conduction at both 109° and 180° domain walls; note the absence of conduction at the 71° domain walls	43
Figure 3.6 (a) Hysteresis loop at 300 K for bismuth ferrite nanoparticles, and (b) Size, d represents the diameter of the as-prepared nanoparticles. M_s is the magnetization observed at $H = 50 \text{ kOe}$. H_c and H_x represent derived coercivities and exchange bias parameters, respectively	47
Figure 3.7 Raman Spectra of bismuth ferrite nanoparticles with size of: (a) 14 nm, (b) 41 nm, (c) 51nm, (d) 75 nm, (e) 95 nm, (f) 245 nm, and (g) 342 nm, respectively as well as of the bulk (h). The Si peaks are identified with an asterisk. The arrow is referring to the A_1 mode at 136 cm^{-1}	47
Figure 3.8 (a) Absorption coefficient at 300 K for bulk and 16 nm bismuth ferrite, and (b) close up view of $A_1(\text{TO1})$ phonon mode at 300 K	48

Figure 3.9 Absorption coefficient of 16 nm bismuth ferrite nanoparticle as compared with epitaxially grown rhombohedral thin film. Inset: Direct band gap analysis of the thin film and nanoparticles	49
Figure 3.10 (a) Scanning electron microscope image of crystallize bismuth ferrite nanofibers, and (b) magnetic hysteresis loop	50
Figure 3.11 (a) Diameter dependence of the room temperature raman spectra of the co-doped bismuth ferrite nanowires, and (b) diameter dependent variation of the magnetic hysteresis loops of the co-doped nanowires measured at 300K	51
Figure 3.12 Polarization hysteresis loops compositions of $x = 0.1, 0.14$ and 0.16 (a) 5 kHz, and (b) 25 kHz	53
Figure 3.13 (a) Dielectric constant ϵ_{33} and $\tan \delta$ measured at 1 MHz (zero bias), and (b) High field d_{33} determined from piezoelectric hysteresis loop measured as a function of composition (not shown here)	54
Figure 3.14 (a) Hysteresis loop of BLFO-PZT thin films measured at 5 kHz, and (b) Dielectric properties measured at 1 kHz	55
Figure 3.15 (a) Hysteresis loops for (a) single layer BNT thin film, (b) single layer BFO thin film, and (c) bi-layered BFO/BNT thin film	57
Figure 3.16 (a) Frequency dependent of dielectric behavior, and (b) dc conductivity vs $1/T$ at different frequencies for the bi-layered BFO/BNTBT thin film	58
Figure 3.17 (a) [003] peaks from x-ray scans showing the effect of film thickness on epitaxial strain. As the film thickness increased, the peak position progressively increases (black line, 70 nm; red line, 100 nm; blue line, 200 nm; and green line, 400 nm), and (b) small signal d_{33} for a 50 μm capacitor	59

Figure 3.18 Pressure-temperature phase diagram for BFO thin films with a thickness of 70 nm	60
Figure 3.19 Scanning electron microscope image (a) surface of the films with low roughness regions and of ~100 nm high square outgrowths, (b) red-green-blue image constructed by superimposing colored element-selective mapping (red: Bi; green: Fe; blue: O). NOTE: white scale bar corresponds to 1 μm	60
Figure 3.20 (a) XRD patterns of BFO epitaxial films grown under different oxygen pressures, (b) Ferroelectric polarization, (c) leakage current density, and (d) piezoelectric coefficient d_{33} as a function of electric field measured at 50 kHz	61
Figure 4.1 Schematic description of Bragg's equation	68
Figure 4.2 Schematic of an X-ray diffraction setup	69
Figure 4.3 X-ray diffraction angles for a thin film deposited on a substrate	69
Figure 4.4 Schematic of basic principle of RBS	71
Figure 4.5 Schematic diagram of a typical backscattering spectrometry setup	72
Figure 4.6 Description of the vibrational Raman Effect based upon an energy level approach	74
Figure 4.7 (a) Schematic of macro Raman Spectrometer, and (b) schematic of micro Raman Spectrometer	75
Figure 4.8 Schematic of the scanning electron microscope and transmission electron microscope	78
Figure 4.9 Signals and types of scattering	79
Figure 4.10 An EELS spectrum showing the zero loss peaks and low energy loss region at reduced gain and an excitation absorption edge	80

Figure 4.11 The sample is placed under the light source. (a) Light On, (b) Light Off, and (c) Current vs Time plot upon sample illumination	82
Figure 5.1 Flowchart of sol-gel deposition procedure	87
Figure 5.2 X-ray diffraction patterns for BFO-Mn doped thin films	89
Figure 5.3 Raman Spectroscopy for $\text{BiFe}_{1-x}\text{Mn}_x\text{O}_3$ thin films as function of Mn content	90
Figure 5.4 FESEM micrographs of $\text{BiFe}_{1-x}\text{Mn}_x\text{O}_3$ thin film surface (left side) and cross section (right side). (a-b) $x = 0.00$, (c-d) $x = 0.05$, (e-f) $x = 0.10$, and (g-h) $x = 0.15$	92
Figure 5.5 (a) Polarization hysteresis loop for BFO thin film, (b) Polarization hysteresis loop for $\text{BiFe}_{0.95}\text{Mn}_{0.05}\text{O}_3$ thin film, and (c) leakage current as a function of electric field for BFO and BFMO thin film Note: 20 layers is equivalent to an overall thickness of 200 nm	95
Figure 6.1 Schematic of three different thin film design deposited by PLD	99
Figure 6.2 Flowchart for the preparation of bismuth ferrite ceramic target by solid oxide method	101
Figure 6.3 Schematic diagram of the deposition system used for laser ablation	103
Figure 6.4 FESEM surface image of (a) BFO (inset: BFO cross section), and (b) BFO-La doped thin film	109
Figure 6.5 X-ray diffraction pattern for pure BFO thin film	109
Figure 6.6 Polarization-Electric Field (P-E) hysteresis loop for single layer bismuth ferrite thin film measured at 1 kHz and room temperature	110

Figure 6.7 X-ray diffraction pattern for BFOBKT thin films deposited at (a-b) 300 mTorr, (b-c) 400 mTorr, and (c-d) 500 mTorr. The left side images (a, c, d) are for 200, and right side images (b, d, e) are for 400 integration	112
Figure 6.8 Field emission SEM micrographs of surface and cross section for BFO-BKT thin films deposited under different oxygen pressure. (a-b) 300 mTorr, (c-d) 400 mTorr, and (e-f) 500 mTorr	115
Figure 6.9 RBS spectrum for BFO-BKT thin film deposited at different oxygen pressure	116
Figure 6.10 (a) Polarization-Electric field (P-E) loops and (b) leakage current characteristics for BFOBKT thin films deposited in a range of oxygen partial pressure of 300 – 500 mTorr	120
Figure 6.11 Dielectric properties of BFO-BKT thin films deposited in a range of oxygen partial pressure of 300 – 500 mTorr (a) relative dielectric constant, and (b) dielectric loss	121
Figure 6.12 X-ray diffraction pattern for BFO/BNT-BKT-BT bi-layered thin film near the (a) 002 integration, and (b) 400 integration	122
Figure 6.13 FESEM surface image of BFO/BNT-BKT-BT bi-layered. NOTE: Top layer is BFO	123
Figure 6.14 (a) P-E loop for BFO/BNT-BKT-BT bi-layered thin film, and (b) leakage current characteristics for BFO, BNT-BKT-BT, and BFO/BNT-BKT-BT thin films	125
Figure 6.15 Dielectric properties of BFO/BNT-BKT-BT bi-layered thin film (a) relative dielectric constant, and (b) dielectric loss	126

Figure 7.1 Schematic for electrospinning setup	131
Figure 7.2 Nanofibers deposited at separated distance between the needle and collector of (a) 15, (b) 20, (c) 25, and (d) 30 cm	139
Figure 7.3 X-ray diffraction pattern for a BFO thin film of the same precursor solution as the nanofibers	140
Figure 7.4 Raman Spectroscopy for 0.6M BFO nanofibers mat	141
Figure 7.5 Transmission electron microscope (TEM) image for a 100 nm nanofibers. (a) surface image, and (b) diffraction pattern	142
Figure 7.6 SEM surface micrographs for electrospun nanofibers of different precursor solution concentrations. (a) 0.4M, (b) 0.6M, (c) 0.8M, (d) 1.0M, (e) 1.2M, and (f) 1.4M	145
Figure 7.7 Nanofibers diameter as a function of precursor solution concentration	146
Figure 7.8 High resolution transmission electron microscope (HRTEM) image of a joint BFO nanofibers	146
Figure 7.9 Average grain size as a function of fiber diameter obtained from TEM	147
Figure 7.10 Fe valence state as a function of fiber diameter obtained from EELS analysis	149
Figure 7.11 Rutherford backscattering spectrometry results for 1.0 M (80 to 100 nm in diameter) BFO multiple-nanofibers	150
Figure 7.12 Rutherford backscattering spectrometry results for 0.8 M (50 to 70 nm in diameter) BFO multiple-nanofibers	150
Figure 7.13 Rutherford backscattering spectrometry results for 0.6 M (30 to 50 nm in diameter) BFO multiple-nanofibers	151

Figure 7.14 SEM surface images for BFO single nanofiber (a) top view of metal electrode, (b-d) zoom in image of the nanofiber between each metal electrode	152
Figure 7.15 Current vs Voltage for single nanofibers of different diameters at RT	153
Figure 7.16 Current vs time at constant voltage (10V) upon illumination	154
Figure 7.17 On/Off ratio for a multiple-nanofibers mat as a function of average diameter	155
Figure 7.18 Plot of the On/Off ratio in comparison with BFO grain size and Fe state for single nanofibers	156
Figure 7.19 Band diagram for different nanofibers diameter. (a-b) completely depleted, and (c) thin channel exists	158
Figure 7.20 (a) Schematic of device fabrication for BFO nanofiber field effect transistor. In the case of a single nanofiber device there is only one fiber between drain and source contacts. For a multiple-nanofibers device there are about ten nanofibers between drain and source contacts	159
Figure 7.21 Field effect transistor device transfer characteristic for (a) single-nanofiber device, and (b) multiple-nanofiber device	161
Figure 7.22 Field effect transistor device output characteristic for (a) single-nanofiber device, and (b) multiple-nanofiber device	162

List of Tables

Table 1.1 Piezoelectric properties of hard and soft PZT	2
Table 2.1 Thirty-two point groups in crystallography	14
Table 2.2 Mechanisms for Multiferroic	26
Table 2.3 Summary of different field effect transistors types and operation requirements	34
Table 4.1 Comparison between TEM and SEM	78
Table 5.1 Comparison of the Raman mode peak positions from the present study and the literature	91
Table 6.1 Weight of raw materials for a 100 g batch of BiFeO_3	102
Table 6.2 Weight of raw materials for a 100 g batch of $0.6\text{BiFeO}_3\text{-}0.4(\text{Bi}_{0.5}\text{K}_{0.5})\text{TiO}_3$	102
Table 6.3 Weight of raw materials for a 100 g batch of $0.88(\text{Bi}_{0.5}\text{Na}_{0.5})\text{TiO}_3$ $0.08(\text{Bi}_{0.5}\text{K}_{0.5})\text{TiO}_3\text{-}0.04\text{BaTiO}_3$	102
Table 6.4 Peak integration parameters for (200) peak profiles	113
Table 6.5 Bi/Fe ratio according to RBS simulation	114
Table 6.6 Ferroelectric values for BFO based thin film solid solution	118
Table 7.1 Electrospinning processing optimization: Flow rate	137
Table 7.2 Electrospinning processing optimization: Voltage	137
Table 7.3 Electrospinning processing optimization: Spinning distance (between the needle and the collector)	138
Table 7.4 d-spacing for single BFO nanofibers from TEM	143

Table 7.5 Chemical composition for BFO multiple-nanofibers (mat)	151
-------------------------------------------------------------------------------	-----

1 Research Objectives and Scope of the Dissertation

1.1 Statement of the problem

Lead-based $\text{Pb}(\text{Zr}_{1-x}\text{Ti}_x)\text{O}_3$ (PZT) compositions near the morphotropic phase boundary ($x \sim 48\%$) have been the leading material for transducers applications because of its high electromechanical properties described in Table 1.1. In a basic sense when a piezoelectric material is subjected to a stress it generates an electric charge. The opposite of this phenomenon holds true when an electric field is applied to a piezoelectric material its shape deforms in proportion to the applied field. In comparison with early discovered piezoelectric material such as barium titanate (BaTiO_3), PZT exhibits stronger electromechanical properties and higher operating temperature. Regardless of its outstanding properties summarized in Table 1.1, PZT and related composition contains a high content of lead. The lead content raises environmental concerns because of its toxicity levels. The lower vapor pressure of lead oxide (PbO) and the required high temperature during the processing results in lead evaporation. The lead is release to the environment causing harmful effects to the ecosystem. The disposal and recycling processes of lead based materials is another concern for those used in consumer products. Therefore imperative measures have been taken to restrict the usage of lead based composition for commercial applications. Many government regulations have been enacted in respond to this inquiry such as the Restriction of Hazardous Substances (RoHS) directives in Europe and China, the European RoHS directive restrict hazardous substances (lead) used in electronic equipment ¹. Thus, there is a great interest in the

development of environmental friendly, biocompatible, and lead free piezoelectric materials.

Table 1.1 Piezoelectric properties of hard and soft PZT ceramics ²⁻⁴

Parameter	Hard PZT4 *	Soft PZT5H **
d_{33} (pC/N)	289	593
g_{33} (10^{-3} Vm/N)	26.1	19.7
k_t	0.51	0.50
k_p	0.58	0.65
Q_m	500	65
E_C (kV/cm)	18	15
T_C (°C)	328	193
ϵ_r @ 1 kHz	1300	3400
$\tan \delta$ @ 1kHz	0.004	0.02

*doped with acceptor ions such as K^+ or Na^+ at the A site or Fe^{3+} , Al^{3+} or Mn^{3+} at the B site ²

** doped with donor ions such as La^{3+} at the A site or Nb^{5+} or Sb^{5+} at the B site ²

In the past fifteen years there has been a significant increase in investigations and development of lead free materials. Currently the lead free perovskite can be grouped in two main families: $(K_{0.5}Na_{0.5})NbO_3$ (KNN) and $(Bi_{0.5}Na_{0.5})TiO_3$ (BNT). Despite the effort to obtain similar piezoelectric properties to PZT, none of these compositions are still ready to replace lead base compositions.

In recent years, bismuth ferrite (BiFeO_3 -BFO) has been considered a potential candidate for the development of lead free ferroelectrics due to its high Curie temperature, 1100 K and high Néel temperature, 650 K of antiferromagnetism ^{5,6}. Theoretically, spontaneous polarization (P_s) corresponds to [111] direction of rhombohedral structure and is expected to display value of $\approx 100 \mu\text{C.cm}^{-2}$. Practical applications of BFO are hindered because of the high leakage current at room temperature.

Bismuth ferrite is also a unique material showing multiferroic (ferroelectric and antiferromagnetism simultaneously) behavior at room temperature. Recently, BFO turn out to be a potential candidate for optical applications ^{7,8} because of the favorable low bandgap of 2.7 eV ^{9,10} that unlike other ferroelectric materials is in the visible range. Anomalous in photoexcited voltage which exceeds the several times the band gap limitations have been reported ¹¹. These effects make BFO attractive for photovoltaic applications. However, a major limitation in practical applications is the low power conversion efficiency ¹².

Even though the investigation on bulk bismuth ferrite exhibited poor ferroelectric properties researchers continue to study this system. Report on the development of bismuth ferrite epitaxial thin film (200 nm) by pulsed laser deposition with very high spontaneous polarization further sparked the materials science community ¹³. When the particle size is reduced lower than antiferromagnetic periodicity (64 nm) the spiral cycloid is suppressed and the magnetic properties become sizeable ¹⁴. Since then (2003 to 2007), the research has evolved into a new scale searching for novel BFO based compositions for future electronic applications.

1.2 Objectives

The purpose of this research was to develop BFO nanostructures (thin film and nanofibers) and study the ferroelectric, optical, and semiconductor properties as potential candidate for multifunctional applications. Along with the processing of bismuth ferrite nanofibers, field effect transistors devices of such nanofibers were fabricated and their electrical performance was evaluated.

On the thin film fabrication, the study was focused in the combination of bismuth ferrite with other lead free compounds in the form of binary system and bi-layered structure to couple, enhance the ferroelectric performance, and minimize the leakage current. Accordingly the microstructure, phase, orientation, ferroelectric properties, and leakage current were characterized.

- 1- Study the effect of controlled atmosphere on the ferroelectric properties of **BFO-BKT** thin films.
- 2- Study the ferroelectric properties of **BFO/BNT-BKT-BT bi-layered** thin film architecture.
- 3- Minimize the leakage current on **Mn doped** bismuth ferrite thin films.

Another objective of this research was on the development of BFO nanofibers as outlined below:

- 1- Optimization of electrospinning sol-gel solution to **fabricate nanofibers**.
- 2- Investigate the microstructure, chemical composition, and crystalline phase of deposited nanofibers.
- 4- Study the **optical properties** for opto-electronic applications.
- 5- Investigate the effect of **nanofiber diameter** on the grain size, iron valence fluctuation, and electrical properties.
- 6- Fabrication of **field effect transistor device** based on bismuth ferrite single and multiple nanofibers.

1.3 Thesis organization

In Chapter 2, fundamentals of ferroelectricity, piezoelectricity, multiferroicity and semiconductor properties are briefly discussed. Chapter 3 is a literature review of bismuth ferrite thin films by chemical solution and pulsed laser deposition methods, also it reviews the fabrication and characterization of nanostructures such as cubes, wires, tubes, and crystal to enhance antiferromagnetic performance and novel applications. Chapter 4 briefly described the characterization tools and equipments required to study and understand bismuth ferrite thin film and nanofibers system such as RBS, XRD, TEM, EELS, and SEM.

The experimental results and discussion is divided in two major topics: bismuth ferrite thin films by Sol-gel and Pulsed Laser Deposition (Chapter 5 & 6) and bismuth ferrite nanofibers (Chapter 7). Chapter 5 and 6 provides processing details of bismuth ferrite thin films by two different routes and their ferroelectric behavior. Chapter 7 presents a detailed study in the deposition of bismuth ferrite nanofibers by electrospinning, the effect of size reduction on its chemical and electrical behavior. The fabrication of FET devices based on BFO nanofibers is also described and analyzed. Chapter 8 is the summary and conclusions of the research carry out in the multifunctional properties and applications of bismuth ferrite thin films and nanofibers. Chapter 9 presents a summary of suggested future activities for BFO system in both forms.

1.4 References

1. US Department of Commerce, N. Support of Industry Compliance with the EU Directive on Restriction of Certain Hazardous Substances (RoHS). at <http://www.nist.gov/mml/csd/inorganic/rohs.cfm>
2. Korotcenkov, G. *Handbook of Gas Sensor Materials: Properties, Advantages and Shortcomings for Applications Volume 1: Conventional Approaches*. (Springer Science & Business Media, 2013).
3. Chung, D. D. L. *Functional Materials: Electrical, Dielectric, Electromagnetic, Optical and Magnetic Applications : (with Companion Solution Manual)*. (World Scientific, 2010).
4. Thomas R. Shrout, S. J. Z. Lead-free piezoelectric ceramics: Alternatives for PZT? **19**, 113–126
5. Venevtsev, Y. N., Zhdanov, G. S. & Solov'ev, S. P. *Sov Phys Crystallogr* **4**, 538 (1960).
6. Fischer, P., Polomska, M., Sosnowska, I. & Szymanski, M. Temperature dependence of the crystal and magnetic structures of BiFeO₃. *J. Phys. C Solid State Phys.* **13**, 1931–1940 (1980).
7. Alexe, M. & Hesse, D. Tip-enhanced photovoltaic effects in bismuth ferrite. *Nat. Commun.* **2**, 256 (2011).
8. Choi, T., Lee, S., Choi, Y. J., Kiryukhin, V. & Cheong, S.-W. Switchable ferroelectric diode and photovoltaic effect in BiFeO₃. *Science* **324**, 63–66 (2009).
9. J. F. Ihlefeld, N. J. P. Optical band gap of BiFeO₃ grown by molecular-beam epitaxy. *Appl. Phys. Lett. - APPL PHYS LETT* **92**, 2908–142908 (2008).
10. Young, S. M., Zheng, F. & Rappe, A. M. First-Principles Calculation of the Bulk Photovoltaic Effect in Bismuth Ferrite. *Phys. Rev. Lett.* **109**, 236601 (2012).
11. Yang, S. Y. *et al.* Above-bandgap voltages from ferroelectric photovoltaic devices. *Nat. Nanotechnol.* **5**, 143–147 (2010).
12. Yang, S. Y. *et al.* Photovoltaic effects in BiFeO₃. *Appl. Phys. Lett.* **95**, 062909 (2009).
13. Wang, J. *et al.* Epitaxial BiFeO₃ Multiferroic Thin Film Heterostructures. *Science* **299**, 1719–1722 (2003).
14. Park, T.-J., Papaefthymiou, G. C., Viescas, A. J., Moodenbaugh, A. R. & Wong, S. S. Size-Dependent Magnetic Properties of Single-Crystalline Multiferroic BiFeO₃ Nanoparticles. *Nano Lett.* **7**, 766–772 (2007).

2 Introduction and Background

2.1 Introduction

The prime objective of this chapter is to briefly introduce, describe, and explore materials properties and characteristics implicated in this investigation. Materials have been grouped into three basic categories: metals, ceramics, and polymers. This classification is based on the atomic structure or chemical composition. Most materials falls into one of these categories, although there are some intermediates ¹. Additionally, there are various combinations of this group known as advance materials; advance materials are used in high technology applications and include semiconductors, biomaterials, smart materials, and nano-engineered materials. Presently, this research focused on the electronic properties of smart materials such as: ferroelectric thin films and semiconductor nanofibers. A brief explanation of these materials representative characteristics and their applications is offered in the following sections.

2.2 Dielectric materials

A dielectric material is one that is electrically insulating and exhibits an electric dipole – the separation of positive or negative charge on an atomic or molecule level under electric field. If a dielectric material is sandwiched within two plates (Figure 2.1) then the capacitance C in terms of the stored charge is defined as:

$$C = \epsilon \frac{A}{d} \quad (2.1)$$

where ϵ is the permittivity of the dielectric material, and ϵ_0 (8.85×10^{-12} F/m) is the permittivity of the free space. The relative permittivity or often referred as the *dielectric constant* is the ratio of:

$$\epsilon_r = \frac{\epsilon}{\epsilon_0} \quad (2.2)$$

which represents the increase in charge storing capacity of the dielectric material. As mentioned above for every dipole moment there is a charge separation between positive and negative electric charge. When an electric field, E , is applied a force will induce an electric dipole to be oriented in the direction of the applied field; this phenomenon is called polarization P . The SI units of polarization are C/m². The surface density (sometimes called electric displacement) D , or the amount of charge per unit area between the plates is proportional to the electric field and defines as ^{1,2}:

$$D = \epsilon_0 E \quad (2.3)$$

In the presence of a dielectric material, the surface density is represented as follows:

$$D = \epsilon_0 E + P \quad (2.4)$$

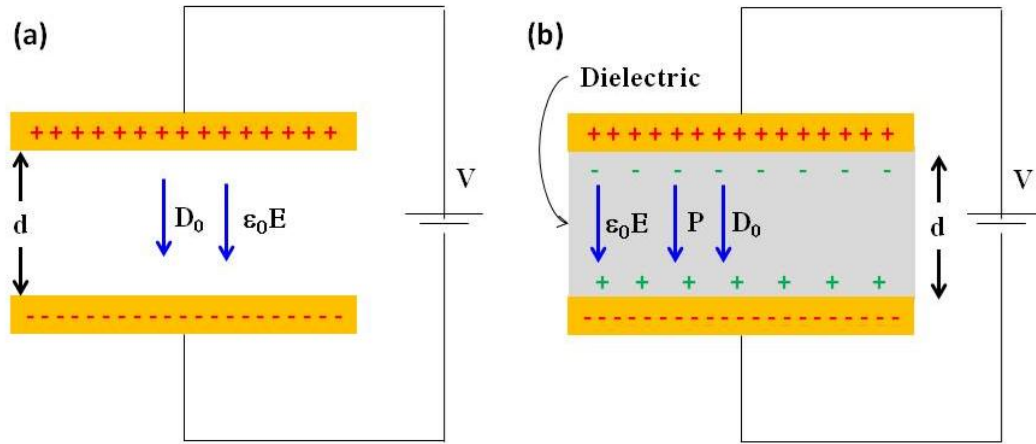


Figure 2.1 A parallel plate capacitor (a) when a vacuum is present and (b) when a dielectric material is inserted.

There are four types of polarization that contribute to the dielectric properties: electronic, ionic, molecular, and space charge as schematically shown in Figure 2.2. Dielectric materials commonly show at least one of these types of polarization. The *electronic contribution* as a result of an external electric field causes a displacement of the center of the electron cloud relative to the nucleus, and thus induces a dipole moment. In *ionic polarization* the material must possess an ionic character. It then has internal dipole, but these built in dipoles cancel each other and net dipole moment is zero. An applied external field acts to displace the ions which induce a net dipole moment. The third type, *molecular or orientation polarization* is found only in a substance that possesses permanent dipole moments which can rotate freely. In thermal equilibrium the dipoles are randomly oriented and do not exhibit a net dipole moment contributing to the polarization. Upon an applied electric field the permanent dipole moments rotate and align to certain extent inducing polarization. The *space charge* type are mobile charge carriers that can migrate an appreciable distance through the dielectric but become trapped or cannot discharge at an electrode. Each mechanism is active within a certain

frequency range. The dependence of real part of the permittivity on the field of frequency is represented in Figure 2.3 for a dielectric material that exhibits all four types of polarization (frequency in logarithmic scale). Electrons have very small mass so are able to follow high frequency up to optical range. Ions are much heavier (thousands time) and are still able to follow the fields up to infrared range. Molecules are heavier yet (in mass) and are severely impeded by their surroundings. Most of them are limited to microwave frequencies. The space charge effects are often in the kHz range or lower. For each polarization type a minimum re-orientation time exists, which depends on the ability with which the different dipoles are capable of realignment.

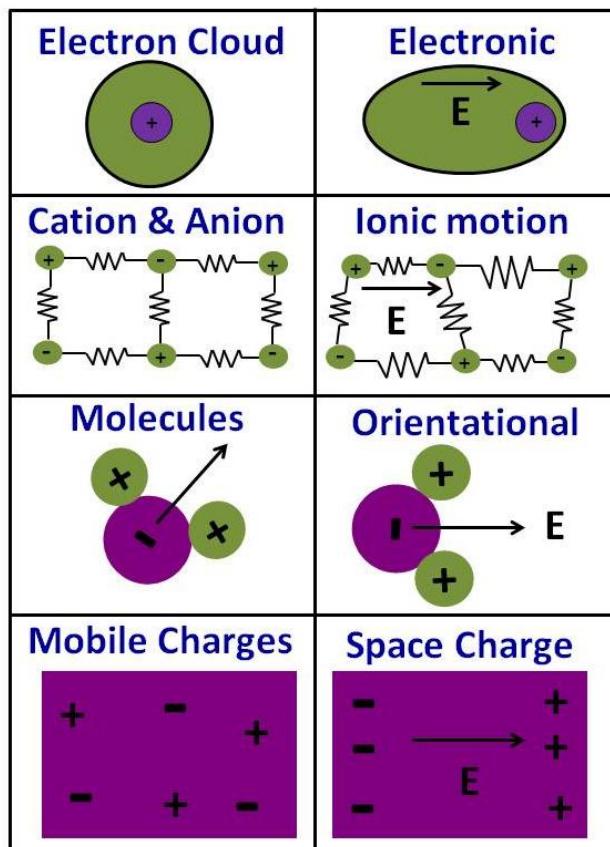


Figure 2.2 Polarization mechanisms leading to dielectric polarization/displacement ³.

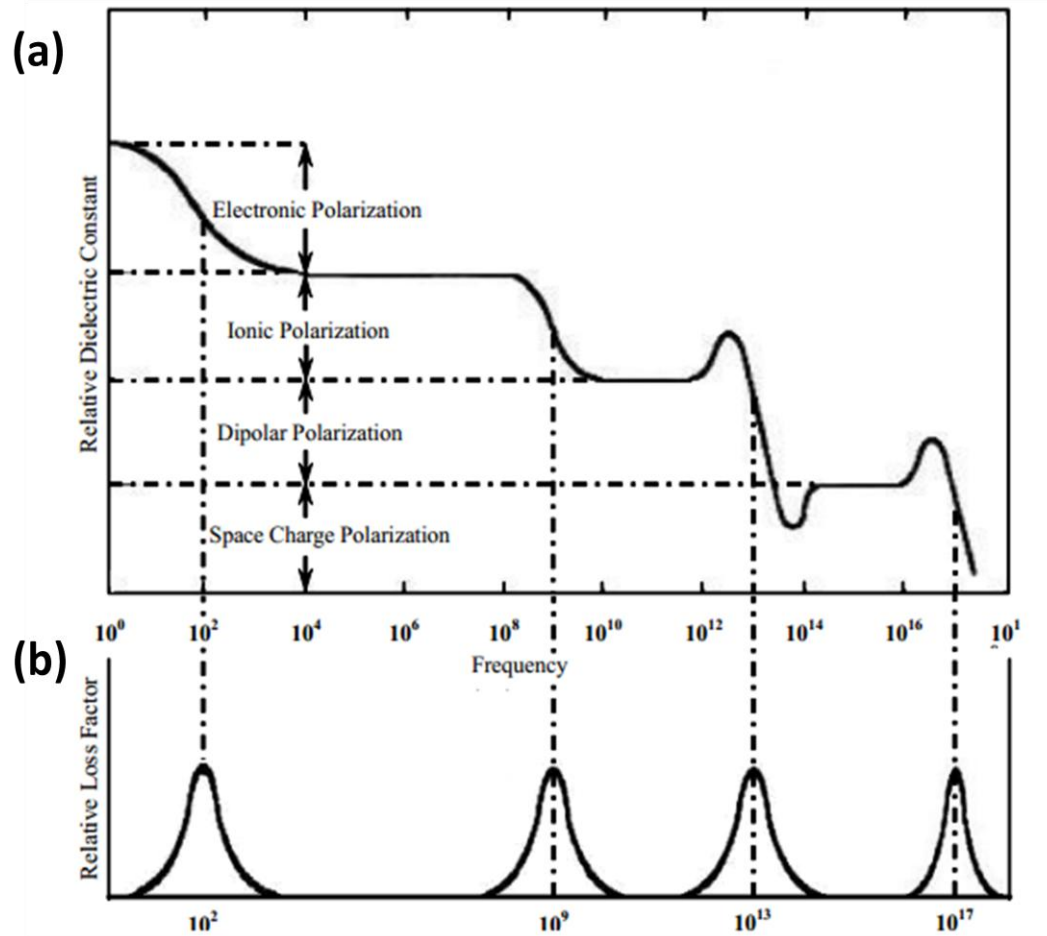


Figure 2.3 Variation of dielectric constant with frequency of alternating electric field. Electronic, ionic, orientation and space charge contributions to the dielectric constant are indicated ^{1,4}.

Dielectrics materials are classified in two major categories: *non ferroelectric* (paraelectric or normal dielectric) and *ferroelectric*. The non ferroelectric category may be divided into three classes: Non polar materials, polar materials and dipolar materials. In this category, the polarization is caused by an electric field. For the first class of non ferroelectric the electric field can only produce elastic displacement of the electron clouds so they only have electronic polarization. Such materials are referred as elemental materials which consist of a single atom. For this category the absorption occurs at the resonance frequency which is in the visible-ultraviolet region. In the second class, an

electric field will cause elastic displacement of the electron cloud and elastic displacement of the positions of ions. Such materials exhibit both electronic and ionic polarization. The absorption occurs at two different resonant frequencies: (1) optical frequency region and (2) infrared region which corresponds to the electronic and ionic polarization respectively. The third class has three types of polarization electronic, ionic and orientational ⁵. The second category of ferroelectric dielectrics is going to be discussed in the next session.

2.3 Piezoelectricity

Structural symmetry of crystal depends on its lattice structure which is described by Bravais unit cell of the crystal. There are only thirty two macroscopic symmetry types and can be classified as follows: *centrosymmetry* and *non-centrosymmetry*. The first type with center symmetry includes eleven point groups. The other twenty one point groups among the thirty two groups do not have centrosymmetry. All non centrosymmetry point groups except the point group 432 exhibit piezoelectric effect. The piezoelectric effect was discovered by Jacques Curie and Pierre Currie in 1880. *Piezoelectricity* is the electric charge accumulated in response to an applied mechanical stress. Such phenomenon is known as the *direct effect*. When an electric field is applied and the polarization cause a change in the shape or dimensions it's called the *converse effect* ⁶. The equations that described the piezoelectric effect in regard of the elastic and electric properties are in a general form:

$$D_i = \varepsilon_{ijk} T_{jk} \quad (2.5)$$

$$\varepsilon_{ij} = s_{kij} E_k \quad (2.6)$$

where D is the electric charge density (electric displacement), ϵ is the permittivity and E is the electric field strength. In equation 2.6 S is the strain, s is the compliance and T is the stress.

Table 2.1 Thirty-two point groups in crystallography ⁷

Crystal System	International Notation	Remarks
Triclinic	1	+ ♦
	$\bar{1}$	-
Monoclinic	2	+ ♦
	$m(\bar{2})$	+ ♦
	2/m	-
Orthorhombic	2mm	+ ♦
	222	+
	mmm	-
Tetragonal	4	+ ♦
	$\bar{4}$	+
	$\bar{4}2m$	+
	422	+
	4mm	+ ♦
	4/m	-
	4/mmm	-
Trigonal	3	+ ♦
	$\bar{3}$	-
	3m	+ ♦
	32	+
	$\bar{3}m$	-
Hexagonal	6	+ ♦
	$\bar{6}m$	+
Hexagonal (cont)	6mm	+ ♦
	6/m	-
	622	+
	$\bar{6}m2$	+
	6/mmm	-
Cubic	23	+
	$\bar{4}3m$	+
	m3	-
	43	-
	m3m	-

‘+’ implies that piezoelectric may be exhibit and ‘♦’ implies that pyroelectric and ferroelectric effects may be exhibited

Piezoelectric materials are utilized in transducers which are devices that convert an electrical signal into a mechanical strain or vice versa. The symmetry of a crystal affects the properties of a material such as dielectric, elastic, piezoelectric, ferroelectric and nonlinear optical properties.

2.4 Ferroelectric materials

The group of dielectric called ferroelectric exhibit spontaneous polarization (P_s) in the absence of an electric field. The electric dipoles are not randomly placed but interact in such a way as to align themselves even without an external field. A distinguished feature of ferroelectrics is that the spontaneous polarization can be reversed by strong applied electric field in the opposite direction. Among the twenty point groups that exhibit piezoelectricity there are ten point groups that have one unique direction axes and thus possesses spontaneous polarization. A material that exhibit spontaneous polarization is composed of negative and positive ions. In certain temperature range the ions are in equilibrium and the center of the positive charge does not coincide with the center of the negative charge at this point the free energy of the crystal is minimum. There are different types of ferroelectric materials according to their crystallization such as perovskite, bronze-tungsten, and bismuth layer structure. The first one of the three is the best known material used for many applications. For example Figure 2.4 shows the crystal structure for perovskite ferroelectric barium titanate (BaTiO_3).

An important characteristic of ferroelectric is the transition temperature called *Curie temperature*, T_C . When the temperature decreases through T_C the ferroelectric crystal experience a transition from a paraelectric phase to a ferroelectric phase. When the

temperature is higher than T_C the crystal does not exhibit ferroelectricity. Above T_C ferroelectric behaves as non polar dielectric. The ferroelectric structure of a crystal is created by a distortion of the paraelectric phase such that the lattice symmetry in the ferroelectric phase is always lower than in the paraelectric phase. For the case of barium titanate the T_C is about 120°C at which paraelectric to ferroelectric transition occurs. However, barium titanate has other three different ferroelectric phases below the T_C shown in Figure 2.5. When the temperature is the vicinity of the T_C , the thermodynamic properties of a ferroelectric crystal exhibit some anomalies followed by a crystal structure change.

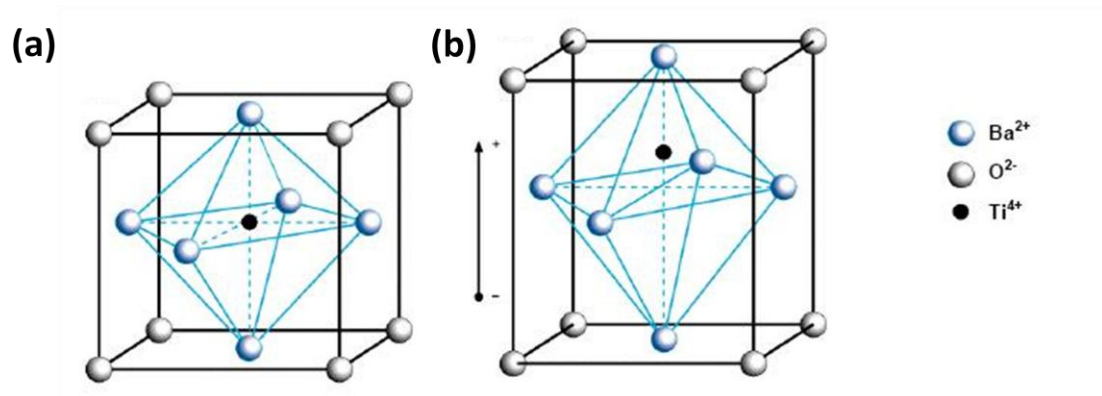


Figure 2.4 The crystal structure of barium titanate (perovskite structure). (a) Above Curie temperature the cell is cubic and (b) below the Curie temperature is tetragonal with Ba²⁺ and Ti⁴⁺ ions shifted relative to the O²⁻ ions.

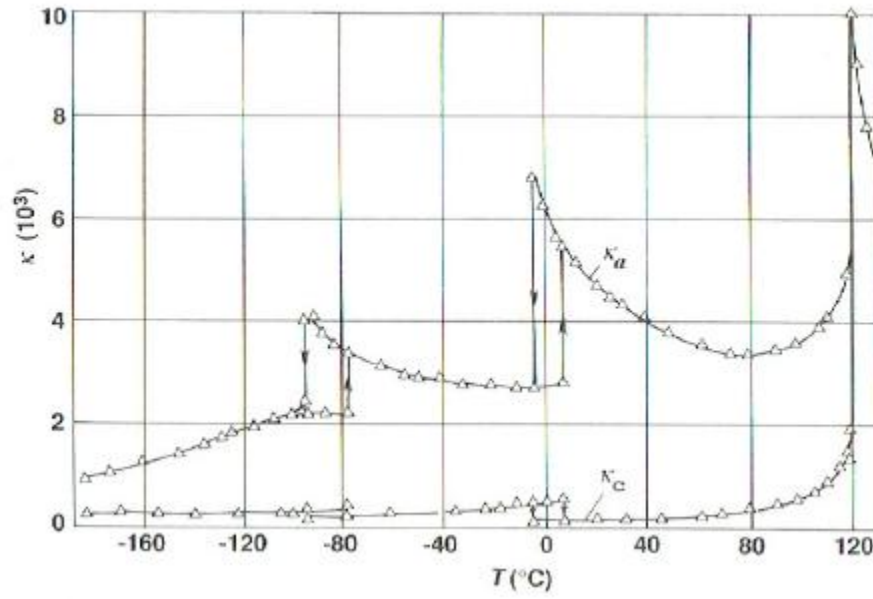


Figure 2.5 Temperature dependence of the dielectric constant in barium titanate ⁸.

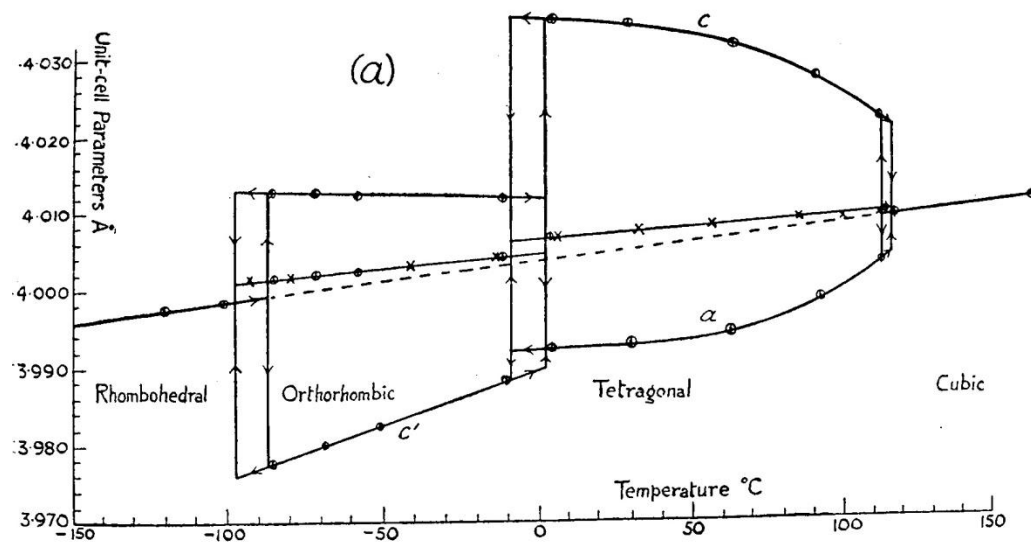


Figure 2.6 Barium titanate phase transition below T_C ⁴.

The temperature dependence of the dielectric constant above the T_C can be described by the *Curie-Weiss law*^{3,7}:

$$\varepsilon = \frac{\varepsilon_0 + C}{\theta - \theta_0} \quad (2.7)$$

where C is the Curie-Weiss constant and θ_0 the Curie-Weiss temperature. θ_0 is different from the Curie point. In the case of a first order transition, $\theta_0 < \theta_C$, while for second order transition $\theta_0 = \theta_C$. Usually the term ε_0 can be neglected because it is much smaller than $C/(\theta - \theta_0)$ when θ is near θ_0 .

Other characteristic of ferroelectrics is the *hysteresis loop*. The polarization is double-valued function of the applied electric field. At low applied electric field a linear relationship between the polarization and electric field is observed, because the electric field is not high enough to switch any domain and the material will behave as a normal dielectric. As the electric field increases a number of domains will be switch in one direction, and the polarization will increase rapidly until all the domains are aligned. This state is called saturation. When the electric field is decrease the polarization will also decrease but does not return to zero. Once the electric field reach zero some of the domains will remain aligned, and a remnant polarization is observed. In order to remove the remnant polarization an electric field in the opposite direction (negative) is applied. Further increase of the electric field on the opposite direction (negative) will cause an alignment of the domains in the opposite direction. The electric field required to reduce the polarization to zero is called the coercive field. The relation between polarization and electric field is represented by a hysteresis loop shown in Figure 2.7. The area within the loop is a measure of the energy to twice reverse the polarization². The spontaneous

polarization is equal to the saturation value of the electric displacement extrapolated to zero field. The remnant polarization is different than the spontaneous polarization if reverse nucleation occurs before the applied field reverses. This can happen in the presence of an internal/external stresses or if the free charges cannot reach the new equilibrium distribution during each half of the hysteresis loop. When doing this type of measurements special caution must be taken into account. Firstly, the loop gives only a measure of the switchable portion of the spontaneous polarization. Secondly, ferroelectric hysteresis loop can easily be confused with non-linear dielectric loss. Errors in the characterization of spontaneous polarization and even incorrect identification of ferroelectrics can be as a result of the non-linear contributions to the displacement ².

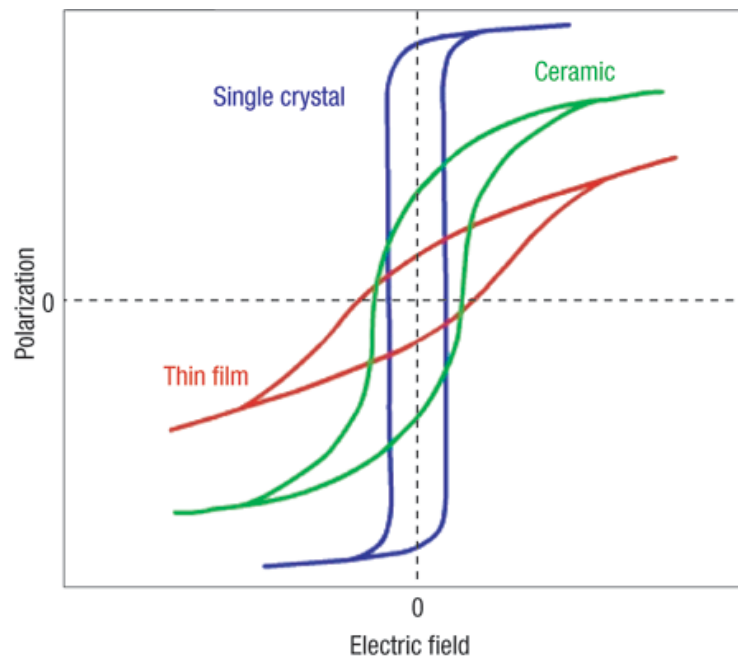


Figure 2.7 Typical hysteresis loop ⁷.

In a ferroelectric is likely that the electric dipoles aligned only in certain regions of different polarization. Each of these regions is called domains. A domain is a homogenous ferroelectric region in which all the dipoles moments in adjacent unit cell have the same orientation. There are several types of domains, and the two most common are: (1) 90° wall in which polarization vectors in adjacent domains at right angles and (2) 180° in which polarization vectors in adjacent domains are anti-parallel. Then the net polarization depends on the difference of the two domains orientations. If the volumes of the domains are equal then there is not a net polarization. The interface between those domains are called domain wall. The domain wall separates regions where the polarization changes. They have a width of 0.2 to 0.3 nm but this varies with crystal and temperature.

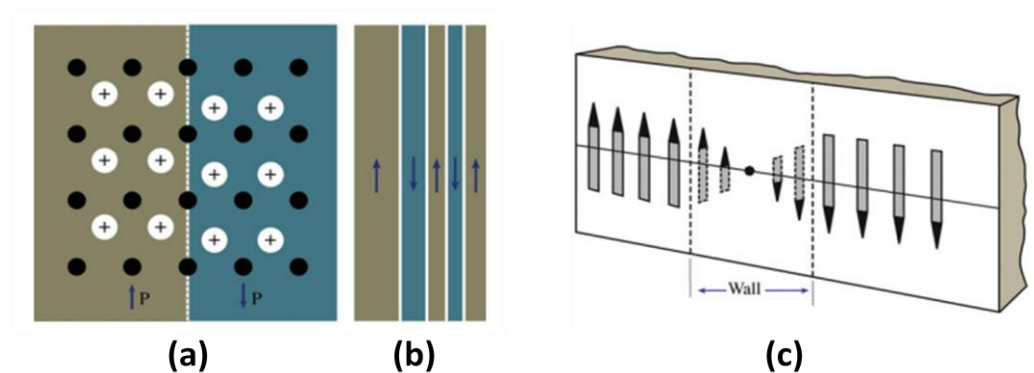


Figure 2.8 (a) ionic displacement in two 180° ferroelectric domains, (b) domain structure is showing several 180° domains of different sizes and (c) 180° domain wall with a width of $\sim 0.2 - 0.3 \text{ nm}$ ⁴.

2.5 Ferromagnetism

Analogous to ferroelectricity, ferromagnetism has a spontaneous magnetic moment in zero applied magnetic fields. The electron spins and magnetic moments are arranged in a regular manner. All of the spin arrangements sketched in Figure 2.9 except the simple antiferromagnet have a spontaneous magnetic moment, called saturation moment. The magnetization is defined as the magnetic moment per unit volume. Similar to ferroelectric materials, ferromagnetic possesses regions magnetized in different directions called domains. The magnetization refers to the value within a domain. The Curie temperature, T_C is the temperature above which spontaneous magnetization disappears.

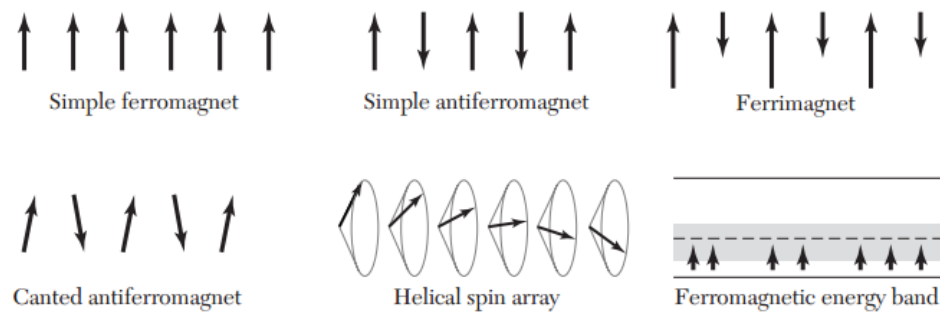


Figure 2.9 Order arrangements of electron spins ⁹.

A feature of ferromagnetic materials is the hysteresis loop which can be understood similar to a ferroelectric hysteresis loop through the concept of domains (magnetic). The motion of the domains and the re-orientation of the domains directions is not totally reversible evidence with a remnant magnetization. When the applied magnetic field is decrease (reverse) to the initial value, the domains do not return completely to their original position but retain some “memory” of their alignment. This memory leads to one

of the most important applications of ferromagnets for magnetic information storage such as magnetic tapes and disks ¹⁰.

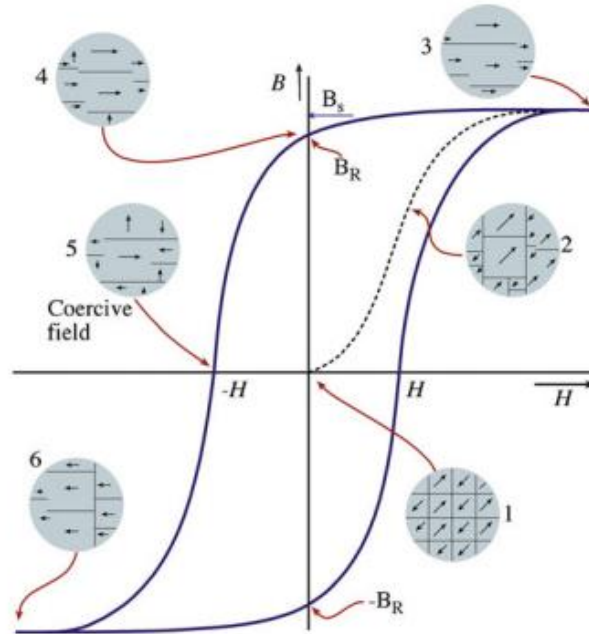


Figure 2.10 A magnetization hysteresis loop for a ferromagnetic material. Insets: domain structures at various magnetic fields ⁴.

According to Landau and Lifshitz the domain structure is a natural consequence of various contributions to the energy exchange, anisotropy and magnetic for a ferromagnetic body. To understand the origin of domains we may consider the structures in Figure 2.11a-e each one represent a cross section through a ferromagnetic crystal. Domains structures are usually more complicated than the examples shown below, but its origin is from the possibility of lowering the energy of a system.

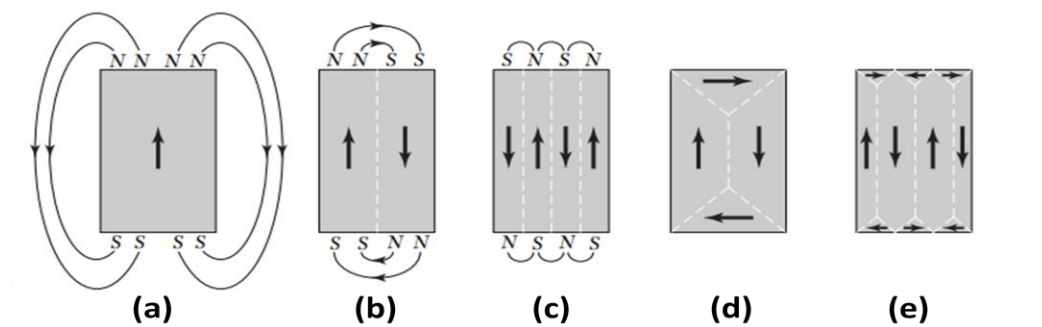


Figure 2.11 The origin of ferromagnetic domains. (a) single domain as a consequence of the magnetic “poles” formed on the surfaces, (b) the magnetic energy is reduced approximately one half by dividing the crystal into two domains magnetized in opposite directions, (c) with N domains the magnetic energy is reduced to approximately $1/N$ of the magnetic energy of a single domain, (d) and (e) in such domain arrangement the magnetic energy is zero ⁹.

Among the three magnetic phenomena in Figure 2.9 simple antiferromagnetism is the most common. In an antiferromagnet the spins are ordered in an anti-parallel arrangement with zero net moment at temperatures below ordering called Néel temperature, T_N . At and above the Néel temperature the susceptibility is independent of the direction of the field in relation with the spin axis. Below the T_N there are two scenarios: (1) when the applied magnetic field is perpendicular to the spin axis and (2) with the applied magnetic field parallel to the spin axis ⁹.

2.6 Multiferroic phenomenon and materials

Multiferroic combines any two or more of the primary ferroic orderings in the sample phase such as: ferroelectricity, ferroelasticity, and ferromagnetism (or any kind of magnetic order). However, current fashion applies the term multiferroic primarily to materials that exhibit simultaneous ferroelectric or ferromagnetic order. The most attractive aspect of multiferroic is the magnetoelectric coupling. In the magnetoelectric coupling a ferroic property is modified or controlled using its associated field (magnetic field modify magnetization and electric field modify polarization). In a multiferroic a magnetic field can tune the electric polarization and vice versa the electric field can tune the magnetization. In terms of the applications, the ability to use electric field to control the magnetism is particularly interesting because it could lead to smaller and more efficient device for magnetic technologies.

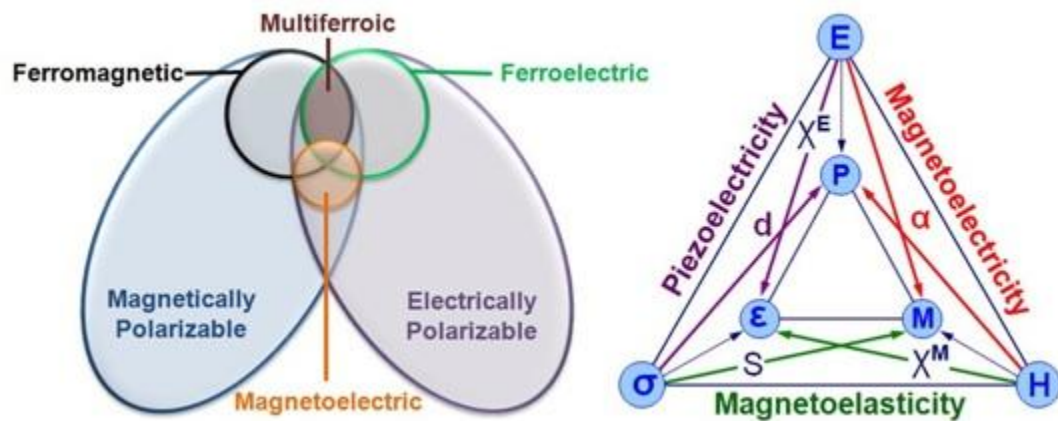


Figure 2.12 Multiferroics combined the properties of ferroelectrics and magnets ¹¹.

This phenomenon results in fascinating from a physics stand point because the mechanism to observe ferroelectricity and ferromagnetism is mutually exclusive. The conventional mechanism in ferroelectric requires formally empty d orbitals while the

formation of magnetic moment results from partially filled d orbitals. Also considering that polarization is represented by a polar vector and magnetization by an axial vector they have different symmetry properties; and is not clear that one should be addressed by the other associated field. Another restriction is that in order for a ferroelectric to keep a polarization, the material must be a robust insulator. However, most magnetic materials are conducting metals. In conventional ferroelectrics (single phase), the polarization arises when non magnetic cations shift away from the center of the surroundings anions. In other hand for magnetic materials, the magnetic cations tend to sit exactly at the center of the surroundings anions. In principle ferroelectricity and magnetism coupling could be achieved through an alternative non d electron mechanism for magnetism or an alternative mechanism for ferroelectricity. Presently in practice only the latter route has been pursued but there are also other possibilities summarized in the Table 2.2.

To better understand the basic phenomena and appreciate the main achievements and remaining problems it's necessary to classify multiferroics by the microscopic mechanism that determines their properties. Generally speaking there are two groups of multiferroics¹¹. The first group which is called type I multiferroics, contains those material where ferroelectricity and magnetism have different source and are independent of one another, but there is still some coupling between them. In this group ferroelectricity appears at higher temperature compared to magnetism and polarization is large in the order of $10 - 100 \mu\text{C}\cdot\text{cm}^{-2}$. Unfortunately the coupling in type I is usually weak. The challenge in this group is to maintain all their positive features but enhance the coupling. The second group which is called type II multiferroics magnetism causes ferroelectricity implying a high coupling between the two. However, in this case different

than type I the polarization is much smaller about $10^{-2} \mu\text{C}\cdot\text{cm}^{-2}$. There are also several subclasses of type I and type II multiferroics depending on the mechanism of ferroelectricity in them ¹¹. The Table 2.2 summarizes the different mechanism for multiferroics. The first three: Lone pair effects, geometric frustration and charge ordering belong to type I and the last one magnetic order to type II multiferroics.

Table 2.2 Mechanisms for Multiferroic ¹²

Mechanism	Description	Examples
Lone-pair effects	In perovskite of general formula ABX_3 , lone pairs of electron on the A cation distort the geometry of the BX_3 anion resulting in ferroelectricity	BiFeO_3 BiMnO_3
Geometric frustration	Long-range dipole-dipole interactions and rotations of oxygen atoms generate a stable ferroelectric state	YMnO_3
Charge ordering	Certain “non centrosymmetric” arrangements of ions induce ferroelectricity in magnetic materials	LuFe_2O_4
Magnetic ordering	Ferroelectricity is induced by magnetic lone-range order in which the arrangement of magnetic dipoles lacks reflection symmetry	TbMnO_3 , $\text{DyMnO}_3, \text{TbMn}_2\text{O}_4$

2.7 Semiconductor materials

Conductors are generally substances which have the property to pass different types of energy. The conductivity of metals is based on the free electrons due to the metal bonding. For an electron to become free it must be excited to one of the empty and available energy states above the Fermi Energy E_F . According to energy band structure for metals shown in Figure 2.13a there are vacant energy states adjacent to the highest filled state. This small energy is required to excite an electron into the low empty state. The insulators do not possess free charge carriers and thus are non conductive. Empty spaces adjacent to the top of the filled valence band are not available. In order for an electron to become free, it must be promoted across the energy band gap into empty spaces at the bottom of the conduction band. This is only possibly by providing to an electron the energy which is approximately equal to the E_g (difference in energy between the conduction and valence band).

A semiconductor is a type of material that has an electrical resistance which is between electrical resistance typical of metals and insulators. The main difference between a semiconductor and an insulator is that the semiconductor possesses a much smaller energy band gap E_g , between the top of the highest filled band (called the valence band), and the bottom of the vacant band just above it (called the conduction band) ¹³. The conductivity of a semiconductor is not as high as that of a metal nevertheless they have unique features that make them useful for special applications. Semiconductors can be classified in two groups: elemental semiconductor materials found in group IV of the periodic table and the compound semiconductor materials, most of which are formed from combinations of group III and group V elements ¹³.

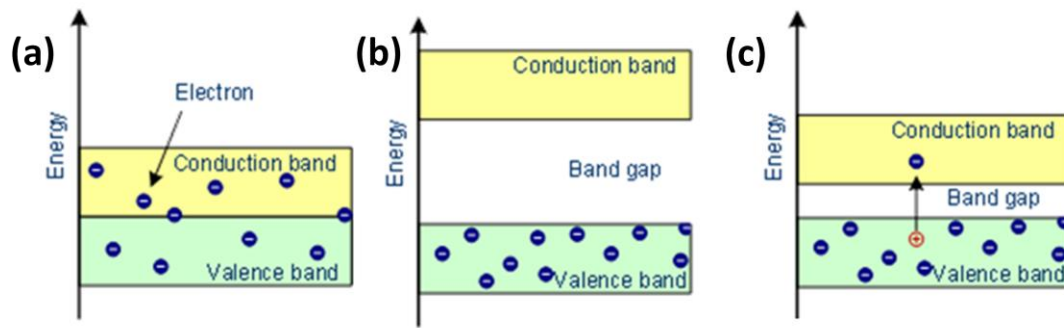


Figure 2.13 The energy band structure for (a) metal, (b) insulator and (c) semiconductor^{13,14}.

The electrical properties of semiconductors are sensitive to the presence of minimum amount of impurities leading to two types of electrical behavior. First, intrinsic semiconductors are those in which electrical behavior depend on the electronic structure inherent in the pure material. Second, extrinsic semiconductors are those in which the electrical behavior is influenced by the presence of impurity atoms.

The intrinsic semiconductor is characterized with an energy band structure shown in Figure 2.13c in which the valence band is filled and for every electron excited into the conduction band there is vacant electron state in the valence band called a *hole*. A hole is considered to have the same magnitude as an electron but with an opposite sign. Thus, in presence of an electric field both electrons and holes move in opposite directions. Practically all commercial semiconductors are extrinsic. When the density of electrons is greater than the density of holes, the semiconductor is considered as *n type*; donor impurity atoms have been added. When the density of holes is greater than the density of electrons, the semiconductor is *p type*; acceptor impurity atoms have been added¹⁵.

Considering an *n type* semiconductor a silicon (Si) atom has four electrons, each of which is covalently bonded with one of four adjacent Si atoms. If an impurity atom with

a valence of five is added as substitutional impurity only four of the five electrons of dopant can participate in the bonding because there only four possible bonds with neighbor atom. The extra non-bonding free electron is loosely bound near the region of the impurity atom by a weak electrostatic attraction. For each of the weakly bound impurities there is an energy state which is located within the forbidden band gap just below the conduction band. The electron binding energy is the energy required to excited one electron from this impurity energy state into the conduction band. Each excitation step donates a single electron to the conduction band – an impurity of these types is called *donor*. Since each donor is promoted from an impurity level there is no a corresponding hole left behind in the valence band. The electrons are majority carriers by their concentration and holes on the other hands are minority charge carries. An opposite effect is produced by adding a trivalent substitutional impurity such as aluminum, boron and gallium from the Group IIIA. One of the covalent bonds around each of the atoms is deficient of an electron such a deficiency may be view as a hole which is weakly bound to the impurity atom. In this case each impurity atom of this type introduces an energy level just above the valence band. An impurity of this nature is called an acceptor, because it is able to accept and electron from the valence band leaving a hole.

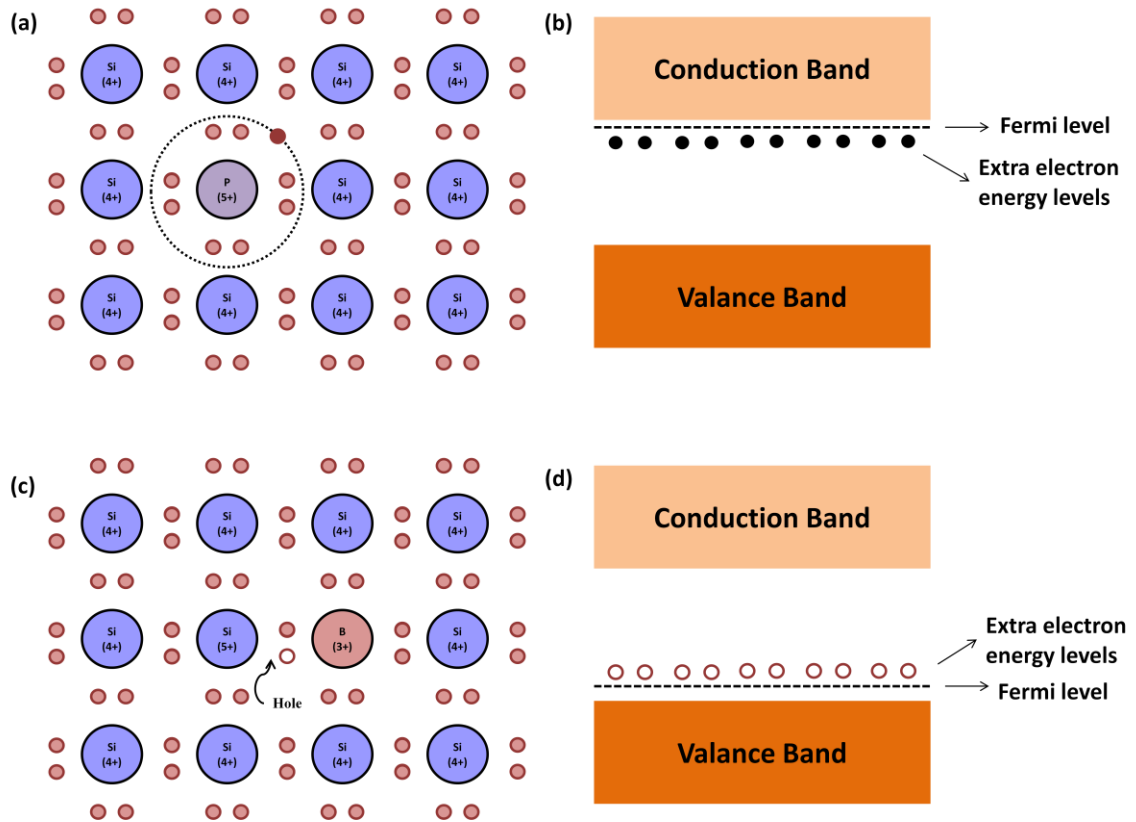


Figure 2.14 Extrinsic semiconductor (a) **n-type**: an impurity atom such as phosphorus with five valence electrons may substitute for a silicon atom resulting in an extra bonding electron, (b) **n-type** band diagram, (c) **p-type**: an impurity atom such as boron with three valence electrons may substitute for silicon atom resulting in a deficiency of a one valence electron, and (d) **p-type** band diagram: ¹.

The conductivity of a semiconductor material besides to being affect it by the concentration of impurities is also a function of the charge carrier mobilities. The career mobility is the ease with which electron and holes are transported through it. The magnitude of electron and holes mobilities is influenced by the same crystalline defects that are responsible for the scattering of electrons in metals: thermal vibrations and impurity atoms.

The unique electrical properties of semiconductor allow their use in devices to perform different functions. Diodes and transistors are two familiar examples. Some advantages of implementing semiconductor materials in electronic technologies are small size, lower power consumption, and no warm up time.

One of the first example diodes or rectifiers is a device that permits the flow of current in one direction but not in the other. A rectifier transforms an alternative current into a direct current. The rectifying junction is constructed from a single piece of semiconductor that is doped to be *n type* in one side and *p type* in the other side. Before applying any potential as discussed previously the *n type* side will be dominated by electrons carriers and the *p type* with holes. An external field could be applied across the p-n junction with two different polarities: forward bias or reverse bias. In a forward bias the positive terminal is connected to the *p-side* and negative to the *n-side*, the opposite polarity is referred as reverse bias ¹. The response of carriers to different polarities is shown in Figure 2.15. In the forward bias the electrons and holes are attracted to the junction area once they encounter continuously recombine. For these bias large number of carriers flow across the semiconductor junction as evidenced by an appreciable current and low resistivity. Oppositely, for reverse bias the carriers (electrons and holes) are pulling away from the junction leaving the junction region free of mobile careers and recombination will not occur. Thus, there is no flow of current and the junction become highly insulative.

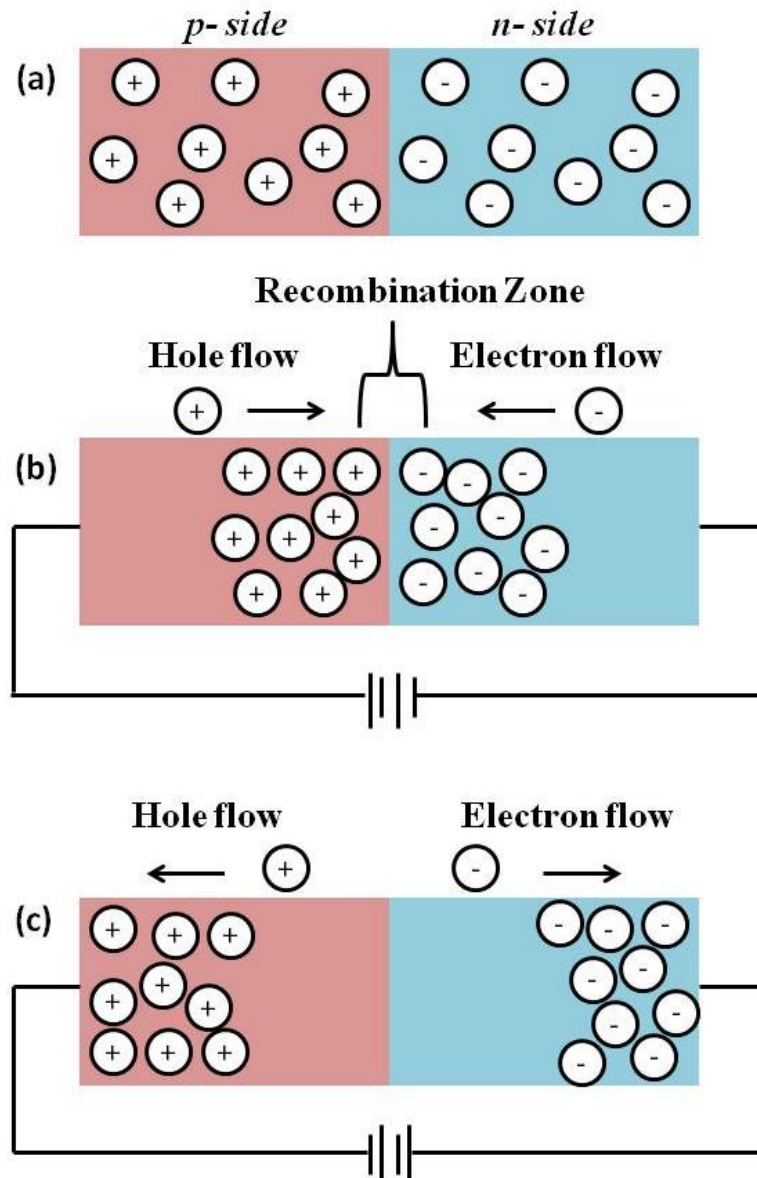


Figure 2.15 For a *p-n* rectifying junction representation of electron and hole distributions for (a) non electrical potential, (b) forward bias and (c) reverse bias¹.

Another example is the transistor which is an important semiconducting device in microelectronics circuitry. Transistor has two primary main functions: amplify an electrical signal and serve as switching devices for the processing and storage of information. A field effect transistor (FET) is a transistor that used an electric field (or the

lack of voltage) to control the shape and therefore the conductivity of a channel of one type of charge carrier in a semiconductor material ². Field effect transistors can be majority charge carriers devices in which the current is mostly due to majority carriers it can also be a minority charge carrier device in which the current is mainly because a flow of minority carriers. The device consists of a channel through which charge carriers (electrons or holes) flow from the source to the drain. The source and drain are part of the device architecture. They are conductors and are connected to the semiconductor material through ohmic contact. The conductivity of the channel depends on the potential applied across the gate and source terminals. The gate allows electrons to flow or block their passage by opening and closing the channel between the source and drain. In summary the FET's three terminals are ¹³.

1. Source (S) through which the carriers enter the channel
2. Drain (D) through which carriers leave the channel
3. Gate (G) terminal that modulates the channel conductivity and controls the current coming out of the drain terminal

There are four types of FET's: n-channel enhancement or depletion mode and p-channel enhancement or depletion mode. The n-channel and p-channel as explain previously is related to the density of electrons and holes in the semiconductor material. In the enhancement mode the transistor requires a voltage between gate and source (V_{GS}) to switch the device "ON" while the depletion mode requires a V_{GS} to switch the device "OFF". The enhancement mode is equivalent to a "Normally Open" switch while the depletion mode is equivalent to a "Normally Closed" switch.

Table 2.3 Summary of different field effect transistors types and operation requirements ^{16,17}

FET's type	$V_{GS} = \text{positive}$	$V_{GS} = 0$	$V_{GS} = \text{negative}$
n-channel depletion	ON	ON	OFF
n-channel enhancement	ON	OFF	OFF
p-channel depletion	OFF	ON	ON
p-channel enhancement	OFF	OFF	ON

If radiation falls onto a semiconductor its conductivity increases. The conductivity of a semiconductor is a function of the concentration of carriers. Radiation causes the covalent bonds to be broken and the electron-hole pair in excess of those generate thermally are created. These increase currents carriers decrease the resistivity of the semiconductor material and its called photoresistor or photoconductor. The energy band diagram for a photoexcited semiconductor having both acceptor and donor impurities is shown. When photons of enough energy illuminates the material the following transitions are possible: (1) an electron-hole pair can be created by a high energy photon referred as an *intrinsic excitation*, (2) a photon may excite a donor electron into the conduction band and (3) a valence electron may go to the acceptor state; the last two are referred as *impurity excitation* ^{15,16}.

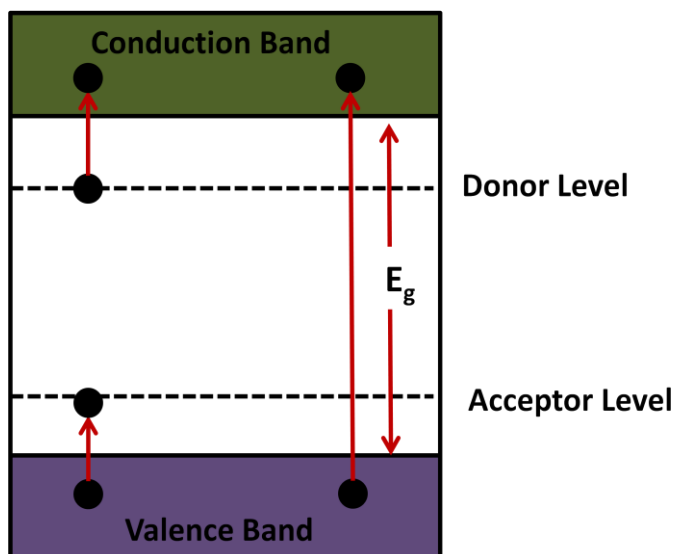


Figure 2.16 Photoexcitation in semiconductors ¹⁵.

2.8 Summary

In this chapter basic concepts studied in this investigation such as: dielectrics, piezoelectricity, ferroelectricity, and ferromagnetism phenomena's were briefly described. The multiferroic properties of materials are also introduced as an emerging field of study for advanced applications. Finally, semiconductor basic concepts were discussed. The semiconductor behavior of bismuth ferrite nanofibers is going to be studied further in this thesis. The discussion on multifunctional concepts is increasing and becoming more noticeable in the scientific community. Technologically, multifunctional materials play a crucial role in the next generation of "intelligent" devices. An understanding of multifunctional materials will open the gate for fascinating applications.

2.9 References

1. Callister, W. D. *Materials Science And Engineering: An Introduction*. (John Wiley & Sons, 2007).
2. Lines, M. E. & Glass, A. M. *Principles and applications of ferroelectrics and related materials*. (Clarendon Press, 1977).
3. Newnham, R. E. *Properties of Materials : Anisotropy, Symmetry, Structure: Anisotropy, Symmetry, Structure*. (Oxford University Press, 2004).
4. Carter, C. B. & Norton, M. G. *Ceramic Materials: Science and Engineering*. (Springer, 2007).
5. Kao, K.-C. *Dielectric Phenomena in Solids: With Emphasis on Physical Concepts of Electronic Processes*. (Academic Press, 2004).
6. Piezoelectricity. *Wikipedia, the free encyclopedia* (2014). at <<http://en.wikipedia.org/w/index.php?title=Piezoelectricity&oldid=612134483>>
7. Xu, Y. *Ferroelectric Materials and Their Applications*. (North-Holland, 1991).
8. Merz, W. J. The Electrical and Optical Behavior of Barium Priderite Single Domain Crystals. *Phys. Rev.* **76**, 1221–1225
9. Kittel, C. *Introduction to Solid State Physics*. (Wiley, 2005).
10. Halliday, D. *Fundamentals of Physics Extended, Eighth Edition Binder Ready Version*. (John Wiley & Sons Canada, Limited, 2007).
11. Khomskii, D. Classifying multiferroics: Mechanisms and effects. *Physics* **2**, 20 (2009).
12. Ramesh, R. Materials science: Emerging routes to multiferroics. *Nature* **461**, 1218–1219 (2009).
13. Neamen, D. A. *Semiconductor Physics And Devices: Basic Principles*. (McGraw-Hill, 2011).
14. Laube, P. Semiconductor Technology from A to Z. at <<http://www.halbleiter.org/en/fundamentals/conductors/>>
15. Millman, J., Halkias, C. & Jit, S. *Electronic Devices and Circuits*. (McGraw-Hill Education (India) Pvt Limited, 2008).
16. Amos, S. W. & James, M. *Principles of Transistor Circuits*. (Newnes, 2000).
17. MOSFET and Metal Oxide Semiconductor Tutorial. *Basic Electronics Tutorials* at <http://www.electronics-tutorials.ws/transistor/tran_6.html>

3 Literature Review

3.1 Introduction

Bismuth ferrite; BiFeO_3 (BFO), is a multiferroic material that exhibit ferroelectricity and antiferromagnetism. It is perhaps the only material that exhibit multiferroicity at room temperature. Bulk properties of BFO have been extensively studied but its electromechanical properties are hindered due to high leakage problems. This is mostly due to the difficulties in materials processing and non stoichiometric single phase bismuth ferrite ^{1,2}. Further research in the area of thin films resulted in enhanced fabrication methods and outstanding properties of epitaxial BFO heterostructure with high remnant polarization ³ establishing a renaissance among the scientific community. Such outcome opened the gate for a great deal interest and efforts to resume the investigation in the area.

Recently, it has been reported the size effect has a very strong influence in the magnetic properties of bismuth ferrite ^{4,5}. As a result there has been quick growth in the fabrication and characterization of BFO nanostructures such as cubes ⁶, fibers ^{7,8}, rods ⁹, tubes ⁴, and crystals ⁸.

Bismuth ferrite is also an attractive material for photoconduction applications because of its distinctive optical band gap compared to other ferroelectric materials. BFO possesses a band gap of 2.7 eV which falls in the visible range and absorbs significant amount of the light spectrum ^{10,11}.

This chapter attempts to summarize the characteristics, fabrication, and properties of BFO thin films and nanostructures.

3.2 Bismuth ferrite

The study of BFO started in 1960 by *Smolenskii et al.* but difficulties in the growth of single crystals resulting in high conductivity prevent the material for further investigation and practical applications¹². In 1967, *Achenbach* and colleagues succeed in the preparation of single phase polycrystalline BFO by removing unwanted phases by washing the material with nitric acid¹³. In 1970, the polarization for bulk BFO was reported to be $6.1 \mu\text{C}\cdot\text{cm}^{-2}$ ¹⁴. Precise x-ray diffraction studies in 1990 on monodomain single crystal revealed BiFeO_3 structure¹⁵. In 2003, the discovery of a large remnant polarization (15 times larger) along with strong ferromagnetism³ of thin films marked the beginning of a new age for bismuth ferrite as a multiferroic material.

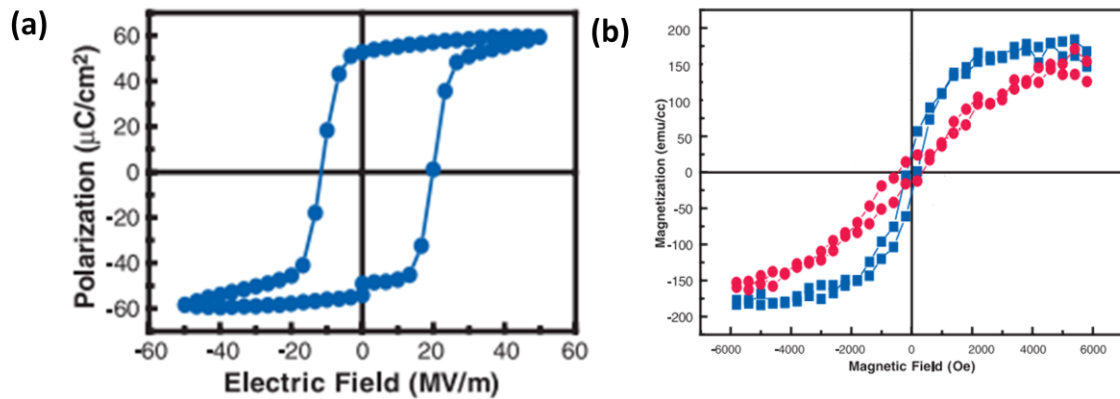


Figure 3.1 (a) Hysteresis loop measured at 15 kHz showing high remnant polarization $\sim 55 \mu\text{C}\cdot\text{cm}^{-2}$, and (b) magnetic hysteresis loop for 70 nm BFO film with an appreciable saturation magnetization of $150 \text{ emu}\cdot\text{cm}^{-3}$, and a coercive field of 200 Oe. **NOTE:** The in-plane loop is shown in blue, and the out-of-plane loop is in red.³

At room temperature bulk bismuth ferrite possesses a simple ABO_3 rhombohedral distorted perovskite structure with space group $R\bar{3}c$. The unit cell can be described as pseudo-cubic, rhombohedral or hexagonal where $[111]_{pc} \parallel [111]_{rh} \parallel [001]_{hex}$. The lattice constant determined by *Kubel and Schmid* are: $a_{pc} = 3.965 \text{ \AA}$, $\alpha_{pc} = 89.35^\circ$ for the pseudocubic unit cell, $a_{rh} = 5.6343 \text{ \AA}$, $\alpha_{rh} = 59.348^\circ$ in the rhombohedral unit cell and $a_{hex} = 5.578 \text{ \AA}$, $c_{hex} = 13.868 \text{ \AA}$ for the hexagonal unit cell¹⁵. When grown as a thin film, it has been shown that the structure could be monoclinic or tetragonal depending upon the strain imposed by the substrate^{16,17} and level of mismatching.

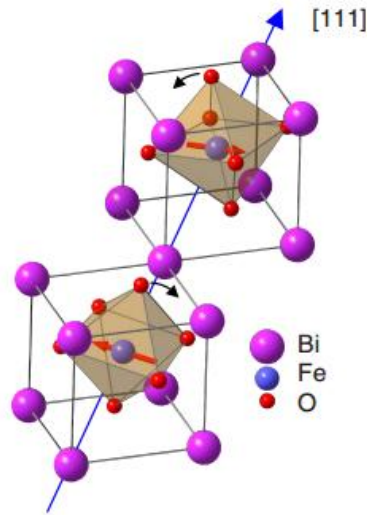


Figure 3.2 Perovskite crystal structure of bulk $BiFeO_3$ ¹⁸.

From a structural point of view an important parameter is the rotation angle of the oxygen octahedra. Equation 3.1 is used to measure how well the ions fit into the perovskite unit cell.

$$\frac{r_{Bi}+r_O}{l} \quad (3.1)$$

where r is the ionic radii of the respective ion and l is the length of the octahedral edge. This parameter is analogous to the tolerance factor as shown Equation 3.2. Using the Shannon atomic radii the tolerance for BiFeO₃ is equal to 0.88.

$$t = \frac{(r_{Bi}+r_O)}{\sqrt{2}(r_{Fe}+r_O)} \quad (3.2)$$

Bismuth ferrite shows spontaneous polarization along one of the eight pseudo-cubic [111] axes with a Curie temperature of 830 °C. Calculated spontaneous polarization is predicted to be about 100-150 $\mu\text{C.cm}^{-2}$ and has been confirmed in thin films³. The polarization in BiFeO₃ is caused by the lone pair (s^2 orbital) of Bi³⁺, so mostly from the A-site while the magnetization comes from the B-site (Fe³⁺). Bulk BFO exhibits G-type, antiferromagnetism with Néel temperature of 380 °C. In the G-type both the intraplane and interplane are antiferromagnetic; each Fe³⁺ with spin up is surrounded by six of the nearest Fe neighbors with spin down. The antiferromagnetic structure has a modulation vector with a periodicity of $\lambda = 0.62 - 0.64$ nm. There is a small canting of Fe magnetic moment leading to a net magnetization of 5 emu.cm^{-3} and some thin film exhibit larger saturation magnetization exceeding 70 emu.cm^{-3} ³. However, the origin for such a high magnetization value in thin films is not well defined and is cause of arguments.

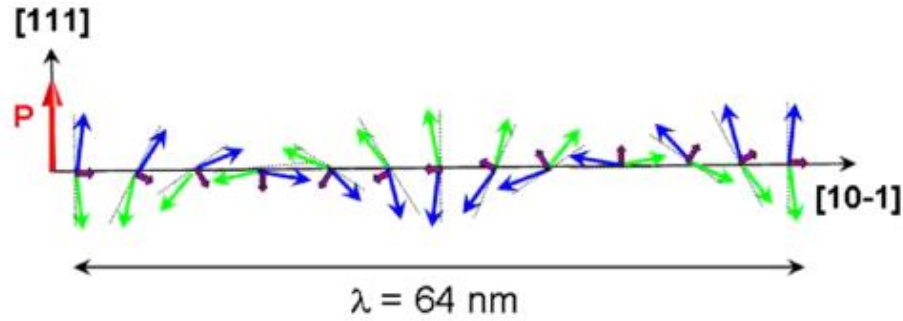


Figure 3.3 Schematic representation of bismuth ferrite spin cycloid ¹⁹. The canted antiferromagnetic spins (blue and green) give rise to a net magnetic moment (purple arrows) that is spatially averaged out to zero due to the cycloidal rotation.

Domain walls orientations have been derived considering the ferroelectric polarization directions pointing along any of the eight pseudocubic and the angles between allowed polarization directions of the ideal rhombohedral system ¹⁵. Such considerations lead to the following domain wall angles (orientations) $\pm 71^\circ$, $\pm 109^\circ$, or $\pm 180^\circ$ in correspondence with [011], [001] and [011] pseudocubic coordinates ²⁰. For each domain wall orientation there is a choice of atomic plane in which the domain can be centered on: BiO or FeO₂ plane in case of the 109° . In order to study the different possibilities, let's consider the different orientations individually ¹⁸.

- (1) 71° domain wall is constructed in the [011] plane. There are two different configurations of rotations of the oxygen octahedra: *continuous* and *changing*. In the continuous case the oxygen octahedral phase rotation remains unchanged in the changing case the phase reverses at the domain wall. The wall can be centered around either BiFeO or O₂ plane.
- (2) 109° domain wall is constructed in the [001] plane. There is also a *continuous* and *changing* configuration of rotations of the oxygen octahedra. In this case the domains can be centered on FeO₂ and O₂ planes.

(3) 180° domain wall constructed in the $[0\bar{1}\bar{1}]$ plane. Again, two octahedral tilt have been explored. Similar to the 71° domain wall is not possible to distinguish between the BiFeO and O_2 centered domain walls.

The domain walls play an important role in the electronic properties because of their size, local symmetry, individual properties, and due to the fact that their location can be controlled. In the case of BFO one of the unique properties within or in the domain wall for different walls orientations is the change in conductivity. *Ramesh* and coworkers have reported that certain domain walls of BFO are much more conductive than the domains²¹. The conductivity of the walls is related to the type of domains they are separated. Epitaxial BFO thin films carefully grown on $SrRuO_3$ (50 nm) as buffer layer bottom electrode and $SrTiO_3$ (100) oriented was used to study the conductivity of the domain walls. The films were grown by laser molecular beam epitaxy technique and ferroelectric domains were imaged by piezoelectric force microscopy (PFM). In order to study the three different types of domains characteristics of BFO (71° , 109° and 180°), controlled ferroelectric domains pattern were written using a PFM by applying a DC voltage. The presence of all three types of domains was confirmed by PFM imaging. Conductive atomic force microscope (c-AFM) shows the occurrence of conduction at 109° and 180° walls but not in 71° walls. The authors argue two reasons for the observed conductivity of the domains walls: (1) the polarization normal to the domain wall is not constant across the domain wall and as a result generates an electrostatic depolarization field that attracts charge carries and (2) the electronic bandgap is reduced for the 180° and 109° domain walls^{21,22}.

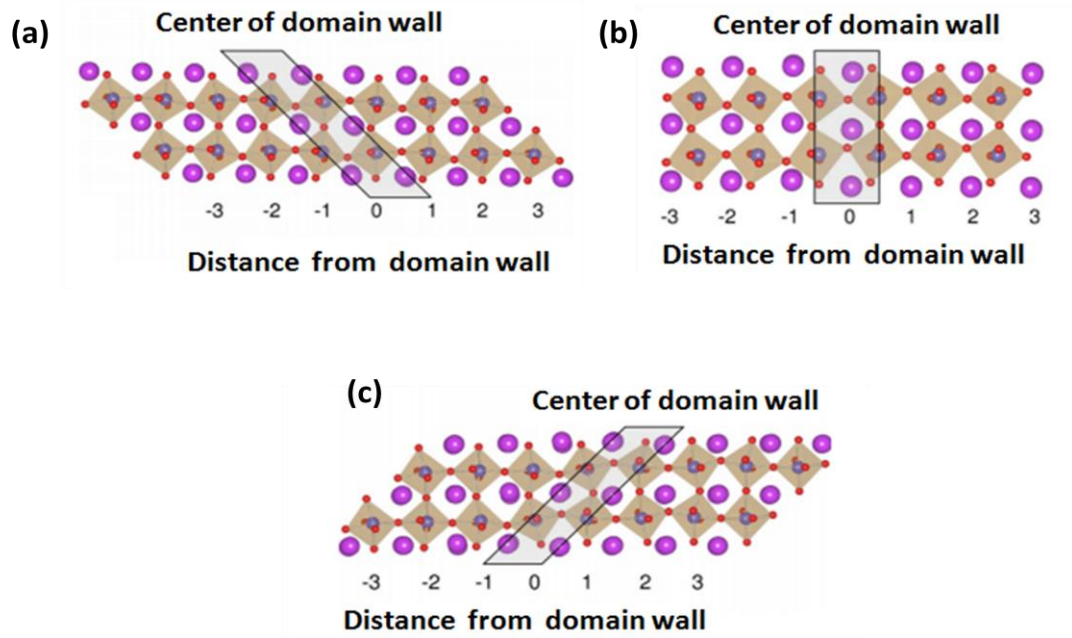


Figure 3.4 (a) 71° domain boundary with continuous oxygen octahedral rotations, (b) 109° domain boundary with continuous oxygen octahedral rotation centered on the FeO_2 plane, and (c) 180° domain boundary with continuous oxygen octahedral rotations¹⁸.

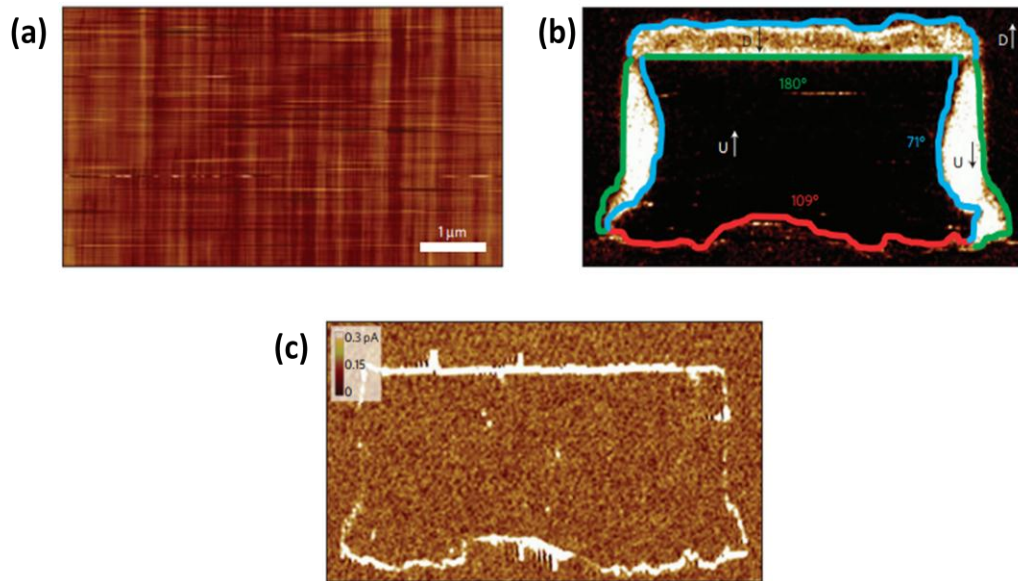


Figure 3.5 (a) Topography of BFO thin films with roughness (rms) of 0.5 nm, (b) In-plane PFM image of a written domain pattern in a mono-domain BFO (110) film showing all three types of domain wall, that is, 71° (blue), 109° (red) and 180° (green), and (c) corresponding c-AFM image showing conduction at both 109° and 180° domain walls; note the absence of conduction at the 71° domain walls.²¹

The piezoelectric constant, d_{33} of BFO thin film is relatively low between 15 - 60 pC/N compared to other perovskite ferroelectrics (KNN based) with values of 100 – 300 pC/N. The reason for low piezoelectric coefficient is likely to be the small dielectric constant, which affects piezoelectricity as indicated by Equation 3.3 ²²

$$d_{33}^{eff} = \frac{\partial s}{\partial E} = \frac{\partial s}{\partial P} \frac{\partial P}{\partial E} = 2Q\varepsilon P \quad (3.3)$$

where Q is the electrostrictive coefficient, s is the strain which is related to the polarization ($s=QP^2$), ε is the dielectric constant. The effective electrostrictive coefficient for BFO is $Q_{33}^{eff} = 1$ to $4 \times 10^{-2} \text{ m}^4/\text{C}^2$ determined by experiments and calculations ²³.

The dielectric constant of BFO at room temperature is ~ 30 which is small compared with those of typical perovskite ferroelectrics such as BaTiO_3 and $\text{Pb}(\text{Zr,Ti})\text{O}_3$. At higher temperatures, colossal dielectric constants have also been reported.

3.3 Bismuth ferrite nanostructures

Dimensionality plays a crucial role in certain material properties due to its effect on the electronic transport mechanism, domain switching, and arrangement of atoms ²⁴. Low dimensional systems are the smallest systems that can be employed for efficient charge transport and optical excitation ²⁵. With a decrease in the device dimension to the nanometer scale, the surface effects become critical by the limiting carrier transport mechanism ²⁵ which is often displayed in charge trapping or recombination.

The synthesis methods are classified in two main methods: “bottom-up” and “top down”. The “bottom up” method is particularly interesting because of the ability to manipulate properties such as shape, size, surface area, pore size, and surface modification of the end product. The “bottom up” method is based on chemical processes

while “top down” method refers to the mechanical crushing of source materials. The processing route selection depends on the desired chemical composition and features of the nanostructures.

Bismuth ferrite nanostructures including zero dimensions (0-D such as nanoparticles), one dimension (1-D such as nanorods, nanowires/fibers and nanotubes), and two dimensions (2-D such as thin films) can be synthesized by the bottom up method. Some of these nano shapes are being prepared by the use of electrospinning, sol-gel, tartaric acid assisted solution, hydrothermal synthesis, molten salt, microemulsion, RF sputtering, and pulsed laser deposition techniques^{3,26–29}.

It is noticeable that epitaxially grown bismuth ferrite thin films have been reported to be strong ferroelectric at room temperature³ as shown in Figure 3.1a, which makes the material to be practically useful. However, BFO still is limited by leakage current problems due to 1) fluctuations in the Fe ions from Fe^{3+} to Fe^{2+} , 2) large coercive fields, 3) presence of impurity phases such as $\text{Bi}_2\text{Fe}_4\text{O}_9$, $\text{Bi}_{24}\text{Fe}_2\text{O}_{39}$ and $\text{Bi}_{25}\text{FeO}_{40}$ ³⁰, and 4) smaller electromechanical coefficients compared with traditional Pb-based materials. There have been several attempts to alleviate these challenges in the development of bismuth ferrite nanostructures such as:

1. Doping ions into Bi and/or Fe sites of the BiFeO_3 ^{31–34};
2. Forming solid solution with other perovskite structures such as, PbTiO_3 ³⁵
 $\text{Bi}_{0.5}\text{K}_{0.5}\text{TiO}_3$ ³⁶;
3. Formation of multilayers^{29,37};
4. Used of buffer layer such as SrRuO_3 ³, BNT³⁸ BaTiO_3 ³⁹;

5. Controlled ambient atmosphere or annealing environment during film deposition.

Besides the ability to manipulate the properties and features of materials in the nanoscale, the main purpose in fabricating bismuth ferrite in the 0-D, 1-D and 2-D scale is to enhance the anti/ferromagnetic properties. When the particle size is reduced to less than the periodicity of the magnetic spin order, the helical order is suppressed and the magnetization of the nanoparticles become sizeable^{4,5}.

3.3.1 Zero dimension structures (0-D)

A size dependent on the magnetic properties of single crystalline multiferroic bismuth ferrite nanoparticles is reported by *Park et al* (2007)⁴. Nanoparticles were synthesized by sol gel methodology based on glycol reaction and size was thermodynamically controlled in a range of 15 to 100 nm. Individual nanoparticles were identified as a rhombohedral perovskite phase. The magnetization response as a function of applied magnetic field for different nanoparticles size was observed to systemically increase while decreasing the size as shown in Figure 3.6. The response is initiated when the size of the particles is less than 95 nm and rapidly increases for samples with particle size lower than 62 nm.

To further confirm the coupling between magnetic and electric properties in the nanoparticles reported Raman measurements are shown in Figure 3.7. The peak at 136 cm^{-1} is the first normal A_1 mode for rhombohedral structure and responsible for the magnetic coupling. The 136 cm^{-1} peak intensity is decreasing with decreasing particle size as an indicative of the suppression in the contribution of Bi-O1 vibrational mode.

Park et al attributed the enhanced coupling to the size confinement considerations along with the lattice distortion in the nanoparticles.

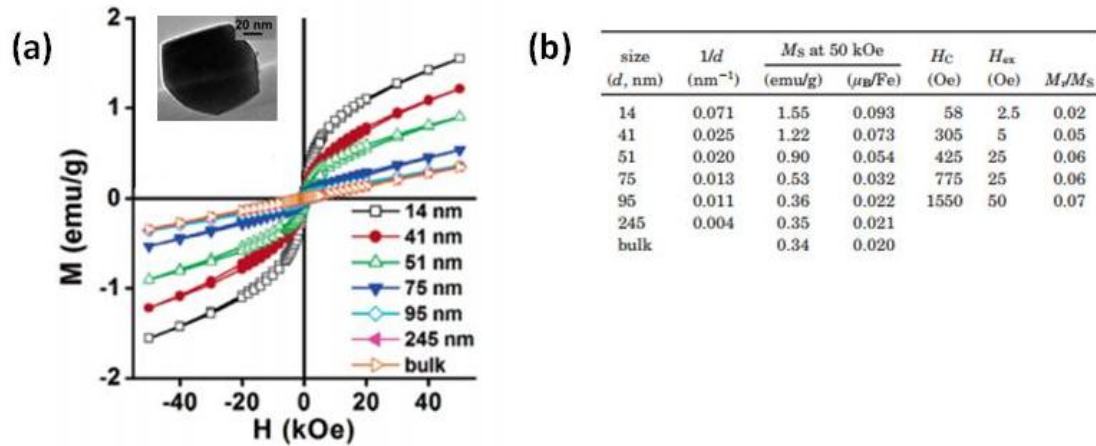


Figure 3.6 (a) Hysteresis loop at 300 K for bismuth ferrite nanoparticles, and (b) Size, *d* represents the diameter of the as-prepared nanoparticles. *M_s* is the magnetization observed at *H* = 50 kOe. *H_c* and *H_x* represent derived coercivities and exchange bias parameters, respectively.

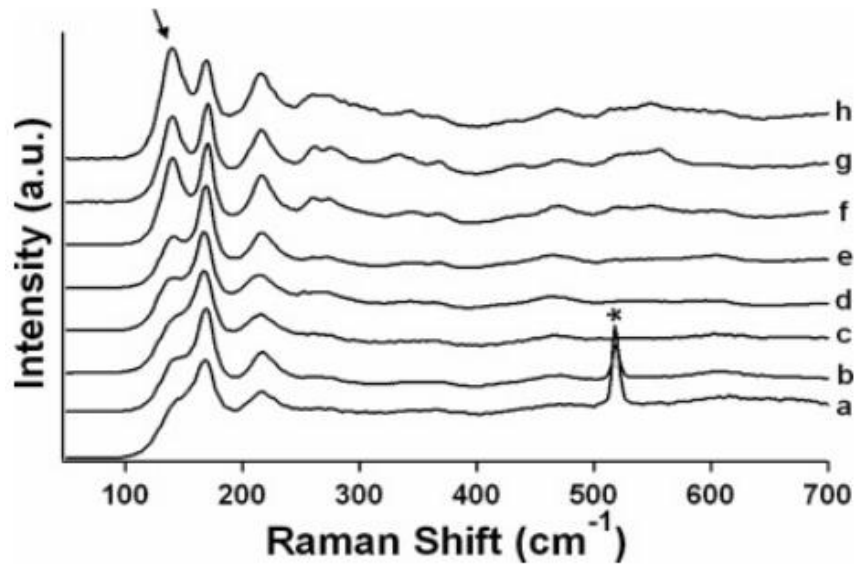


Figure 3.7 Raman Spectra of bismuth ferrite nanoparticles with size of: (a) 14 nm, (b) 41 nm, (c) 51 nm, (d) 75 nm, (e) 95 nm, (f) 245 nm, and (g) 342 nm, respectively as well as of the bulk (h). The Si peaks are identified with an asterisk. The arrow is referring to the *A₁* mode at 136 cm⁻¹.

Figure 3.8a shows the absorption spectrum of bulk and 16 nm nanoparticle of bismuth ferrite in which the vibrational excitations are assigned based on calculations. With decreasing nanoparticle size, the spectral shape begins to display “three band character”, indicative of a size induced approach to the paraelectric phase ⁴⁰. The $A_1(\text{TO1})$ mode display in Figure 3.8b softened by more than 6% and dampens considerably. The shift in red curve of the $A_1(\text{TO1})$ peak is assigned as the soft mode driving the ferroelectric transition.

Surface strain by finite size induces changes in the electronic structure of bismuth ferrite. The Figure 3.9 displays the optical absorption coefficient for a 16 nm particle and for epitaxially grown bismuth ferrite thin film ⁴¹. The splitting of 3.2 and 4.5 eV bands in BFO film is assigned to minority channel dipole which allowed charge transfer excitation ⁴¹. The 3.2 eV splits to smaller features with centered at 2.9 eV and 3.4 eV. Such splitting is due to lattice distortion related to the FeO_6 octahedra ⁴².

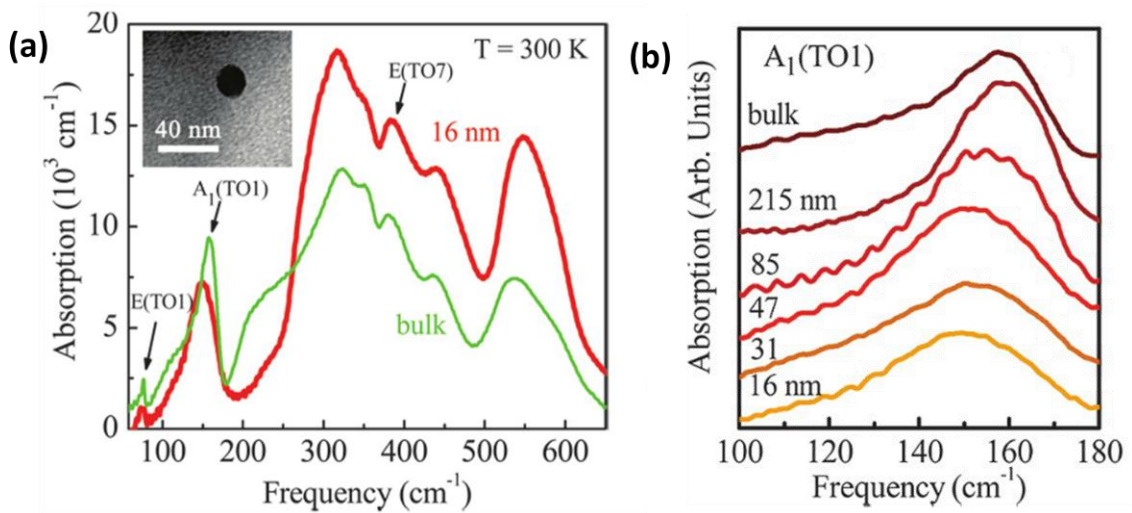


Figure 3.8 (a) Absorption coefficient at 300 K for bulk and 16 nm bismuth ferrite, and (b) close up view of $A_1(\text{TO1})$ phonon mode at 300 K ⁴⁰.

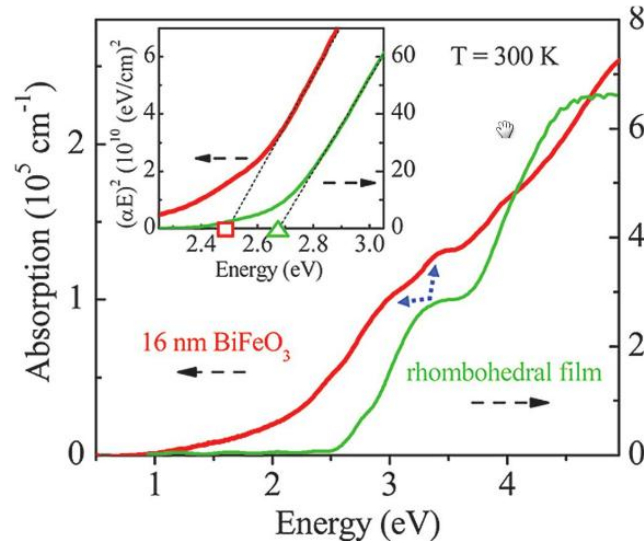


Figure 3.9 Absorption coefficient of 16 nm bismuth ferrite nanoparticle as compared with epitaxially grown rhombohedral thin film. Inset: Direct band gap analysis of the thin film and nanoparticles ⁴⁰.

3.3.2 One dimension structures (1-D)

Park et al was the first group that successfully synthesized bismuth ferrite 1D nanostructures (tubes) ⁴³. The tubes were prepared by sol-gel technique and porous anodic aluminum oxide template (AAO). Templates were completely removed by immersion in NaOH, leaving the tubes in a pile which was hard for characterizing the electrical properties. Tubes with diameter pores of 100 to 200 nm are polycrystalline with some amorphous content.

S. H. Xie et al. ⁴⁴ was one of the first group who reported the fabrication of BFO fibers with the objective of improving their ferromagnetism by decreasing the crystallite size within the fibers. Ultra-fine fibers were synthesized by sol gel based electrospinning technique. Bismuth nitrate – $\text{Bi}(\text{NO}_3)_3 \cdot 5\text{H}_2\text{O}$ and iron nitrate – $\text{Fe}(\text{NO}_3)_3 \cdot 9\text{H}_2\text{O}$ were dissolved in 2-methoxyethanol. The molar ratio of Bi:Fe was kept to be 1.05:1. A mixture of ethanol, glacial acetic acid and polymer – poly(vinyl pyrrolidone) was added to

the nitrates solution and stirred continuously. The solution was then loaded into a syringe equipped with a needle. The needle was connected a high voltage supply and ground connected to a metal collector in the opposite site. The voltage was increased up to 1.4 kV/cm and fibers were collected in glass flake (collector). The as spun fibers were heat treated in air, nitrogen, and argon (120 °C for 4 hours, 350 °C and 550 °C for 2 hours). Scanning electron microscopy in Figure 3.10a shows uniform ultra-fine fibers round in shape and straight over few micrometers in length. Fired fibers have diameters in a range of 100 to 300 nm. Crystalline fibers are obtained and impurities are reduced for fibers fired under Ar atmosphere. High voltage PFM demonstrated the ferroelectric and piezoelectric behavior of BFO nanofibers. The linear piezoelectric coefficient was estimated to be around 22 pC/N, which is smaller than those reported for BFO epitaxial thin films. Weak ferromagnetism with saturation magnetization of 4 emu/g and coercive field of 200 Oe was measured (Figure 3.10b). The enhanced magnetization may be attributed to an intrinsic effect due the presence of impurities such as $\gamma\text{-Fe}_2\text{O}_3$.

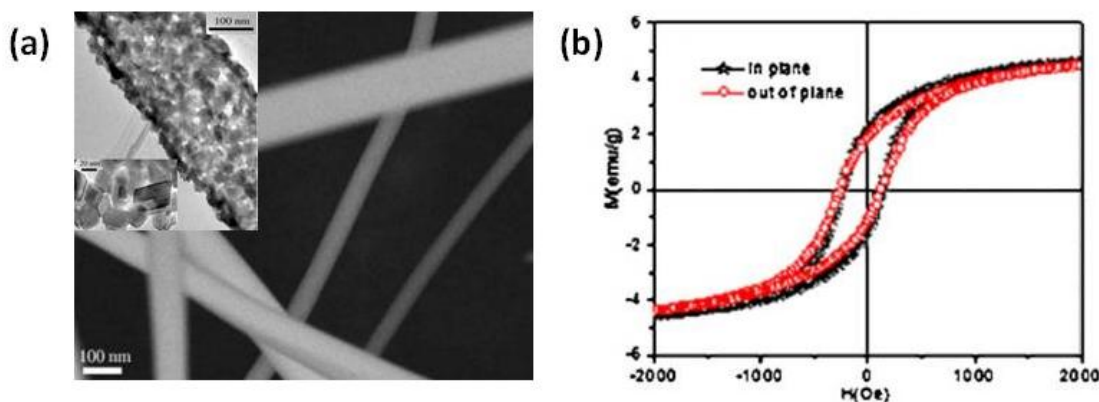


Figure 3.10 (a) Scanning electron microscope image of crystallized bismuth ferrite nanofibers, and (b) magnetic hysteresis loop⁴⁴.

Dopant ion substitution engineering as another possibility that can significantly enhance the magnetic, electric, and magnetoelectric properties of BFO is also investigated in 1D structures. In view of variety of possibilities, *Das et al*⁴⁵ reported the diameter dependent on the optical, magnetic, and magnetodielectric properties of Pr-Cr co-doped bismuth ferrite nanowires prepared via wet chemical template assisted route. Single phase rhombohedral structure Pr-Cr BFO nanowires of 18, 35, 55, 100, 150, and 250 nm were prepared. Co-doping causes a bond length change in the atoms of BFO crystal structure confirmed by a shift in the Raman peaks. The peak related with the Bi-O1 vibrational mode around 130 cm^{-1} in the 200 nm, responsible for the magnetoelectric coupling in the sample was found to shift towards a lower frequency as the nanowires diameter increases. The gradual decrease in the peak intensity is probably due to the grater lattice distortion or enhanced coupling between ferroelectric and magnetic order. The magnetic response was enhanced by decreasing the nanowire diameter and maximum saturation magnetization of 0.57 emu/g was obtained.

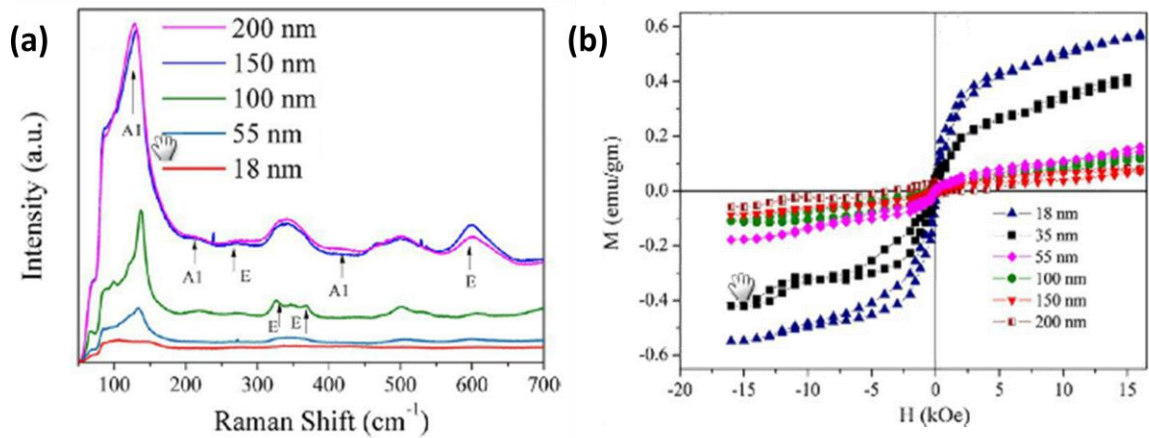


Figure 3.11 (a) Diameter dependence of the room temperature raman spectra of the co-doped bismuth ferrite nanowires, and (b) diameter dependent variation of the magnetic hysteresis loops of the co-doped nanowires measured at 300K⁴⁵.

Replacing/Codoping Bi^{3+} with Pr ion and Fe^{3+} with Cr ion changes the canting angle and increases the degree of the distortion which results in a smaller bond angle of the antiferromagnetic Fe-O-Fe chain of spins leading to enhanced magnetization ⁴⁵.

3.3.3 Two dimension structures (2-D)

In previous section the effect of ion substitution was discussed for 1D structure. Ion substitution in the A and/or B site of the perovskite BiFeO_3 is a widely explore alternative route to obtain low leakage current with high ferroelectric properties in 2D structures (thin films) as well. A-site substitution refers to the case where Bi^{3+} ions are replaced by other elements. A-site substitution by ions with smaller ionic radius can cause more buckling in the Fe-O-Fe angle which results in a smaller tolerance factor ⁴⁶. A small tolerance factor favors a more insulator character in BFO. Replacing Bi^{3+} by divalent ions might produce hole-doped BFO while substitution with higher valence like 4+ might produce electron carriers ⁴⁶ unless other defects as oxygen vacancies are produced. On the other hand, B-site substitution refers to the case in which Fe^{3+} ions are replaced by other transition metals. The d-orbital state of the Fe^{3+} ion plays an important role on the physical properties of BFO by changing its electronic structure. The composition tuning through A or B site substitution in perovskite ferroelectric is known to achieve a region called morphotropic phase boundary (MPB) in which properties are enhanced (maximized). An MPB region is also expected when A or B-site substitution in BiFeO_3 occurred.

Epitaxial thin films of $\text{Bi}_{(1-x)}\text{Sm}_x\text{FeO}_3$ with varying Sm content were fabricated on (100) oriented STO substrate with 50 nm SRO as bottom electrode^{47,48}. Sm^{3+} has a smaller ionic radius of 1.24 Å compared to Bi^{3+} that possess a value of 1.36 Å. Thus, doping to replace the A-site with Sm^{3+} is expected to cause a distortion in the octahedral angle but also can alter the long-range ferroelectric order. Hysteresis loops for compositions of $x = 0.1, 0.14$, and 0.16 shown in Figure 3.12 shows a transition from ferroelectric to antiferroelectric phase as Sm content is increased. Increasing Sm content causes the coercive field to drop but the polarization is maintained. Measured dielectric constant and piezoelectric coefficient, d_{33} values reached a maximum (Figure 3.13) for a composition value of $x = 0.14$. Sm^{3+} substituted BFO has good properties compared to other popular dopants such as La ⁴⁹ or Nd .

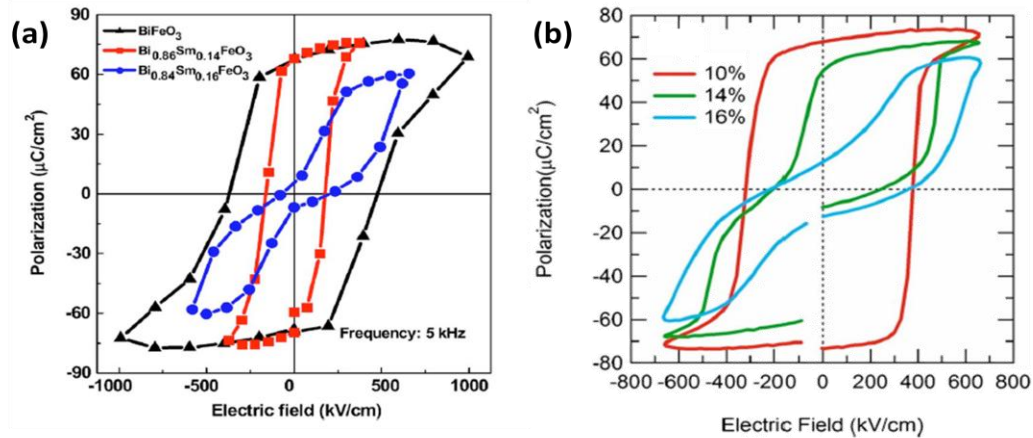


Figure 3.12 Polarization hysteresis loops compositions of $x = 0.1, 0.14$ and 0.16 (a) 5 kHz⁴⁷, and (b) 25 kHz⁴⁸.

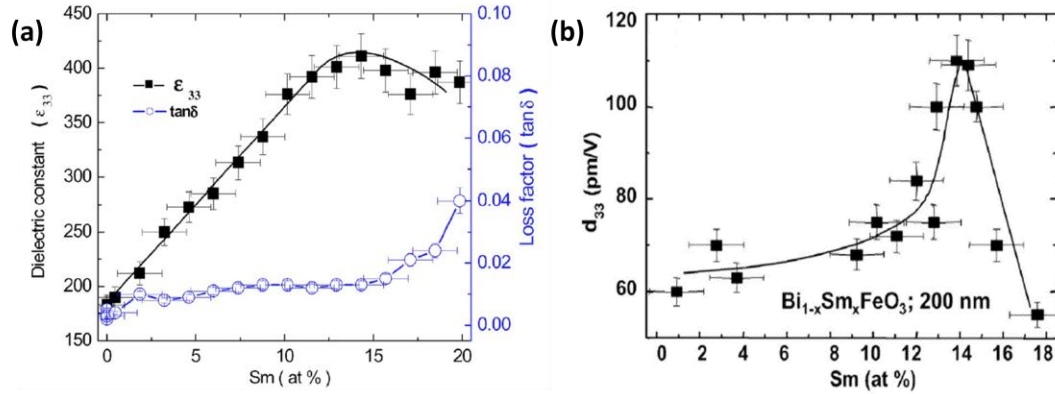


Figure 3.13 (a) Dielectric constant ϵ_{33} and $\tan \delta$ measured at 1 MHz (zero bias), and (b) High field d_{33} determined from piezoelectric hysteresis loop measured as a function of composition (not shown here) ⁴⁷.

At this point, it is clear that ion doping improves the ferroelectric properties and reduces the leakage current. Considering that PZT is the most studied ferroelectric material with low leakage current, useful for practical applications it could be integrated in a binary system with BFO based compositions. Solid solution of PZT and La doped BFO composite thin films deposited on Pt/TiO₂/SiO₂/Si greatly decrease the leakage current and improve the electrical properties as shown in Figure 3.14a. Composite thin films of 0.60Bi_{0.90}La_{0.10}FeO₃-0.40Pb(Zr_{0.52}Ti_{0.48})O₃ (BLFO-PZT) were deposited without a buffer layer through RF sputtering ³⁵. There is an enhancement in the dielectric constant with a value of ~527 and a dielectric loss of ~1.9 % at 1 kHz (Figure 3.14b) which is much larger than those of pure BFO and BLFO.

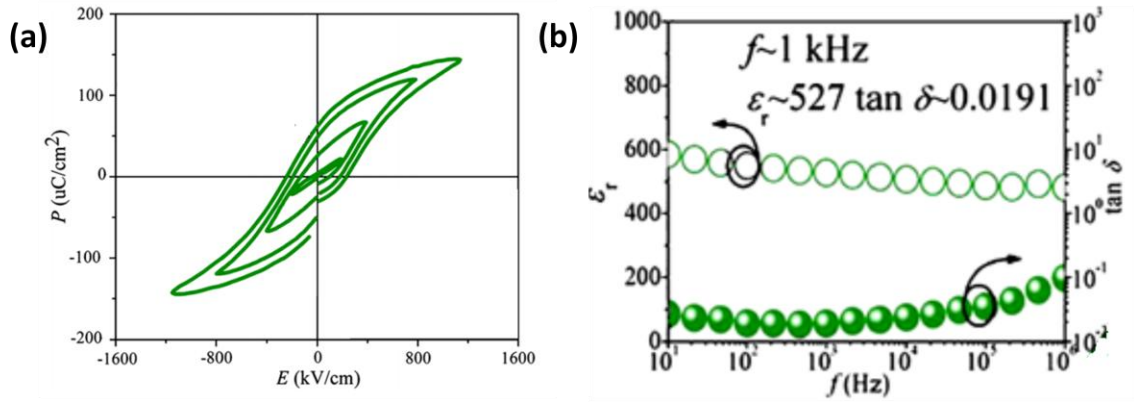


Figure 3.14 (a) Hysteresis loop of BLFO-PZT thin films measured at 5 kHz, and (b) Dielectric properties measured at 1 kHz ³⁵

Matsuo et al, investigated the ferroelectric properties of $x\text{BKT}-(1-x)\text{BFO}$ solid solution in the form of ceramics. The results obtained from TEM, X-ray and neutron powder diffraction indicate that morphotropic phase boundary (MPB) region exists between $0.4 < x < 0.43$. Ceramics with MPB composition exhibited superior properties with remnant polarization of $52 \mu\text{C}\cdot\text{cm}^{-2}$ and k_{33} of 0.36 at room temperature ³⁶. Such results stimulate the study of BKT-BFO solid solution in the form of thin films.

Multilayer thin films of BFO and one or more ferroelectric layers have been showed to exhibit enhanced properties ^{29,37}. However, the coupling and interaction among the layers can strongly influence the growth and physical properties of the thin films. Well studied lead free ferroelectric materials such as $(\text{Bi}_{0.5}\text{K}_{0.5})\text{TiO}_3$ (BKT), BaTiO_3 (BT), and $(\text{Bi}_{0.5}\text{Na}_{0.5})\text{TiO}_3$ (BNT) are some of the potential candidates to combine in a multilayer design with BFO, although other ferromagnetic materials are also considered. The ferroelectric and dielectric properties of BNT and BKT ceramics are known to be moderated in comparison with PZT compositions. BKT and BNT ceramics possess a relatively high dielectric constant of 770 and 580 and longitudinal piezoelectric d_{33}

coefficient, of 80 and 70 pC/N, respectively ⁵⁰. BNT-BKT-BT thin films has shown remnant polarization values of $\sim 30 \mu\text{C}\cdot\text{cm}^{-2}$ ^{51,52}.

BFO/BNT bi-layered thin films deposited by radio frequency (RF) sputtering on Pt/TiO₂/SiO₂/Si substrate without any buffer layer exhibit a strong (111) orientation and enhanced properties ²⁹. A 60 nm BNT layer was first deposited at 650 °C and then 200 nm thick BFO layer was subsequently deposited on the BNT/Pt/TiO₂/SiO₂/Si at the same temperature. Bi-layered was deposited at a RF power of 120 W, a based pressure of 10^{-6} Torr and deposition pressure of 10 mTorr with Ar and O₂ at the ratio of 7:1. XRD studies showed a pure perovskite structure with no impurity phases. However, BFO directly deposited on Pt/TiO₂/SiO₂/Si exhibited a mixture of pyrochlore and perovskite phase. BFO single layer showed poor ferroelectric properties (Figure 3.15b) while BFO/BNT bi-layered exhibited properties comparable with similar thin film samples as shown in Figure 3.15c. Improvement in the remnant polarization values is attributed to the crystallinity and to the development of space charge in the interface between the layers.

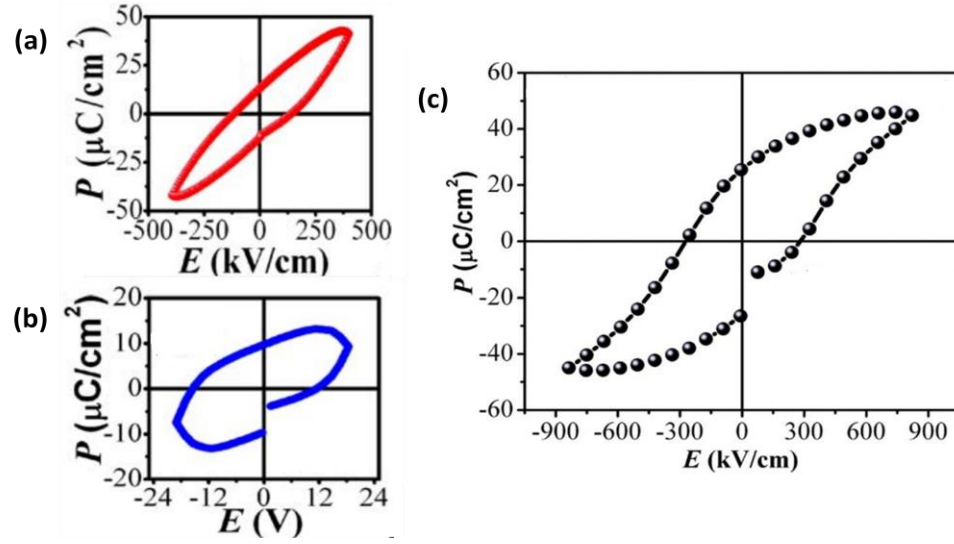


Figure 3.15 (a) Hysteresis loops for (a) single layer BNT thin film, (b) single layer BFO thin film, and (c) bi-layered BFO/BNT thin film²⁹.

BNT-BT is another well-established ferroelectric composition that shows excellent ferroelectric properties. It has been used as a buffer layer with the goal of reducing leakage current⁵³ in bi-layered system of $\text{BiFeO}_3/[(\text{Bi}_{0.5}\text{Na}_{0.5})_{0.94}\text{Ba}_{0.06}]\text{TiO}_3$. Thin films were grown by a combined route of sol-gel and RF sputtering. The BNT-BT layer was grown by sol-gel and BFO by RF sputtering with thickness of 150 nm and 280 nm respectively. Single BNT-BT layer exhibits a polycrystalline phase, while secondary phase of $\text{Bi}_{25}\text{FeO}_{40}$ was formed in BFO single layer. The electric properties of bi-layered BFO/BNT-BT in Figure 3.16 shows properties as: $\epsilon_r = 178$, $\text{Pr} = 40 \mu\text{C}.\text{cm}^{-2}$, and $E_c = 386 \text{ kV/cm}$ ³⁸. Experimental values for dielectric constant are lower than those calculated when assuming a series composite connectivity of BNT-BT and BFO layers. Simply series connection cannot be considered. The temperature dependence shown in Figure 3.16b can be described by the Arrhenius equation:

$$\sigma_{dc} = \sigma_o \exp \left(-\frac{E_a}{k_B T} \right) \quad (3.4)$$

where σ_0 and k_B are constant, and E_a is the activation energy of conduction, which can be calculated from the slopes of the plot in Figure 3.16b. The activation energies for grain and grain boundaries were calculated as ~ 0.75 and ~ 0.74 eV respectively³⁸. Certainly, oxygen vacancies can be formed steadily in BFO thin films leading to the formation of conduction electrons.

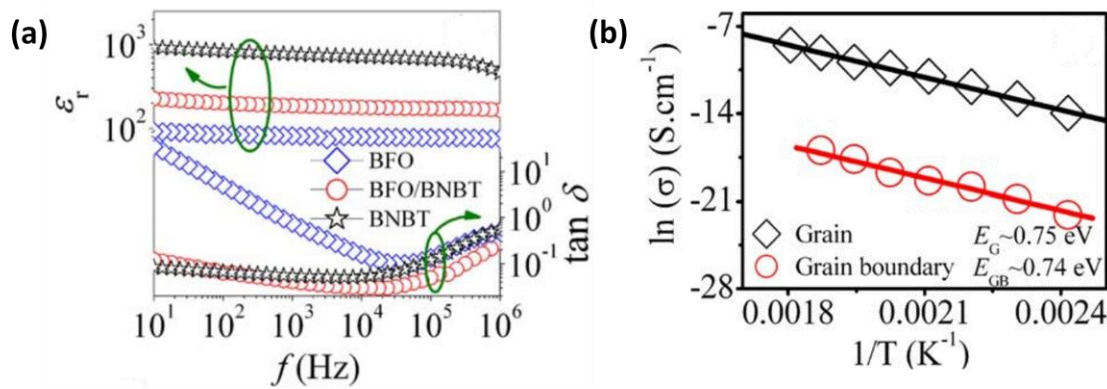


Figure 3.16 (a) Frequency dependent of dielectric behavior, and (b) dc conductivity vs $1/T$ at different frequencies for the bi-layered BFO/BNTBT thin film³⁸.

Bismuth ferrite thin films in the thickness range of 50 to 500 nm grown on SrRuO_3 (SRO) was deposited on SrTiO_3 [100] (STO) substrate by pulsed laser deposition by Wang *et al*³ exhibit outstanding ferroelectric properties. A 50 nm layer of SRO buffer layer/bottom electrode as deposited at 600 °C in an oxygen ambient of 100 mTorr followed by the BFO layer (70, 100, and 200 nm), deposited at 670 °C in an oxygen ambient of 20 mTorr. X-ray diffraction (XRD) as a function of film thickness in Figure 3.17a showed only diffraction peaks from the substrate [001] and pseudocubic reflections which confirm the epitaxial nature of the BFO film. Detailed XRD analysis suggests a tetragonal like crystal structure with a small monoclinic distortion. The presence of the SRO layer induced a compressive stress which causes the in plane lattice parameter smaller than that of BFO. By decreasing the film thickness the degree of compressive

stress is decreased. The ferroelectric hysteresis loop was measured at 15 kHz and 200 nm film showed a remnant polarization of $50 - 60 \mu\text{C}\cdot\text{cm}^{-2}$ shown in Figure 3.1. Piezoelectric hysteresis loop in Figure 3.17b showed a remnant out of plane piezoelectric coefficient, d_{33} of 70 pm/V. The piezoelectric coefficient decreases as the film thickness decrease, while the polarization follows opposite trend ³.

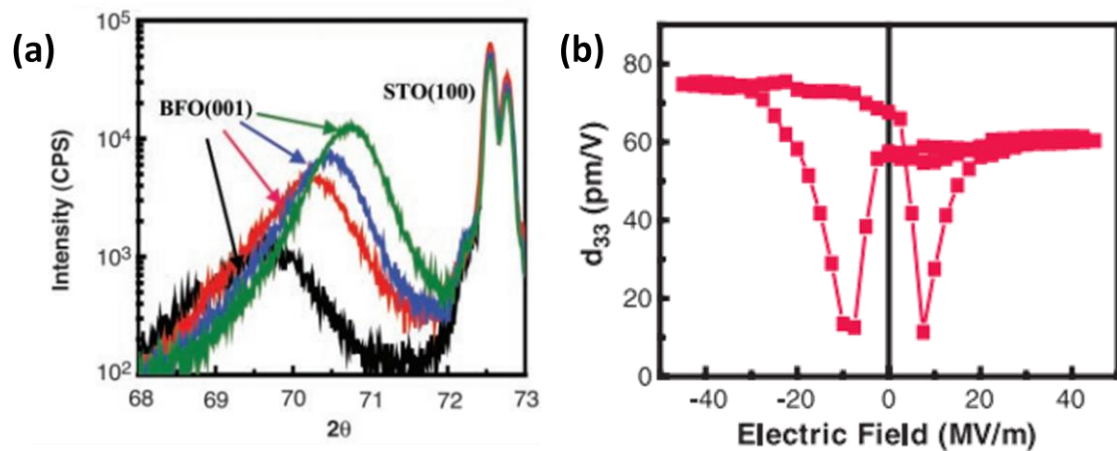


Figure 3.17 (a) [003] peaks from x-ray scans showing the effect of film thickness on epitaxial strain. As the film thickness increased, the peak position progressively increases (black line, 70 nm; red line, 100 nm; blue line, 200 nm; and green line, 400 nm), and (b) small signal d_{33} for a $50 \mu\text{m}$ capacitor ³.

The growth window to obtain pure phase BFO thin film is limited. Bismuth related impurities results in large leakage current while iron related causes artifacts magnetic measurements. Recent studies have focused in the influence of growth temperature and ambient oxygen pressure to suppress the presence of impurities. *Béa et al* ⁵⁴ mapped out the pressure – temperature phase diagram (Figure 3.18) for BFO thin films grown by pulsed laser deposition. The mapping is complex and clearly illustrates the difficulty for optimizing the temperature and oxygen pressure to obtain pure BFO phase thin films by pulsed laser deposition ⁵⁴.

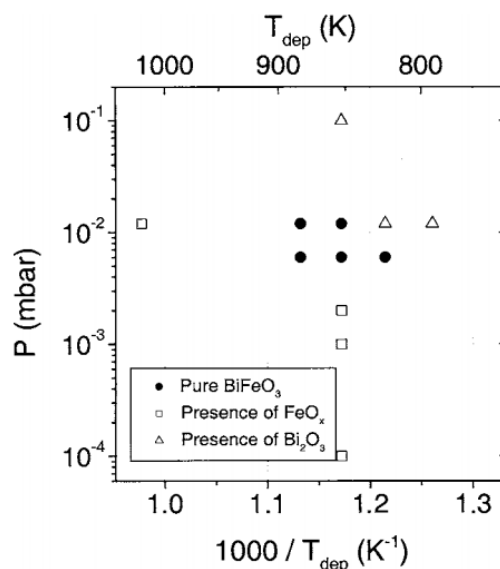


Figure 3.18 Pressure-temperature phase diagram for BFO thin films with a thickness of 70 nm⁵⁴.

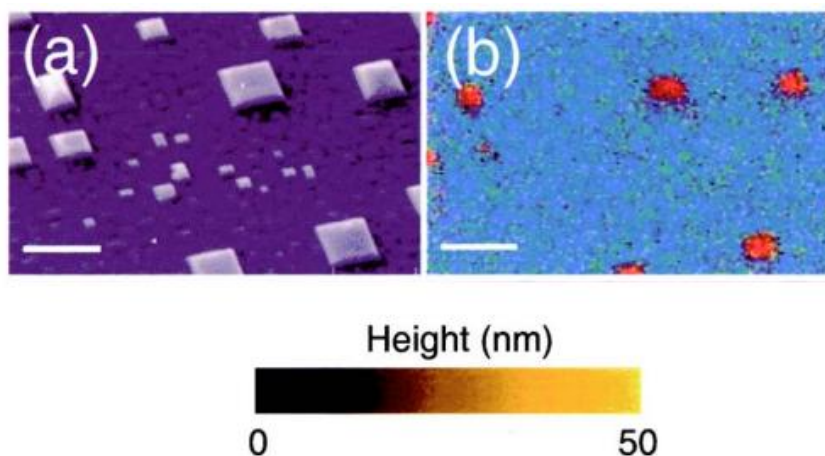


Figure 3.19 Scanning electron microscope image (a) surface of the films with low roughness regions and of ~100 nm high square outgrowths, (b) red-green-blue image constructed by superimposing colored element-selective mapping (red: Bi; green: Fe; blue: O). **NOTE:** white scale bar corresponds to 1 μm ⁵⁴.

Colored mapping in Figure 3.19 indicates that outgrowth blocks are Fe deficient and corresponds to a BiO_x phase. The areas between the blocks are homogenous in composition. The electrical properties of BFO thin films grown by PLD were later investigated by *You et al*⁵⁵ and are presented in Figure 3.20.

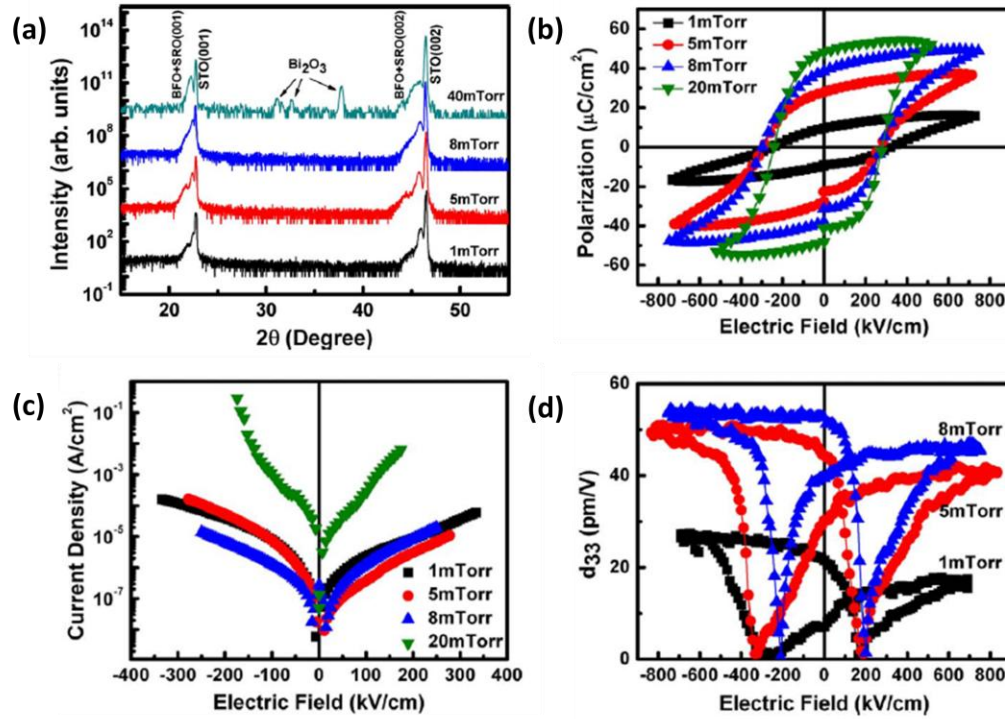


Figure 3.20 (a) XRD patterns of BFO epitaxial films grown under different oxygen pressures, (b) Ferroelectric polarization, (c) leakage current density, and (d) piezoelectric coefficient d_{33} as a function of electric field measured at 50 kHz ⁵⁵.

Pure phase BFO thin film is obtained in a wide range of oxygen pressure between 1 – 20 mTorr at 700 °C as shown in Figure 3.20a. As the oxygen pressure decrease the remnant polarization decreases as shown in Figure 3.20b. But, the leakage current in Figure 3.20c does not follow similar trend. Although, pure phase was obtained at minimum oxygen pressure, the Bi/Fe ratio was found to decrease as deposition pressure decreases. Leakage current in Bi-deficient samples are much smaller than those stoichiometric or Bi-rich ones.

3.4 Summary

This chapter aimed to provide a general overview of the most important characteristics and outstanding electronic properties of bismuth ferrite. It is difficult to review a topic that is so popular and is continuing to develop rapidly. So, rather some of the work that has been done and is pertinent to this investigation was considered.

There has been a progress during BFO history which resulted in a better understanding of the structure and ferroelectric origin. Advances characterization tools such as PFM enables the study of domains walls which revealed a unique conduction phenomenon in BFO due to electrostatic field build up within the walls. This conduction mechanism provides a possibility to integrate BFO in a variety of electronic devices, and not only for storage, memory, and spintronics applications.

Although, reduced leakage current and good electromechanical properties are obtained, often this is not the case for different processing routes. Outstanding results are difficult to reproduce, thus causing more effort to be done in this regard. Some of these efforts were briefly discussed in this chapter such as: ion doping, formation of multilayer design, thin film composite, and controlled growth atmosphere for 0-D, 1-D and 2-D bismuth ferrite nanostructures.

3. 5 References

1. Selbach, S. M., Einarsrud, M.-A. & Grande, T. On the Thermodynamic Stability of BiFeO₃. *Chem. Mater.* **21**, 169–173 (2009).
2. Ting Liu, Y. X. Low-Temperature Synthesis of BiFeO₃ via PVA Sol–Gel Route. *J. Am. Ceram. Soc.* **93**, 3637 – 3641 (2010).
3. Wang, J. *et al.* Epitaxial BiFeO₃ Multiferroic Thin Film Heterostructures. *Science* **299**, 1719–1722 (2003).
4. Park, T.-J., Papaefthymiou, G. C., Viescas, A. J., Moodenbaugh, A. R. & Wong, S. S. Size-Dependent Magnetic Properties of Single-Crystalline Multiferroic BiFeO₃ Nanoparticles. *Nano Lett.* **7**, 766–772 (2007).
5. Jaiswal, A. *et al.* Effect of Reduced Particle Size on the Magnetic Properties of Chemically Synthesized BiFeO₃ Nanocrystals. *J. Phys. Chem. C* **114**, 2108–2115 (2010).
6. Joshi, U. A., Jang, J. S., Borse, P. H. & Lee, J. S. Microwave synthesis of single-crystalline perovskite BiFeO₃ nanocubes for photoelectrode and photocatalytic applications. *Appl. Phys. Lett.* **92**, 242106 (2008).
7. Baji, A. *et al.* One-dimensional multiferroic bismuth ferrite fibers obtained by electrospinning techniques. *Nanotechnology* **22**, 235702 (2011).
8. Zhang, X., Bourgeois, L., Yao, J., Wang, H. & Webley, P. A. Tuning the Morphology of Bismuth Ferrite Nano- and Microcrystals: From Sheets to Fibers. *Small* **3**, 1523–1528 (2007).
9. Dutta, D. P. *et al.* Effect of doping on the morphology and multiferroic properties of BiFeO₃ nanorods. *Nanoscale* **2**, 1149 (2010).
10. Fruth, V. *et al.* Preparation of BiFeO₃ films by wet chemical method and their characterization. *J. Eur. Ceram. Soc.* **27**, 937–940 (2007).
11. J. F. Ihlefeld, N. J. P. Optical band gap of BiFeO₃ grown by molecular-beam epitaxy. *Appl. Phys. Lett. - APPL PHYS LETT* **92**, 2908–142908 (2008).
12. GA Smolenskii, Isupov, V. & Agrnovskaya, A. Ferroelectrics of the oxygen octahedral type with layered structure. *Sov. Phys. Solid State* **1**, 650–655 (1959).
13. Achenbach, G. D., James, W. J. & Gerson, R. Preparation of Single-Phase Polycrystalline BiFeO₃. *J. Am. Ceram. Soc.* **50**, 437–437 (1967).
14. Teague, J. R., Gerson, R. & James, W. J. Dielectric hysteresis in single crystal BiFeO₃. *Solid State Commun.* **8**, 1073–1074 (1970).
15. Kubel, F. & Schmid, H. Structure of a ferroelectric and ferroelastic monodomain crystal of the perovskite BiFeO₃. *Acta Crystallogr. Sect. B* **46**, 698–702 (1990).
16. Paudel, T. R., Jaswal, S. S. & Tsymbal, E. Y. Intrinsic defects in multiferroic BiFeO₃ and their effect on magnetism. *Phys. Rev. B* **85**, 104409 (2012).
17. Jang, H. W. *et al.* Strain-Induced Polarization Rotation in Epitaxial (001) BiFeO₃ Thin Films. *Phys. Rev. Lett.* **101**, 107602 (2008).
18. Lubk, A., Gemming, S. & Spaldin, N. A. First-principles study of ferroelectric domain walls in multiferroic bismuth ferrite. *Phys. Rev. B* **80**, 104110 (2009).
19. Lebeugle, D. *et al.* Electric-Field-Induced Spin Flop in BiFeO₃ Single Crystals at Room Temperature. *Phys. Rev. Lett.* **100**, 227602 (2008).
20. Streiffer, S. K. *et al.* Domain patterns in epitaxial rhombohedral ferroelectric films. I. Geometry and experiments. *J. Appl. Phys.* **83**, 2742–2753 (1998).
21. Seidel, J. *et al.* Conduction at domain walls in oxide multiferroics. *Nat. Mater.* **8**, 229–234 (2009).

22. Catalan, G. & Scott, J. F. Physics and Applications of Bismuth Ferrite. *Adv. Mater.* **21**, 2463–2485 (2009).
23. Bark, C. W., Ryu, S., Koo, Y. M., Jang, H. M. & Youn, H. S. Electric-field-induced structural modulation of epitaxial BiFeO₃ multiferroic thin films as studied using x-ray microdiffraction. *Appl. Phys. Lett.* **90**, 022902 (2007).
24. Zhang, X. Y. *et al.* Synthesis and piezoresponse of highly ordered Pb(Zr_{0.53}Ti_{0.47})O₃ nanowire arrays. *Appl. Phys. Lett.* **85**, 4190–4192 (2004).
25. Urban, J. J., Yun, W. S., Gu, Q. & Park, H. Synthesis of Single-Crystalline Perovskite Nanorods Composed of Barium Titanate and Strontium Titanate. *J. Am. Chem. Soc.* **124**, 1186–1187 (2002).
26. Li, B., Wang, C., Liu, W., Ye, M. & Wang, N. Multiferroic properties of La and Mn co-doped BiFeO₃ nanofibers by sol–gel and electrospinning technique. *Mater. Lett.* **90**, 45–48 (2013).
27. Huang, Z.-M., Zhang, Y.-Z., Kotaki, M. & Ramakrishna, S. A review on polymer nanofibers by electrospinning and their applications in nanocomposites. *Compos. Sci. Technol.* **63**, 2223–2253 (2003).
28. Ahadi, K., Mahdavi, S. M., Nemati, A. & Kianinia, M. Photoconductivity and diode effect in Bi rich multiferroic BiFeO₃ thin films grown by pulsed-laser deposition. *J. Mater. Sci. Mater. Electron.* **22**, 815–820 (2011).
29. Wu, J., Kang, G., Liu, H. & Wang, J. Ferromagnetic, ferroelectric, and fatigue behavior of (111)-oriented BiFeO₃/(Bi_{1/2}Na_{1/2})TiO₃ lead-free bilayered thin films. *Appl. Phys. Lett.* **94**, 172906 (2009).
30. Kumar, M. M., Palkar, V. R., Srinivas, K. & Suryanarayana, S. V. Ferroelectricity in a pure BiFeO₃ ceramic. *Appl. Phys. Lett.* **76**, 2764–2766 (2000).
31. Zhu, X. H. *et al.* Thickness-dependent structural and electrical properties of multiferroic Mn-doped BiFeO₃ thin films grown epitaxially by pulsed laser deposition. *Appl. Phys. Lett.* **93**, 082902 (2008).
32. Wang, Y. A large polarization in Ce-modified bismuth ferrite thin films. *J. Appl. Phys.* **109**, 124105 (2011).
33. Wang, Y. & Nan, C.-W. Enhanced ferroelectricity in Ti-doped multiferroic BiFeO₃ thin films. *Appl. Phys. Lett.* **89**, 052903 (2006).
34. Lee, Y.-H., Wu, J.-M. & Lai, C.-H. Influence of La doping in multiferroic properties of BiFeO₃ thin films. *Appl. Phys. Lett.* **88**, 042903 (2006).
35. Wu, J., Zhang, B. & Wang, X. Bismuth ferrite composite thin films. *Appl. Phys. A* **111**, 1017–1020 (2013).
36. Matsuo, H. *et al.* Structural and piezoelectric properties of high-density (Bi_{0.5}K_{0.5})TiO₃–BiFeO₃ ceramics. *J. Appl. Phys.* **108**, 104103 (2010).
37. Wu, J. & Wang, J. Multiferroic behavior and impedance spectroscopy of bilayered BiFeO₃/CoFe₂O₄ thin films. *J. Appl. Phys.* **105**, 124107 (2009).
38. Wu, J., Kang, G. & Wang, J. Electrical behavior and oxygen vacancies in BiFeO₃/[(Bi_{1/2}Na_{1/2})_{0.94}Ba_{0.06}]TiO₃ thin film. *Appl. Phys. Lett.* **95**, 192901 (2009).
39. Yang, P. *et al.* Effect of BaTiO₃ buffer layer on multiferroic properties of BiFeO₃ thin films. *J. Appl. Phys.* **105**, 061618 (2009).
40. Chen, P. *et al.* Size-Dependent Infrared Phonon Modes and Ferroelectric Phase Transition in BiFeO₃ Nanoparticles. *Nano Lett.* **10**, 4526–4532 (2010).

41. Basu, S. R. *et al.* Photoconductivity in BiFeO₃ thin films. *Appl. Phys. Lett.* **92**, 091905 (2008).
42. Neaton, J. B., Ederer, C., Waghmare, U. V., Spaldin, N. A. & Rabe, K. M. First-principles study of spontaneous polarization in multiferroic BiFeO₃. *Phys. Rev. B* **71**, 014113 (2005).
43. Park, T.-J., Mao, Y. & Wong, S. S. Synthesis and characterization of multiferroic BiFeO₃ nanotubes. *Chem. Commun.* 2708–2709 (2004). doi:10.1039/B409988E
44. Xie, S. H. *et al.* Nanocrystalline multiferroic BiFeO₃ ultrafine fibers by sol-gel based electrospinning. *Appl. Phys. Lett.* **93**, 222904–222904–3 (2008).
45. Das, R., Khan, G. G., Varma, S., Mukherjee, G. D. & Mandal, K. Effect of Quantum Confinement on Optical and Magnetic Properties of Pr–Cr-Codoped Bismuth Ferrite Nanowires. *J. Phys. Chem. C* **117**, 20209–20216 (2013).
46. Yang, C.-H., Kan, D., Takeuchi, I., Nagarajan, V. & Seidel, J. Doping BiFeO₃: approaches and enhanced functionality. *Phys. Chem. Chem. Phys.* **14**, 15953–15962 (2012).
47. Fujino, S. *et al.* Combinatorial discovery of a lead-free morphotropic phase boundary in a thin-film piezoelectric perovskite. *Appl. Phys. Lett.* **92**, 202904 (2008).
48. Cheng, C.-J. *et al.* Structural transitions and complex domain structures across a ferroelectric-to-antiferroelectric phase boundary in epitaxial Sm-doped BiFeO₃ thin films. *Phys. Rev. B* **80**, 014109 (2009).
49. Seidel, J. *et al.* Domain Wall Conductivity in La-Doped BiFeO₃. *Phys. Rev. Lett.* **105**, 197603 (2010).
50. Hiruma, Y., Nagata, H. & Takenaka, T. Thermal depoling process and piezoelectric properties of bismuth sodium titanate ceramics. *J. Appl. Phys.* **105**, 084112 (2009).
51. Abazari, M., Safari, A., Bharadwaja, S. S. N. & Trolrier-McKinstry, S. Dielectric and piezoelectric properties of lead-free (Bi,Na)TiO₃-based thin films. *Appl. Phys. Lett.* **96**, 082903 (2010).
52. Hejazi, M., Jadidian, B. & Safari, A. Lead-free (Bi_{0.5}Na_{0.5})TiO₃-based thin films by the pulsed laser deposition process. *IEEE Trans. Ultrason. Ferroelectr. Freq. Control* **59**, 1855–1863 (2012).
53. Wu, J., Kang, G. & Wang, J. Electrical behavior and oxygen vacancies in BiFeO₃/[(Bi_{1/2}Na_{1/2})_{0.94}Ba_{0.06}]TiO₃ thin film. *Appl. Phys. Lett.* **95**, 192901 (2009).
54. Béa, H. *et al.* Influence of parasitic phases on the properties of BiFeO₃ epitaxial thin films. *Appl. Phys. Lett.* **87**, 072508 (2005).
55. You, L., Chua, N. T., Yao, K., Chen, L. & Wang, J. Influence of oxygen pressure on the ferroelectric properties of epitaxial BiFeO₃ thin films by pulsed laser deposition. *Phys. Rev. B* **80**, 024105 (2009).

4 Characterization and Equipment Tools

4.1 Introduction

To understand the material's electronic properties, certain information is required such as: crystal structure, surface topography, chemical composition, chemical structure, atomic structure, and electronic state. There is no one technique that is able to provide all the necessary information; it will always require several techniques. In order to fully comprehend the behavior, properties, and to solve the particular problems is necessary to examine and analyze the different aspects of materials. This chapter is a summary of the characterization tools used to identify and understand the phase, morphology, and observed electronic behavior in bismuth ferrite thin films and nanofibers. The characterization methods can be grouped as:

- Physical topography: Scanning electron microscope (SEM)
- Chemical composition: Rutherford backscattering spectrometry (RBS)
- Chemical structure: Electron energy loss spectroscopy (EELS)
- Crystal Structure: X-ray diffraction (XRD)
- Electronic properties: Current vs Voltage, Current vs Time, Permittivity vs Frequency, and Dielectric Loss vs Frequency

Most of the surface characterization methods involve bombarding the surface with a form of radiation: electron, ions, neutrons, and collecting the resulted emitted radiation. Surface analysis techniques: XPS, SEM, EELS, TEM, and RBS are carried out in vacuum. The reason is because the probe/detection system such as electrons and ions are

scatter by molecules in the gas phase. Photons as another detection option, can in principle, be used in ambient, but is also possible that gas absorption occurs. The information that can be obtain from this techniques could be very revealing, however the complexity of the materials could make difficult the interpretation and understanding of the data using simple analysis.

In every characterization tool, it is important to understand the capabilities and limitations of the technique being used in regard with the material, processing methods, and require information.

4.2 X-ray diffraction

A regular array of atoms in a crystal lattice interacts elastically with short radiation, and as a consequence a diffraction spectrum in which the incident radiation is scattered is obtained (Figure 4.1). The diffraction angles and the intensities in the diffractions beams are sensitive to the crystal structure of the specimen. The diffraction angles depend on the Bravais point lattice and the unit cell dimensions of the crystal. To determine the angular distribution of the peak intensities in the diffraction spectrum from a regular crystal lattice is defined by the Bragg's equation:

$$n\lambda = 2d \sin \theta \quad (4.1)$$

where n is an integer, λ is the wavelength of the radiation, d is the spacing of the crystal lattice planes responsible for a particular diffracted beam, and θ is the angle that the incident beams makes with the lattice planes assuming that the angle of incidence is equal to the angle of reflection.

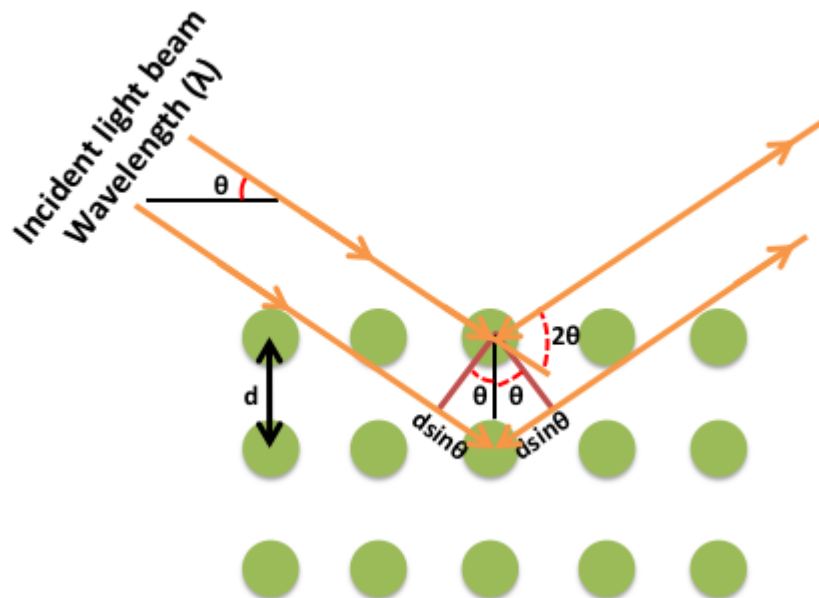


Figure 4.1 Schematic description of Bragg's equation ¹.

X-ray diffraction (XRD) has the capability of measuring the average spacing between the layers and rows of atoms, determining the orientation of a single crystal or polycrystalline sample, measuring the grain size, and internal stresses of small crystalline regions.

An X-ray diffractometer includes five major components: X-rays, the X-ray generator, a diffractometer assembly, X-ray data collection, and analysis system as shown in Figure 4.2. The alignment of the beam, the position and orientation of both the specimen and X-ray detector is controlled by the diffractometer assembly. The X-rays are generated by accelerated beam of electrons on to a pure metal (usually Mo or Cu) target contained in a vacuum tube. These high energy electrons are ejected from the ground state of the metal, creating holes and X-rays are emitted during the re-filling to the ground states.

The resulted diffraction pattern spectrum can be analyzed in two different manners.

- 1) The crystalline material may be identified by comparing the diffraction angles corresponding to the peaks with a diffraction standard.
- 2) The crystalline material may be compared with a calculated spectrum derived from hypothetical model. In a general case, a measured spectrum is compared with existing data.

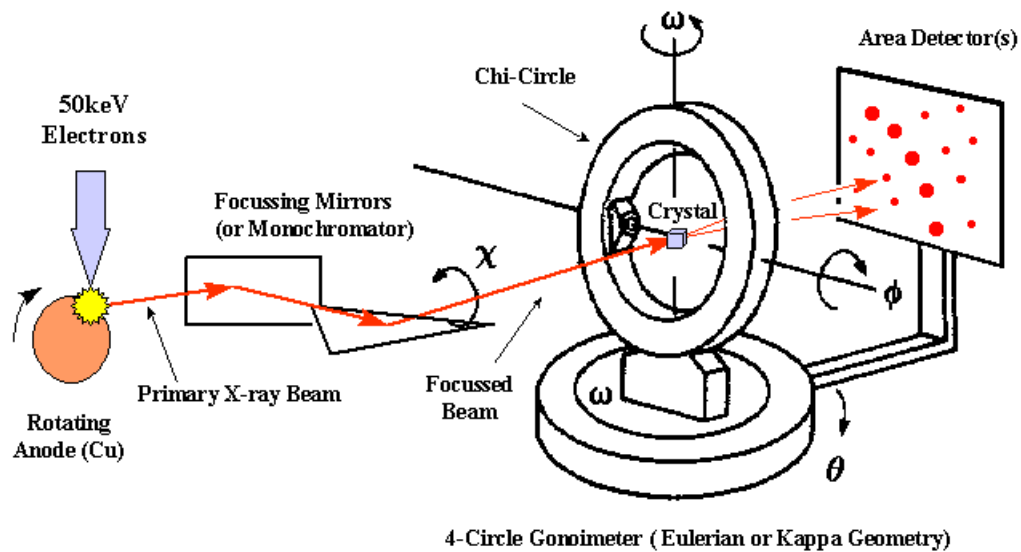


Figure 4.2 Schematic of an X-ray diffraction setup.

Image source: <http://ruppweb.dyndns.org/>

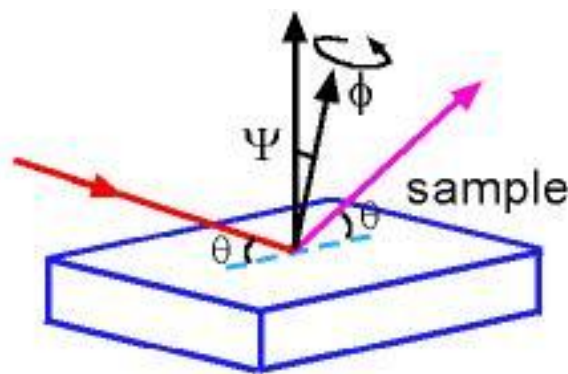


Figure 4.3 X-ray diffraction angles for a thin film deposited on a substrate.

The conventional 2θ X-ray diffraction geometry is not useful for the study and analysis of thin films partially because of the poor sensitivity and the presence of the interfering substrate. A phi scan (ϕ) allows to obtain crystallographic information about thin film as well of specific orientation. In a polycrystalline sample all the grains are randomly oriented, thus all the inclination and rotation angles (Figure 4.3) for a certain plane will result in constant intensity. Differently, for an oriented film in a specific plane, a diffraction peak will be observed for specific rotation and inclination angles depending on the material's structure. In order to examine and oriented film a phi scan/rocking curve experiment is performed. In a rocking curve spectrum the detector is set at specific Bragg angle and the sample is tilted. The crystal/sample will produce a sharp peak, only when is properly tilted so that the crystallographic direction is parallel to the diffraction vector.

4.3 Rutherford backscattering ²

Rutherford Backscattering Spectrometry (RBS) is commonly used to estimate the chemical composition of thin films. RBS provide information such as elemental analysis, thickness, and depth distribution. One of the major advantages of RBS technique is that standard sample is not required to determine the composition of the sample quantitatively. The thickness of the sample is determined by comparing a RBS spectrum with a profile simulated by the SIMNRA software.

The principal of RBS involves mono-energetic He ions between 2 – 4 MeV. These ions impinge perpendicularly on the sample and small portion of the ions will undergo head on collisions with the nucleus of the sample atom on the surface as well as in depth

and backscattered. The particles that are backscattered by angles greater than 90° can be detected and energy-analyzed^{2,3} as shown in Figure 4.4. The backscattered energy from atom with mass M is related to the incident energy through the Kinematic Factor (K) which is expressed in the Equation 4.2, where Q and $\frac{dq}{d\Omega}$ are the number of incident particles and the differential scattering cross section respectively. Consequently, it provides the depth profile and the composition of the film. The energy distribution carries information about the mass and depth distribution of atoms when the scattering occurs².

$$Y = N \frac{dq}{d\Omega} \Delta\Omega Q \quad (4.2)$$

The accelerator is the major component in the RBS setup (Figure 4.5). Charge particles are generated and ions are accelerated to the desired energy to several megaelectron volts. Then, the high energy ions pass through a series of devices that focus the beam and filter the energy for a selected species and energy for a given experiment. Then, the beam passes through a magnet, the focused beam is directed onto the sample.

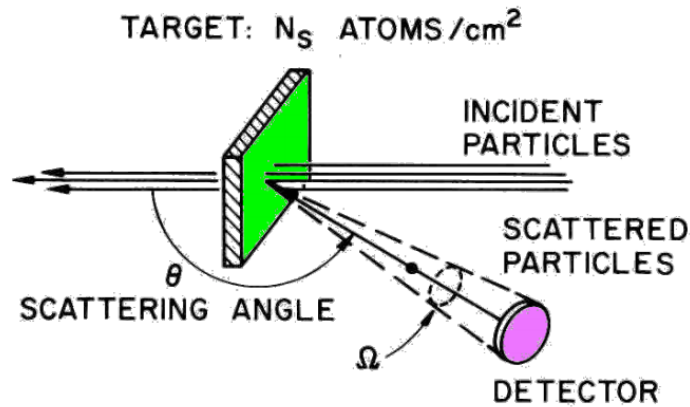


Figure 4.4 Schematic of basic principle of RBS.

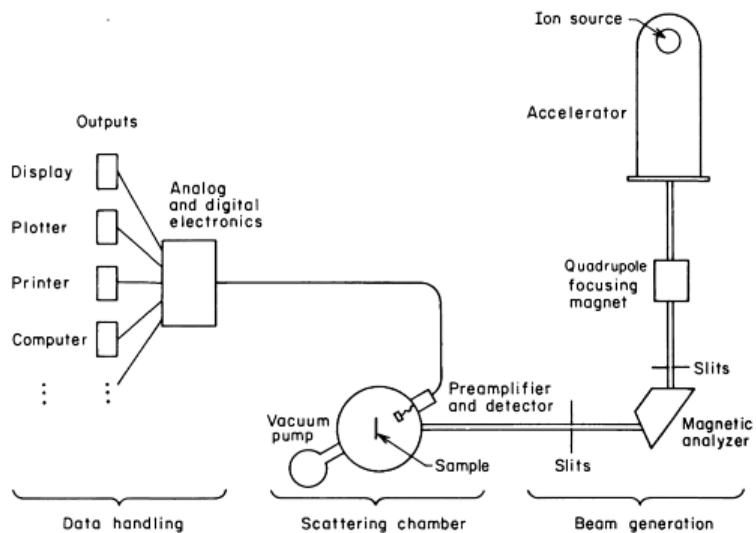


Figure 4.5 Schematic diagram of a typical backscattering spectrometry setup ².

4.4 Raman spectroscopy

Raman spectroscopy is based on inelastic scattering of a monochromatic light and thus maybe compared with Electron Energy Loss Spectroscopy (EELS) discussed in Section 4.8. A specimen is irradiated with a monochromatic source, usually a laser, where photons are absorbed by the sample and then re-emitted. The frequency of the re-emitted photons is shifted up or down in comparison with the frequency of the incident light such effect is referred as Raman Effect. The shifted in frequency provide information about the vibration and rotation modes that are not observed with infrared spectroscopy (IR).

Raman Effect relies upon the polarization of the electron cloud. An incident electromagnetic radiation with frequency, ν_0 , causes a molecular deformation determined

by a molecular polarizability, α . Considering the oscillating wave as an electric field, E , the polarizability relates the dipole moment with the electric field as:

$$P = \alpha E \quad (4.5)$$

As a result of the deformation, molecules start to vibrate with a characteristic frequency, ν_m , such vibration is known as nuclear displacement. The resulted oscillating dipole moments are able to emit light in three different frequencies (Figure 4.9):

1. **Rayleigh scattering**: the excited molecular returns back to the same basic vibrational state and emits light with the same incident frequency, ν_0
2. **Stoke Raman scattering**: A photon with frequency ν_0 , is absorbed by Raman active molecule and part of the photon's energy is transferred to the Raman active mode with frequency ν_m . The resulting frequency of scattered light is reduced to $\nu_0 - \nu_m$.
3. **Anti-Stokes Raman scattering**: A photon with frequency ν_0 is absorbed by Raman active molecule and at the time of interaction is already in the excited vibrational state. The excessive energy of excited Raman active mode is released and the molecule returns to the ground vibrational state. The resulting frequency of scattered light increases up to $\nu_0 + \nu_m$.

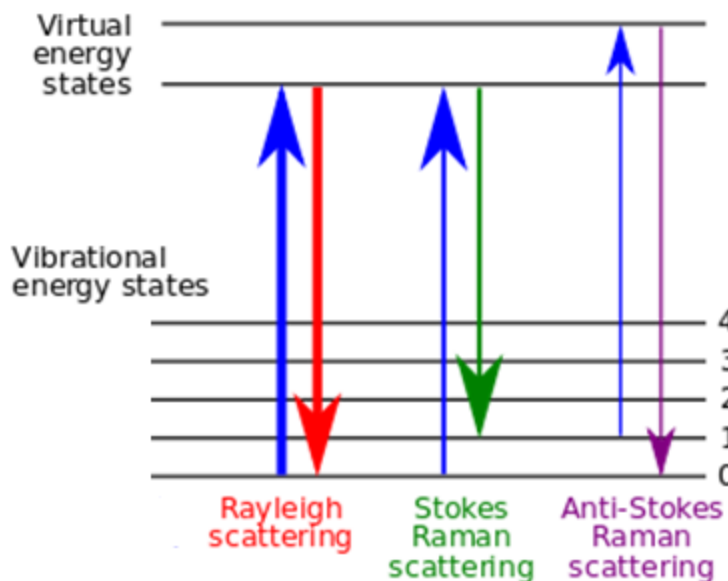


Figure 4.6 Description of the vibrational Raman Effect based upon an energy level approach ⁴⁻⁶.

A Raman system consists of four major components: excitation source (Laser), sample illumination system and light collection optics, wavelength selector, and detector. There are two types of Raman spectrometer systems: a Macro Raman Spectrometer, and Micro Raman Spectrometer (Figure 4.10). The former has spatial resolution anywhere from 100 μm to one millimeter while the latest uses a microscope to magnify its spatial resolution.

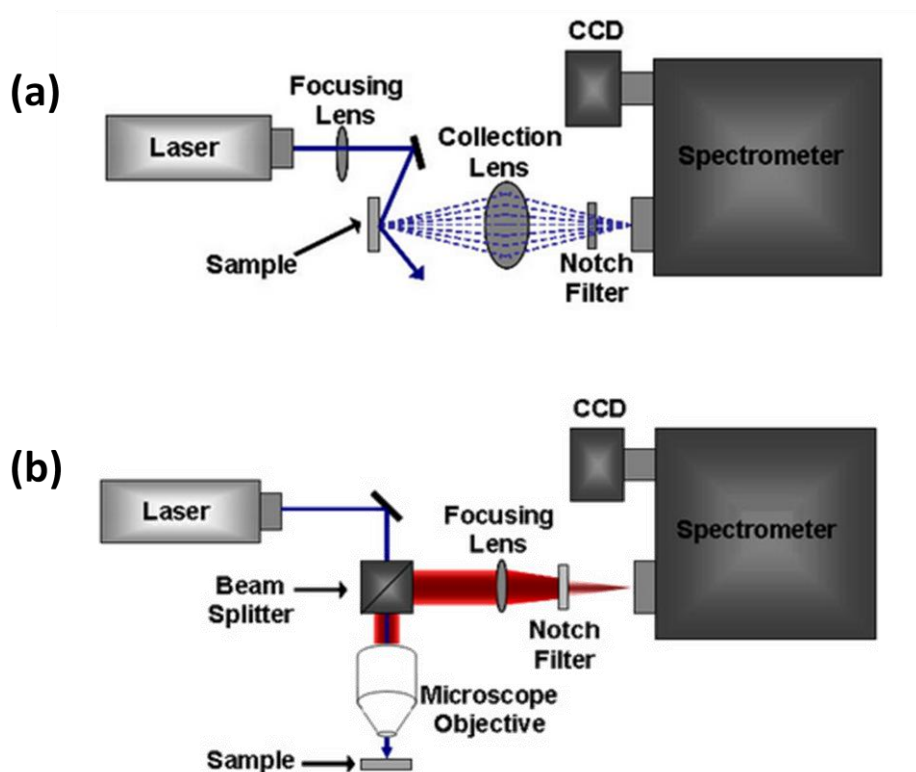


Figure 4.7 (a) Schematic of macro Raman Spectrometer, and (b) schematic of micro Raman Spectrometer ⁷.

Considering that Raman signal is normally weak, there are several techniques to improve Raman signal such as: Stimulated Raman, Coherent Anti-Stokes Raman Spectroscopy (CARS), Resonance Raman (RR), and Surface Enhanced Raman Spectroscopy (SERS). In the Stimulated Raman, the sample is irradiate with a very strong laser pulse and a new “non linear” phenomena is observed in the Raman signal. CARS is another type of “non-linear” spectroscopy in which a strong collinear lasers is used to irradiated the sample. With CARS only one strong Raman peak of interest is obtained. In RR technique it was found that under certain conditions some type of colored molecules can produce Raman scattering instead of fluorescence. The RR takes place when the excitation laser frequency is chosen in a way that it crosses frequencies of electronic

excited states and resonates with them. SERS is an enhancement of polarizability because charges transfer effect or chemical bond formation between the metal surface and the molecules under study.

Advantages of Raman Spectroscopy include ease of sample preparation, is a non destructive technique, and it can be perform using with any operating range from UV to NIR. Vibrational spectra are typically as frequency spectra as a function of intensity.

4.5 Electron microscopy: transmission electron microscopy and scanning electron microscopy^{8,9}

Electron microscope uses accelerated electron as the illumination source and as a result has a higher resolution power that reveal the features of smaller object. Different than usual optical microscope, electron microscope is upside down. In the TEM the source of electrons is at the top of the microscope or the “column” while the collecting system is in the bottom. The main components in the microscope are (Figure 4.11):

- electron gun maintained at high voltage (100 - 400 kV)
- heated tungsten filament capable of generating electron beam current in the order of $5 \times 10^4 \text{ A.m}^{-2}$
- electromagnetic condenser lens system that focuses the high energy electron beam
- specimen stage which allows for tilting as well as some z-adjustment
- objective lenses allows the fine focusing of the image
- final imaging system which also uses electromagnetic lenses
- fluorescence screen where the final image is observed

The scanning electron microscope (SEM) uses a probe lens to focus the beam instead of electromagnetic condenser system. The electromagnetic probe lens in the SEM fulfils a similar purpose to the objective lens in the TEM and determines the ultimate resolution of the specimen. In the SEM, the objective lens is placed above the specimen. When the probe interacts with the sample, inelastic scattering occurs and as a result of such interaction the image is collected. The power of the SEM has to do with the wide range of signals that may result as a consequence of the interaction between the electron probe and the sample surface such as: characteristics X-rays, cathodoluminescent, backscattered electrons, and secondary electron.

The basic difference in the operation between the TEM and SEM lied in the modes of data collection. In the TEM information is collected continuously while in the SEM is collected sequentially for each data point. In the SEM the scanning speed must be restricted in order to ensure that the specimen signal is collected for each point.

Sample preparation for TEM is not simple but techniques are available for doing so such as: mechanical thinning, electrochemical thinning, and ion milling. For SEM imaging, the specimen must be electrically conductive to avoid the accumulation of charge at the surface. In case of insulative sample it must be coated with a metal such as Au or C. TEM is more powerful to study crystallographic defects down to the nanoscale range while SEM is more powerful technique for surface characterization.

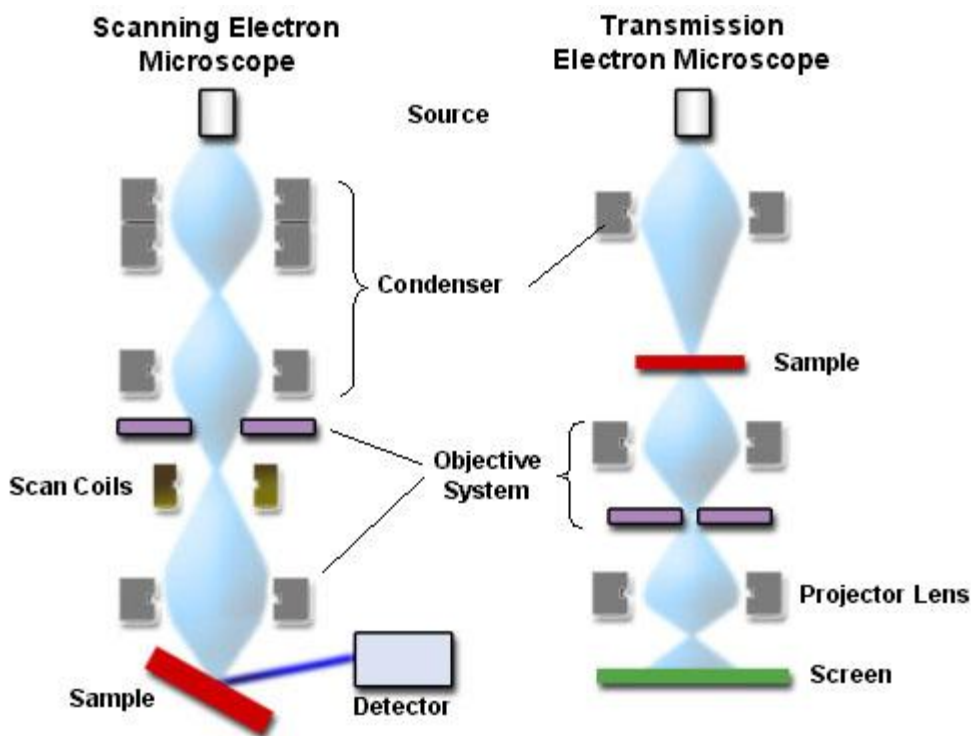


Figure 4.8 Schematic of the scanning electron microscope and transmission electron microscope.

Table 4.1 Comparison between TEM and SEM

TEM	SEM
Primary image is focused by the objective lens, a set of other imaging lenses enlarge the final image.	Image is developed point by point generated by the interaction of focused probe as it scanned across the surface.
Depth of field exceeds the resolution by at least two orders of magnitude	Depth of field is typically of the order of microns, resolution to the nanometer range
Specimen is placed close to the back focal plane of the objective lens	Specimen is placed beneath the probe lens it has a long working distance
Specimen diameter is typically less than 3 mm	Specimen size are similar to those used in optical microscope about 20-30 mm

4.6 Electron energy loss spectroscopy^{4,8,12}

Electron energy loss spectroscopy (EELS) is a technique based on the primary process of an electron excitation, which results in the fast losing energy use to identify the chemical composition. When a specimen is exposed to electrons with known kinetic energy, some of them will undergo inelastic scattering in which they lose energy and their “original” path is deflected. The transmitted beam (Figure 4.15) is collected in a high resolution electron spectrometer in which the electrons are separated according to their kinetic energy and as result the amount of energy that was loss is measured.

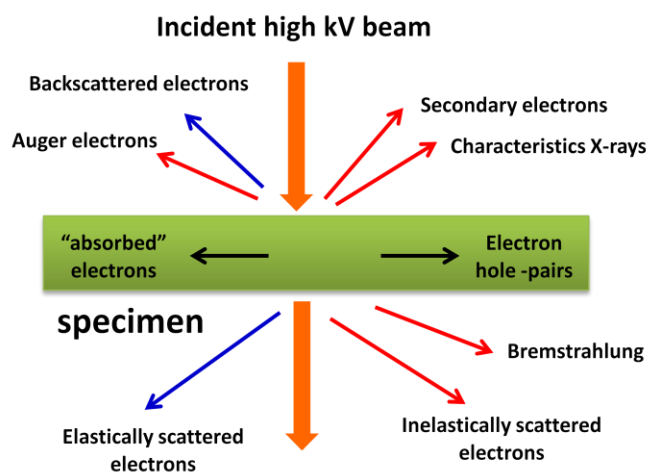


Figure 4.9 Signals and types of scattering¹³.

A spectrum of the number of electrons (scattered intensity) as a function of their decreased kinetic energy is obtained. A typical loss spectrum is shown in Figure 4.16 over a range of 1000 eV. Four processes⁸ may contribute to the energy losses of the electron beam among which two of them can be detected with magnetic spectrometers.

1. **Phonon excitations:** results in small energy losses less than kT , these peaks are within the zero-loss spectrum
2. **Electron transitions:** within and between different shells of the atoms; energy range of 1 – 50 eV; peaks can be detected in the spectrum; used to identify the phase in which a specific element is present
3. **Plasmon excitation:** associated with oscillations in the conduction band; energy range 5 – 50 eV; interpreted in chemical terms; controversial interpretation
4. **Absorption edges associated with atomic ionization:** energy range above 50 eV; accessible for chemical analysis

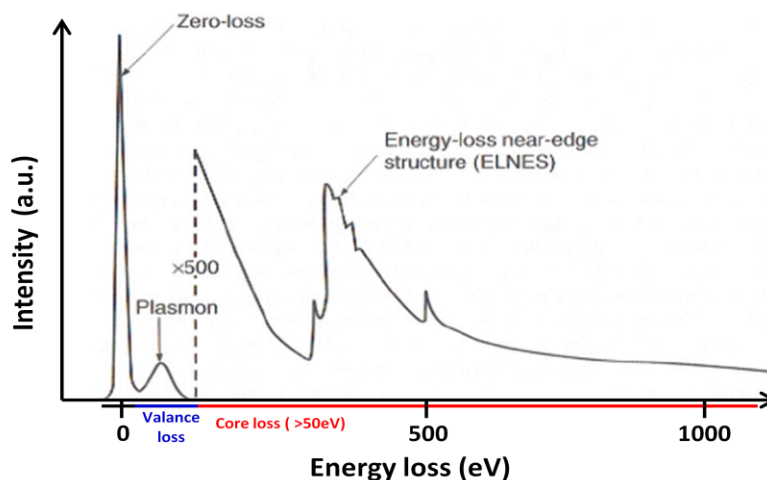


Figure 4.10 An EELS spectrum showing the zero loss peaks and low energy loss region at reduced gain and an excitation absorption edge⁸.

The zero loss peak is characteristic of electrons that are elastically scattered. Low loss peak is related to interaction with electrons weakly bounded to the outer shell. For higher loss there is an interaction with electrons in the inner shell causing excitation from the ground state into an unoccupied shell above the Fermi level.

The energy resolution of the magnetic spectrometers used in EELS is better than 1 eV, and resolutions of the order of 0.5 eV are reported when using a field emission gun. However, in most cases, it is the energy beam spread which limits the EELS resolution, and not the features of the EELS detector. It is recommended to collect the zero loss peak which corresponds to the first Gaussian peak for the beam exiting the specimen and used it to calibrate both the absolute zero for the spectrum and to estimate the energy resolution. The EELS technique is very sensitive and can detect signal from less than a few thousands atoms. The peak intensity depends on the physics of the primary excitation.

In this technique there is no need of a standard sample. The core – loss intensities can be converted to the elemental ratio using cross sections. These cross sections are known for most of the *K* edges and *L* edges. Thus, the simplest method of finding quantitative estimates is by taking the ratios of the data derived from each edge.

4.7 Electrical characterization

In order to measure the electrical properties of bismuth ferrite thin films and nanofibers *Au* electrodes were deposited as top electrode. For BFO based thin films prepared by PLD, *Au* top electrodes of 200 μm in diameter and 50 nm in thickness were deposited by DC sputtering using a metallic shadow mask. For BFO based nanofibers prepared by electrospinning, *Au* top electrodes of 50 nm in thickness and 50 μm in width were deposited by DC sputtering.

4.7.1 Current vs voltage & current vs time (Light On/Light Off)

The *IV* measurements were done using two-probe system and a *HP-Agilent* source meter. Voltage was applied between the two gold electrodes and current passing between them was measured. To study the photoconductive (*It*) response a solar simulator with AM 1.5 spectra output was chosen as the light source. A constant voltage was applied between the two gold electrodes and the variation in the current was measured upon illumination of the nanofibers to the light. While the light source was switched On/Off the current was measured. The On/Off ratio was calculated from the current values with the Light On over the current when Light Off.

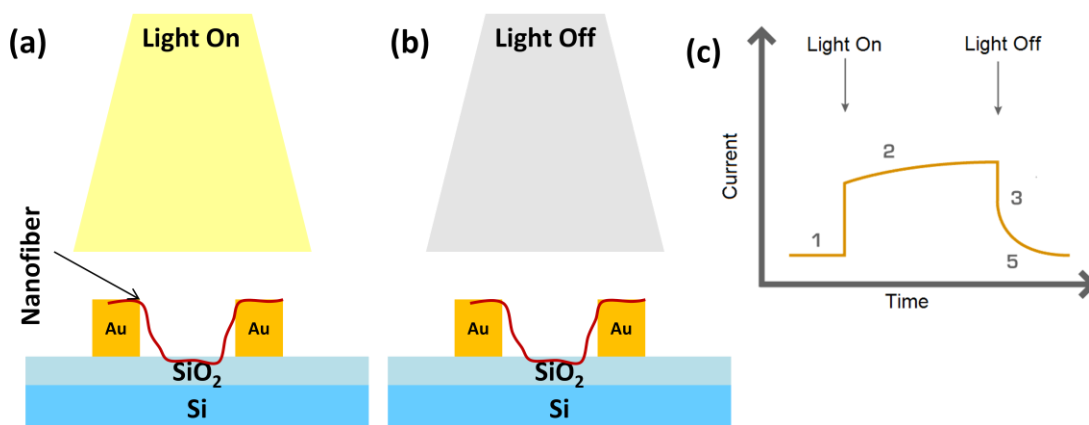


Figure 4.11 The sample is placed under the light source. (a) Light On, (b) Light Off, and (c) Current vs Time plot upon sample illumination.

4.7.2 Ferroelectric and dielectric measurements

The ferroelectric, leakage current (I - V plot), and dielectric properties of thin films were studied using a ferroelectric test system (Precision LC, Radiant Inc.) and LCR meter (HP4284A) at room temperature. The P - E hysteresis loop was measured at a pulse width of 10ms using a triangular wave signal. The dielectric constant and dissipation factor were studied at zero bias fields and an oscillation level of 50mV. Thin films microstructure was studied by a field emission scanning electron microscopy (FESEM-Zeiss, Sigma) operated between 3 to 5 kV.

4.8 Summary

This chapter discussed fundamental principles of characterization techniques used in this investigation to understand the behavior and properties of bismuth ferrite thin films and nanofibers. The crystallographic structure and orientation of grown thin films and nanofibers are studied with phi scan x-ray diffraction and rocking curve. The composition and chemical structure was determined by a combination of techniques which included XPS, RBS, Raman Spectroscopy, and EELS. Finally, the surface topography was studied by electron microscopy such as TEM and SEM.

4.9 References

1. Wide Angle X-ray Diffraction Studies of Liquid Crystals. *OpenStax-CNX* at <<http://cnx.org/content/m46154/latest/?collection=col10699>>
2. Chu, W.-K., James Mayer W. & Nicolet, M. A. *Backscattering Spectrometry*. (Elsevier, 2012).
3. Tu, K. & Rosenberg, R. *Analytical techniques for thin films*. (Academic Press, 1988).
4. Vickerman, J. C. & Gilmore, I. *Surface Analysis: The Principal Techniques*. (Wiley, 2009).
5. Raman spectroscopy. *Wikipedia, the free encyclopedia* (2014). at <http://en.wikipedia.org/w/index.php?title=Raman_spectroscopy&oldid=613655348>
6. Kalantri, P. P., Somani, R. R. & Dinesh T. Makhija. Raman Spectroscopy: A potential technique in analysis of pharmaceuticals. *Chem. Sin.* **1**, 1–12 (2010).
7. Surface-Enhanced Raman Spectroscopy for the Study of Surface Chemistry. *OpenStax-CNX* at <<http://cnx.org/content/m34522/latest/?collection=col10699>>
8. Brandon, D. & Kaplan, W. D. *Microstructural Characterization of Materials*. (John Wiley & Sons, 2008).
9. Reimer, L. *Scanning Electron Microscopy: Physics of Image Formation and Microanalysis*. (Springer, 1998).
10. Atomic force microscopy. *Wikipedia, the free encyclopedia* (2014). at <http://en.wikipedia.org/w/index.php?title=Atomic_force_microscopy&oldid=611644876>
11. Haugstad, G. *Atomic Force Microscopy: Understanding Basic Modes and Advanced Applications*. (John Wiley & Sons, 2012).
12. Egerton, R. *Electron Energy-Loss Spectroscopy in the Electron Microscope*. (Springer, 2011).
13. Williams, D. B. & Carter, C. B. *Transmission Electron Microscopy: A Textbook for Materials Science*. (Springer, 2009).

5 Bismuth Ferrite Thin Film by Sol-Gel

5.1 Introduction

As discussed in Chapter 3 bismuth ferrite has attracted a great deal of attention due to its multiferroic properties at room temperature and as a potential candidate for photovoltaics. In spite of its good ferroelectric properties with high remnant polarization, there are still some arguments on such characteristics. Therefore, further studies are being conducted to elucidate the ferroelectric origin and properties. One of the serious issues in BFO is its high leakage current at room temperature in both ceramic and thin films. As a result, breakdown occurs even at low electric field thereby creating a problem in the observation of saturation in the ferroelectric hysteresis loop (domain switching). A great effort is being done to overcome leakage current issue which has been discussed previously.

In order to understand and correlate bismuth ferrite system/properties from different perspective, thin films have been fabricated through a variety of methods which involve: pulsed laser deposition ¹⁻³, metal organic chemical vapor deposition, physical vapor deposition, chemical solution deposition ⁴⁻⁶, and molecular beam epitaxy ⁷. Among all techniques, chemical solution deposition (CSD) is attractive because of it's a versatility to prepare oxide thin films. It is expected to provide high homogeneity, low temperature, and control of chemical composition. Bismuth ferrite thin films have been prepared by CSD process using different combinations of solvents such as ethylene glycol, acetic acid, 2-methoxyethanol, and propionic acid. Each combination requires complex solution synthesis methods to effectively adjust the viscosity, solubility and surface

tension in the precursor which will later affect the thin film deposition. On the other hand, substitution of various ions in the *Fe* site has been examined with the purpose of improving the insulating resistance. It is reported that Mn-doped ABO_3 perovskite ferroelectric thin films have shown enhanced leakage current and reduced dielectric loss⁸⁻¹³. Substitution of Mn in the Fe site of BiFeO_3 plays an important role in controlling the valence fluctuation of Fe and reducing the carrier concentration in the film¹⁴. Donor doping with Mn is expected to fill the oxygen vacancies and thus increase the electrical resistivity of BFO.

In this chapter, an attempt has been made to prepare BFO- Mn doped thin films by sol-gel method and evaluated its microstructure and leakage current. The thin films crystallinity, and phase are discussed in relation with the leakage current density.

5.2 Experimental procedure

Bismuth ferrite-based ($\text{BiFe}_{1-x}\text{Mn}_x\text{O}_3$; $x = 0, 0.05, 0.10, 0.15$) thin films were prepared by chemical solution deposition (CSD) spin coating method. Precursor solution was prepared by dissolving equal amounts (0.5g) of $\text{Bi}(\text{NO}_3)_3 \cdot 5\text{H}_2\text{O}$, $\text{Fe}(\text{NO}_3)_3 \cdot 9\text{H}_2\text{O}$, and $\text{Mn}(\text{NO}_3)_2 \cdot 4\text{H}_2\text{O}$ in a combination of 2-methoxyethanol (2MEO) and glacial acetic acid (GAC) in a 2:1 ratio. The combination of 2MEO and GAC was selected as a solvent because of its ability to dissolve a wide range of precursor and to adjust the viscosity and surface tension. Individual solutions were kept under stirring for one hour, after dissolution they were added according to stoichiometric composition. Final molarity was adjusted by adding 2MOE. In order to minimize particulate contamination, the solution was filtered. The filtered solution was spin coated at 3000 rpm for 30 seconds to deposit

one layer of thin film on a commercial Pt/Ti/SiO₂/Si substrate. Each layer was pyrolyzed at 300 °C for 2 minutes in a hot plate. The spin coating and pyrolysis processes were repeated several times to increase the film thickness. Finally, the film was placed in the furnace at 550 °C for 10 minutes and cooled rapidly. The described process is summarized in Figure 5.1.

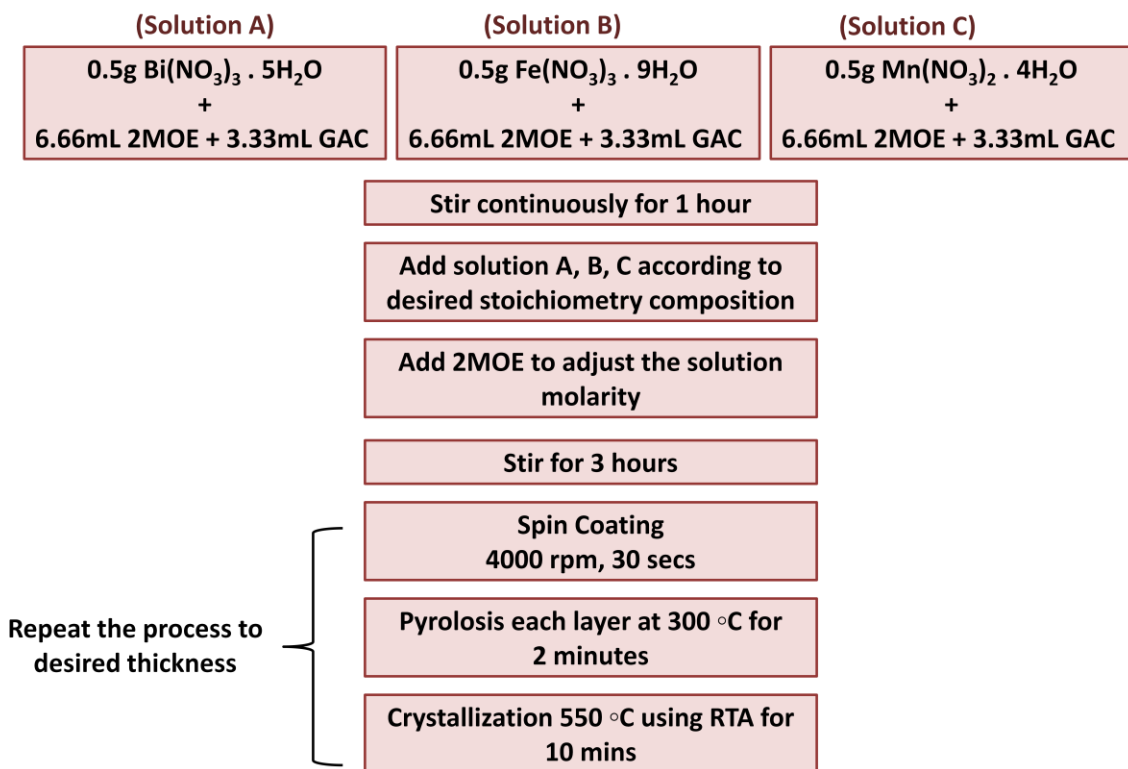


Figure 5.1 Flowchart of sol-gel deposition procedure.

5.3 Results and discussion

Figure 5.2 shows the XRD patterns for $\text{BiFe}_{1-x}\text{Mn}_x\text{O}_3$ ($x=0.00, 0.05, 0.10, 0.15$) films. The XRD indicate that pure polycrystalline BFO films formed with no secondary phase up to 15% Mn doping. Mn atoms has a similar ionic radii to Fe (0.675 \AA), thus the substitution tolerance of Mn in BFO is high and formation of secondary phase was not reported even in 50 % Mn substituted in films ⁹ and ceramics ¹⁰. Figure 5.2c shows the magnified patterns in the vicinity of $2\text{-theta} = 31^\circ$. As shown in the figure, pure BFO exhibits a minor separation between (104) and (110) reflections, which indicates the distorted perovskite rhombohedral structure with $R3c$ space group. When Mn is introduced the peak reflections are shifted and overlapped to a single broad peak ⁹. This results indicated that there is a change in the lattice parameter by Mn substitution and suggest that the rhombohedral structure of un-doped BFO film is modified and reduced towards the tetragonal structure. The (012) peak in Figure 5.2b is observed to be shifted towards a higher angle with Mn doping which is in agreement with a possible change in the lattice parameters as a function of Mn content.

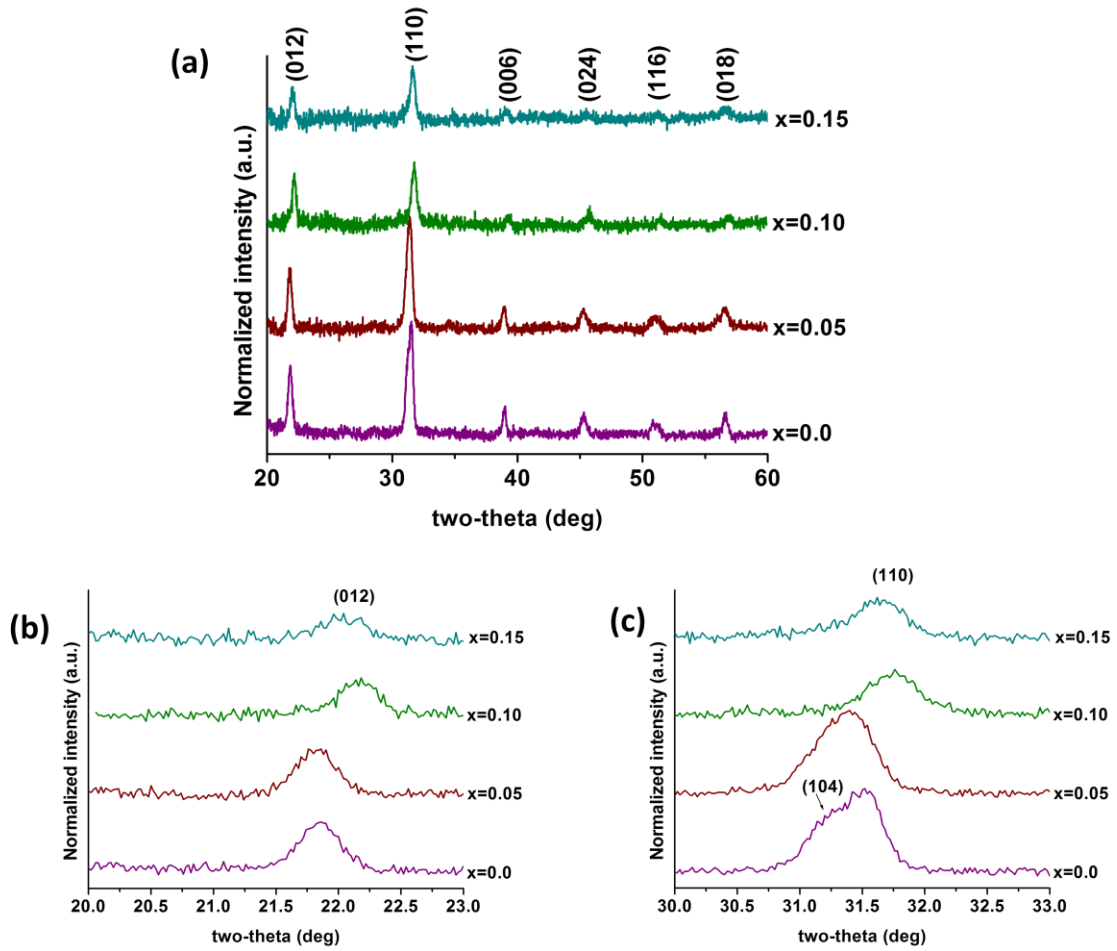


Figure 5.2 X-ray diffraction patterns for BFO-Mn doped thin films.

The effect of Mn doping is further reflected in the Raman spectra of the $x = 0.00$ to 0.15 samples as shown in Figure 5.3. Raman spectroscopy in the microscopic scale is able to probe local changes in the structure¹⁵. The rhombohedral ($R3c$) structure of BFO give rises to 13 Raman actives modes listed as $4A_1 + 9E$ ^{16,17}. In this study 12 and 10 Raman actives modes were identified for un-doped and 5% Mn doped thin films respectively. It is clear from Figure 5.3 that increasing Mn $> 5\%$ content gives rise to broad and less intense Raman bands associated with the normal modes in pure BFO. There is no appearance of extra bands in the doped samples, thus it appears that doping

with Mn in BFO affects the perovskite related phonon modes which are associated with a tilting of the FeO_6 . The increase in wave numbers for some of the higher Raman modes can perhaps be attributed to an increase in the Mn-O bonding compared to Fe-bonding¹⁵. The obtained peak position in this study and the comparison with reported values for BFO single crystal and epitaxial thin film is shown in Table 5.1.

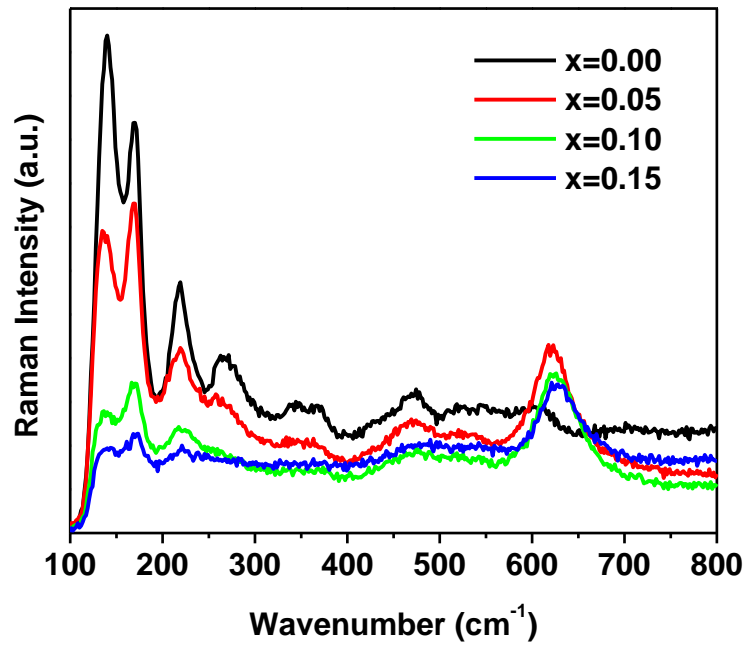


Figure 5.3 Raman Spectroscopy for $\text{BiFe}_{1-x}\text{Mn}_x\text{O}_3$ thin films as function of Mn content.

Table 5.1 Comparison of the Raman mode peak positions from the present study and the literature

Raman mode (cm⁻¹)	Present Study x = 0.00	Present Study x = 0.05	Single Crystal ¹⁶	Epitaxial thin film ¹⁸
A₁-1	140	135	147	136
A₁-2	170	170	176	168
A₁-3	219	219	227	211
A₁-4	498	–	490	425
E	262	258	265	275
E	271	341	279	335
E	344	–	351	365
E	369	389	375	–
E	474	474	437	456
E	543	607	473	549
E	599	622	525	597
E	88	90	77	–
E	–	–	36	–

The surface morphology and cross section of the pure BFO and Mn doped thin films were studied using field emission SEM as shown in Figure 5.4. Un-doped BFO thin films exhibited a smooth surface with minor presence of particulates. Individual grains are not distinguished for low Mn content thin films ($x = 0.00$ to $x = 0.10$). The surface of the films becomes rougher and a combination of small and larger grains are observed when the amount of Mn increased to 15 % (Figure 5.4g). The cross section images showed a

dense and continuous thin film through the overall thickness of 200 nm for lower doping level. Mn 15% doped films show a columnar growth.

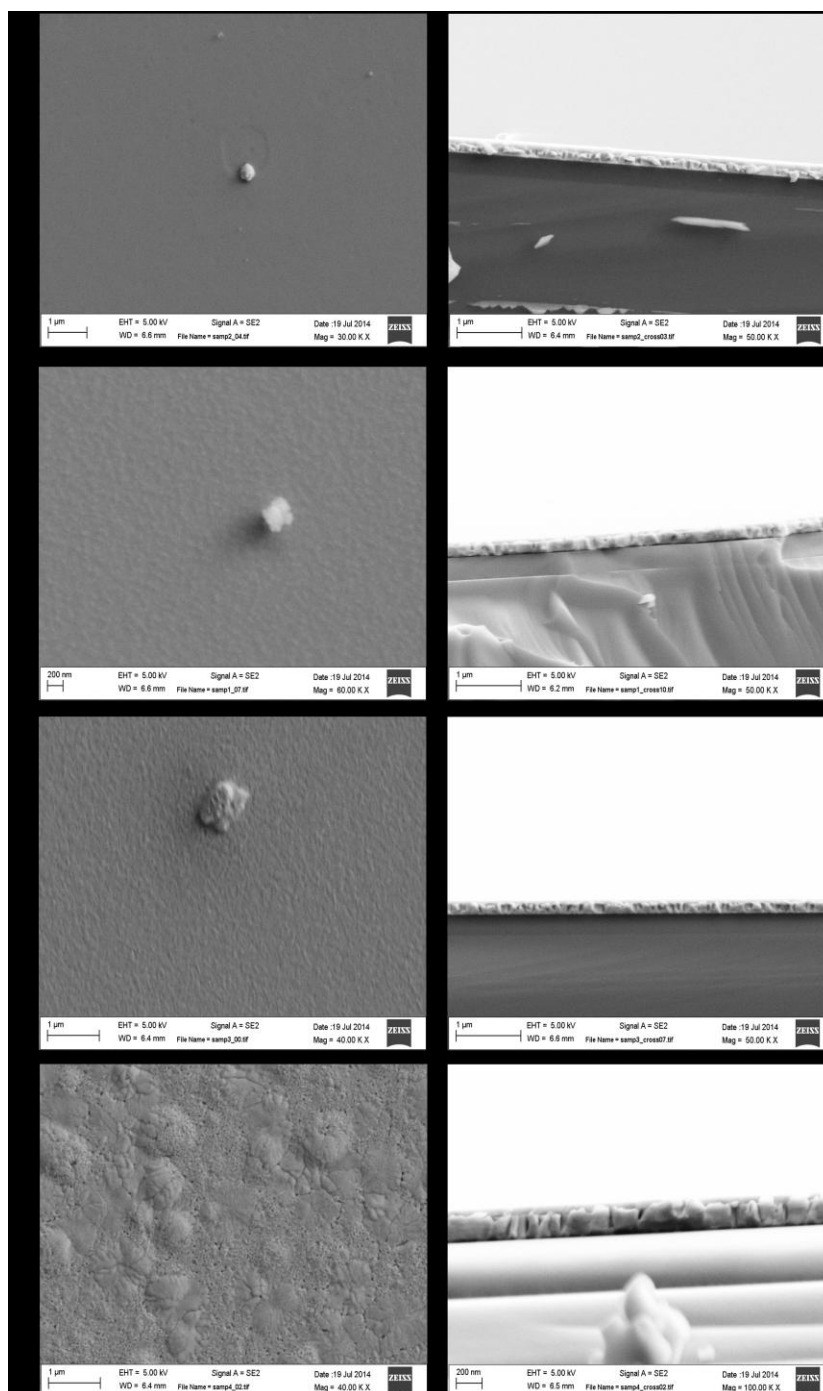


Figure 5.4 FESEM micrographs of $\text{BiFe}_{1-x}\text{Mn}_x\text{O}_3$ thin film surface (left side) and cross section (right side). (a-b) $x = 0.00$, (c-d) $x = 0.05$, (e-f) $x = 0.10$, and (g-h) $x = 0.15$

Figure 5.5 shows the electrical behavior of BFO and BFO-Mn 5% measured at 1 kHz and room temperature. Pure BFO thin films exhibited a poor ferroelectric loop, a so called “banana loop” in which saturation is not observed (Figure 5.5a). In comparison with un-doped BFO films, the hysteresis loop of the Mn 5% films prepared under the same processing conditions show higher remnant polarization. However, saturation still is not achieved and the loop shape is not desirable. The coercive field for 5% Mn-doped thin film is found to be about 300 kV/cm (Figure 5.5b) which is larger than reported value for epitaxial BFO film¹. The leakage current as a function of electric field for un-doped and 5% Mn doping is shown in Figure 5.5c. The leakage current value for un-doped BFO is small at lower voltages and sharply increases at higher voltages. The leakage current for 5% Mn doped films is suppressed by approximately two orders of magnitude and gradually increases with applied voltage. Such a decrease is expected to improve the ferroelectric properties.

As a result of the low electrical resistivity of BFO at room temperature, most of the reported ferroelectric behavior are measured at higher frequencies in the range of 10 to 25 kHz¹. The temperature or frequency dependence of ferroelectric properties suggests that domain wall motion is an important factor in determining the electrical properties of BFO. Despite the fact that leakage current was decreased, the breakdown field of the films, at which the conductivity starts to increase sharply, was low at room temperature. Such value is lower than the reported coercive field of the films^{1,19}, and thus is possible to obtain a saturated polarization hysteresis loop at room temperature. High electric field is necessary to switch the domains which can be achieved at lower temperature without the film breakdown. *H. Amorín et al* described such behavior as dipolar effect in which

Fe^{2+} ions and oxygen vacancies clamps ferroelectric domains²⁰. Considering the multivalence of Mn substitution for Fe, charge compensation can occur by the formation of A-site (Bi) or B-site (Fe) vacancy which is associated with oxygen vacancy. These point defects are mobile and can diffuse to more energetically favorable positions which act as a potential well. Considering same external applied field, the diffusion velocity for ion/cation and oxygen vacancies varies and defects could combine during this process. On the other hand, at low temperature, the potential well intensifies and leads to trapped point defect and the probability of combining decreases. The intensified potential well increases trapped point defect induces and enhances domain pinning. In order to switch the strong pinned domains, high coercive field is necessary. Consequently, at lower temperatures there are more frozen domains and higher remnant polarization could be obtained.

The films doped with $x > 10\%$ exhibited a high leakage current with a rounded hysteresis loop (not shown here).

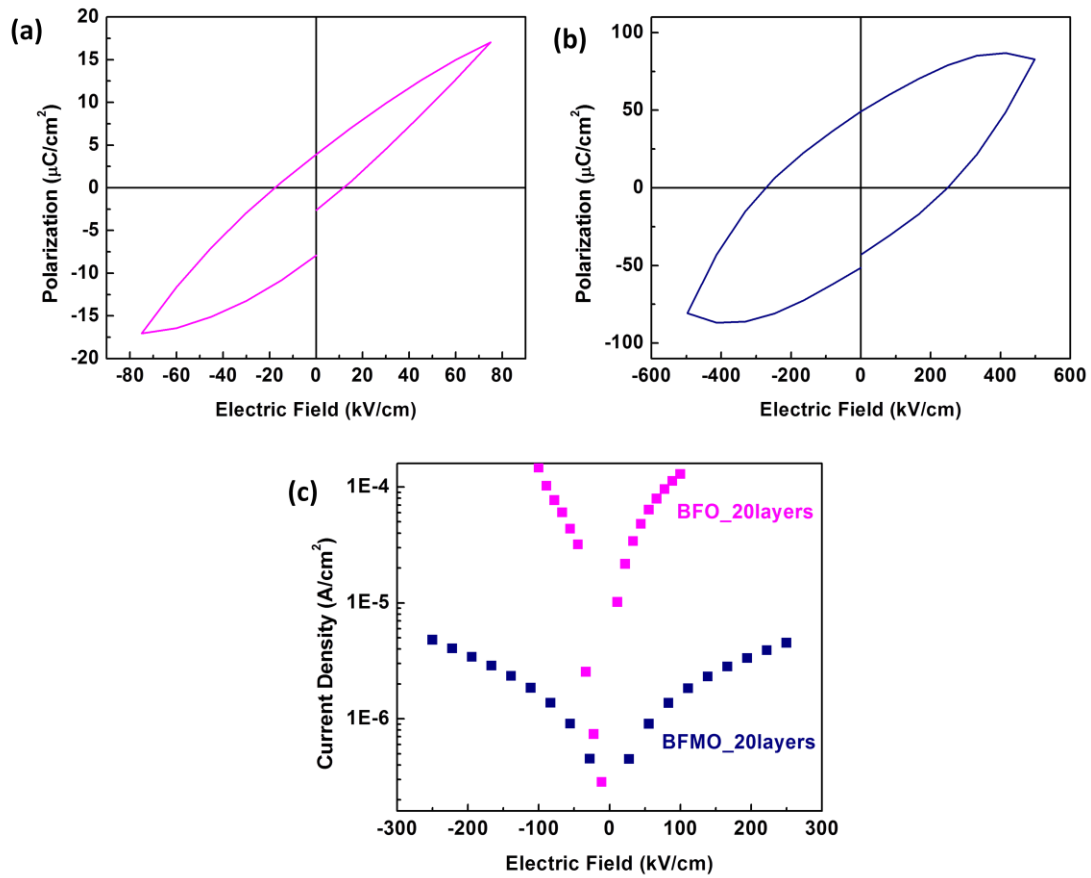


Figure 5.5 (a) Polarization hysteresis loop for BFO thin film, (b) Polarization hysteresis loop for $\text{BiFe}_{0.95}\text{Mn}_{0.05}\text{O}_3$ thin film, and (c) leakage current as a function of electric field for BFO and BFO-Mn thin film **Note: 20 layers is equivalent to an overall thickness of 200 nm.**

5.4 Summary

In this chapter, un-doped and Mn doped ($x = 0.01$ to 0.15) bismuth ferrite thin films of 200 nm in thickness have been fabricated and deposited on Pt/Ti/SiO₂/Si substrate through chemical solution/spin coating process. X-ray diffraction analysis revealed that the obtained films were composed of polycrystalline grains with a perovskite structure. Increasing Mn content resulted in structural change from rhombohedral to tetragonal for $x > 5\%$ which is also confirmed by a peak shift in the Raman phonon active modes. There is no evidence of impurity up to 15% Mn doping. Cross section imaging obtained from FESEM showed the columnar type growth of thin film. The leakage current density of the un-doped films was successfully reduced by two orders of magnitude with 5% Mn doping. However, saturated polarization with electric field is not achieved. The value at which the hysteresis loop started to become rounded (breakdown) is lower than the coercive field of reported BFO. Therefore, a different thin film processing approach is proposed to effectively reduce the leakage current density and coercive field which is discussed in the next chapter.

5.5 References

1. Wang, J. *et al.* Epitaxial BiFeO₃ Multiferroic Thin Film Heterostructures. *Science* **299**, 1719–1722 (2003).
2. Jiang, K. *et al.* Influences of oxygen pressure on optical properties and interband electronic transitions in multiferroic bismuth ferrite nanocrystalline films grown by pulsed laser deposition. *ACS Appl. Mater. Interfaces* **3**, 4844–4852 (2011).
3. Wang, C. *et al.* Leakage current of multiferroic (Bi_{0.6}Tb_{0.3}La_{0.1})FeO₃ thin films grown at various oxygen pressures by pulsed laser deposition and annealing effect. *J. Appl. Phys.* **99**, 054104 (2006).
4. Liu, H. R., Liu, Z. L., Liu, Q. & Yao, K. L. Ferroelectric properties of BiFeO₃ films grown by sol-gel process. *Thin Solid Films* **500**, 105–109 (2006).
5. Shannigrahi, S. R., Huang, A., Chandrasekhar, N., Tripathy, D. & Adeyeye, A. O. Sc modified multiferroic BiFeO₃ thin films prepared through a sol-gel process. *Appl. Phys. Lett.* **90**, 022901 (2007).
6. Fruth, V. *et al.* Preparation of BiFeO₃ films by wet chemical method and their characterization. *J. Eur. Ceram. Soc.* **27**, 937–940 (2007).
7. J. F. Ihlefeld, N. J. P. Optical band gap of BiFeO₃ grown by molecular-beam epitaxy. *Appl. Phys. Lett. - APPL PHYS LETT* **92**, 2908–142908 (2008).
8. Hejazi, M., Taghaddos, E., Gurdal, E., Uchino, K. & Safari, A. High Power Performance of Manganese-Doped BNT-Based Pb-Free Piezoelectric Ceramics. *J. Am. Ceram. Soc.* n/a–n/a (2014). doi:10.1111/jace.13098
9. Singh, S. K., Ishiwara, H. & Maruyama, K. Room temperature ferroelectric properties of Mn-substituted BiFeO₃ thin films deposited on Pt electrodes using chemical solution deposition. *Appl. Phys. Lett.* **88**, 262908 (2006).
10. Palkar, V. R., Kundaliya, D. C. & Malik, S. K. Effect of Mn substitution on magnetoelectric properties of bismuth ferrite system. *J. Appl. Phys.* **93**, 4337–4339 (2003).
11. Li, B., Wang, C., Liu, W., Ye, M. & Wang, N. Multiferroic properties of La and Mn co-doped BiFeO₃ nanofibers by sol-gel and electrospinning technique. *Mater. Lett.* **90**, 45–48 (2013).
12. Singh, S. K., Ishiwara, H., Sato, K. & Maruyama, K. Microstructure and frequency dependent electrical properties of Mn-substituted BiFeO₃ thin films. *J. Appl. Phys.* **102**, 094109 (2007).
13. Yu, X. & An, X. Enhanced magnetic and optical properties of pure and (Mn, Sr) doped BiFeO₃ nanocrystals. *Solid State Commun.* **149**, 711–714 (2009).
14. Yoneda, Y. & Sakamoto, W. Electronic and local structures of BiFeO₃ films. *J. Phys. Condens. Matter* **23**, 015902 (2011).
15. Somdutta Mukherjee, R. G. Influence of Zr doping on the structure and ferroelectric properties of BiFeO₃ thin films. *J. Appl. Phys.* **107**, 123535 – 123535–5 (2010).
16. Fukumura, H. *et al.* Raman scattering study of multiferroic BiFeO₃ single crystal. *J. Magn. Magn. Mater.* **310**, e367–e369 (2007).
17. Palai, R. *et al.* β phase and γ - β metal-insulator transition in multiferroic BiFeO₃. *Phys. Rev. B* **77**, (2008).

18. Singh, M. K., Jang, H. M., Ryu, S. & Jo, M.-H. Polarized Raman scattering of multiferroic BiFeO₃ epitaxial films with rhombohedral R3c symmetry. *Appl. Phys. Lett.* **88**, 042907 (2006).
19. Singh, S. K. & Ishiwara, H. Reduced Leakage Current in BiFeO₃ Thin Films on Si Substrates Formed by a Chemical Solution Method. *Jpn. J. Appl. Phys.* **44**, L734 (2005).
20. Amorín, H. *et al.* Multiferroism and enhancement of material properties across the morphotropic phase boundary of BiFeO₃-PbTiO₃. *J. Appl. Phys.* **115**, 104104 (2014).

6 Bismuth Ferrite Thin Films by Pulsed Laser Deposition

6.1 Introduction

Several deposition techniques such as sol-gel, chemical solution deposition (CSD) ^{1,2}, radio frequency sputtering (RF) ^{3,4}, molecular beam epitaxy (MBE) ^{5,6}, and pulsed laser deposition (PLD) ⁷⁻⁹ have been employed for the deposition of BFO based thin films. Among them PLD is a popular technique due to the capability to deposit complex oxides, which allow the growth of high quality thin films. In the PLD method, presence of oxygen pressure during film growth significantly affects the crystallization, phase purity, and eventually properties of the films. A great deal of research is accomplished in deposited bismuth ferrite thin films with PLD techniques for multiferroic applications

This chapter is focused on the investigation of thin films with following target composition deposited on (001) oriented SrTiO₃ substrate as shown in Figure 6.1:

1. Pure BiFeO₃
2. Solid solution of BiFeO₃-(Bi, K)TiO₃
3. BFO and BNT-BKT-BT targets to develop bi-layered thin films.

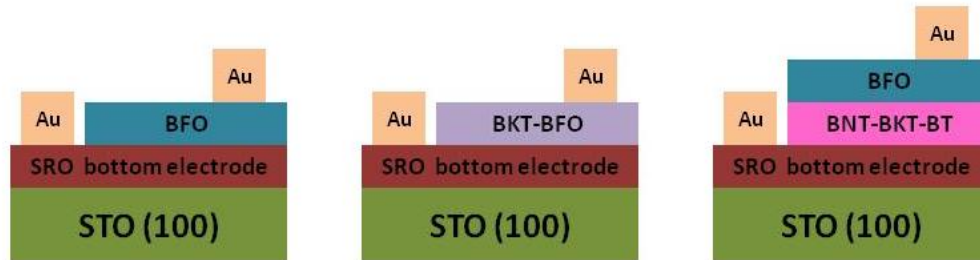


Figure 6.1 Schematic of three different thin film design deposited by PLD.

6.2 Experimental procedure

6.2.1 Powder and target preparation

The preparation of the PLD ceramic target for the fabrication of thin film is similar to the fabrication of bulk ferroelectric ceramic. Mixed-oxide route was employed for powder and ceramic processing. The process was optimized to obtain a high quality target. The characteristics of the target regarding the density, purity and phase uniformity is important for the film quality. The high quality PLD target plays an important role on the preparation, structure, and properties of thin films.

Different BFO based compositions were prepared using Bi_2O_3 (99.9%, Aldrich), Fe_2O_3 (<99%, Alfa Aesar), K_2CO_3 (99.99%, Alfa Aesar), TiO_2 (99.5%, Aldrich), Na_2CO_3 (99.95%, Alfa Aesar) and BaCaO_3 (99.9%, Alfa Aesar) as starting materials. The ceramic target compositions are: (1) BiFeO_3 [BFO], (2) $0.6 \text{ BiFeO}_3\text{-}0.4(\text{Bi}_{0.5}\text{K}_{0.5})\text{TiO}_3$ [BFO-BKT], and (3) $0.88(\text{Bi}_{0.5}\text{Na}_{0.5})\text{TiO}_3\text{-}0.08(\text{Bi}_{0.5}\text{K}_{0.5})\text{TiO}_3\text{-}0.04\text{BaTiO}_3$ [BNT-BKT-BT]. A flow chart for the preparation of BFO-based ceramic target is shown in Figure 6.2. The raw materials were dried overnight at 200 °C to remove moisture, and then manually mixed in proper stoichiometric proportions. The mixture was ball milled in acetone for 24 hours followed by drying and calcination in air. The calcination regimes for BFO, BFO-BKT and BNT-BKT-BT were 750, 870 and 850 °C for 4 hours respectively. The calcined powder was ball milled for 10 hours, dried, and pressed into ceramic pellets of 25 mm in diameter. The BFO, BFO-BKT and BNT-BKT-BT pellets were sintered at 850, 1000 and 1150 °C for 2 hours respectively to obtain dense with relative density > 94%. The sintered density was calculated geometrically. Low density target can either results in

fracture of the target during laser ablation or create large particulate on the surface of thin films.

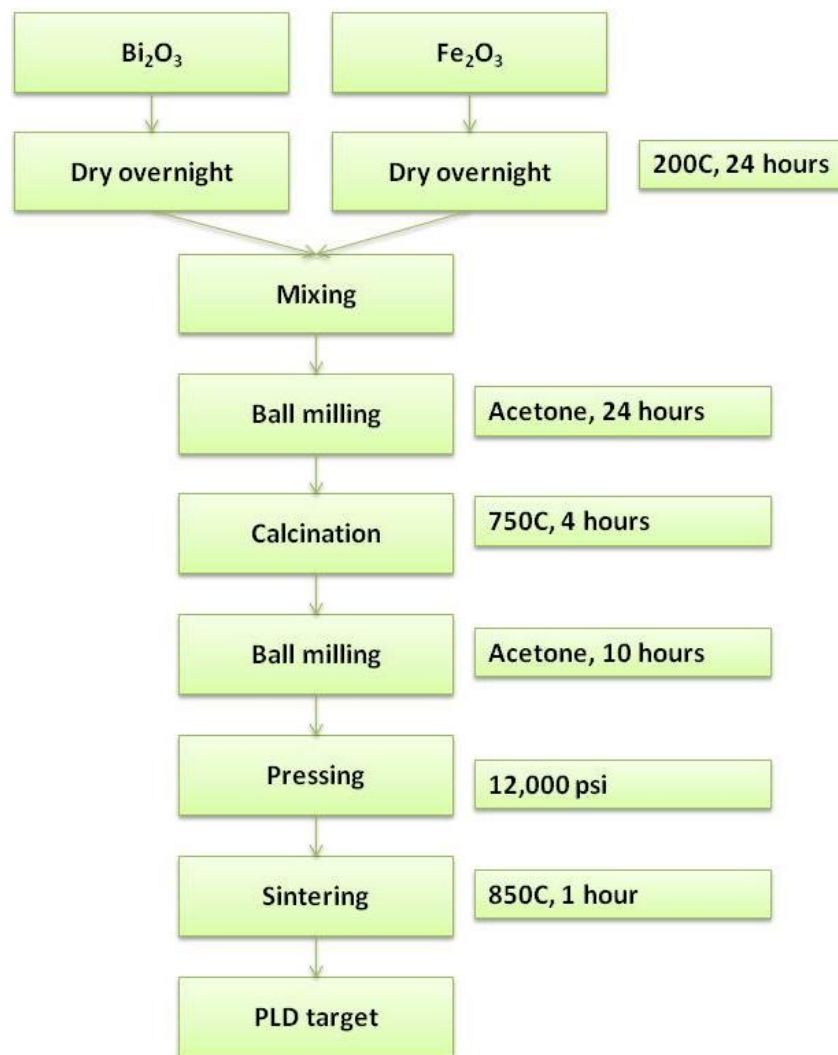


Figure 6.2 Flowchart for the preparation of bismuth ferrite ceramic target by solid oxide method.

Table 6.1 Weight of raw materials for a 100 g batch of BiFeO₃

Composition	BFO
Precursor	Weight (grams)
Bi ₂ O ₃	74.4767
Fe ₂ O ₃	25.5241

Table 6.2 Weight of raw materials for a 100 g batch of
0.6BiFeO₃-0.4(Bi_{0.5}K_{0.5})TiO₃

Composition	BFO-BKT
Precursor	Weight (grams)
Bi ₂ O ₃	67.6145
Fe ₂ O ₃	17.3792
K ₂ CO ₃	5.0138
TiO ₂	11.5890

Table 6.3 Weight of raw materials for a 100 g batch of 0.88(Bi_{0.5}Na_{0.5})TiO₃-
0.08(Bi_{0.5}K_{0.5})TiO₃-0.04BaTiO₃

Composition	BNT-BKT-BT
Precursor	Weight (grams)
Bi ₂ O ₃	52.4149
Na ₂ CO ₃	10.9291
K ₂ CO ₃	1.2956
TiO ₂	37.4327
BaCO ₃	2.5747

6.2.2 Laser deposition system

Pulsed laser deposition technique is based on the interaction of high-powered nanosecond Excimer-laser pulses with bulk targets resulting in evaporation, plasma formation, and subsequent deposition of thin films. A KrF excimer (Lamda Physik) laser was used for depositing BFO-based thin films. The KrF excimer laser had a wavelength of 248 nm and a pulse length ranging of 30 nsec. The laser beam was focused onto the prepared ceramic target, which was at an angle of 45° respect to the beam. The operating frequency was in the range from 5 to 10 Hz. The laser fluency was varied by placing attenuation lenses between the lasers and focusing lenses. The substrate was attached to a substrate heater block with Ag paint. The target to substrate distance was kept at 6.4 cm. Thin film deposition was carried out in oxygen ambient. The chamber was first pump using a turbo pump backed by a roughing pump and the substrate was heated to deposition temperature. The oxygen gas was introduced through a leak valve followed by deposition. A schematic of the PLD system and Standard Operational Procedure is shown.

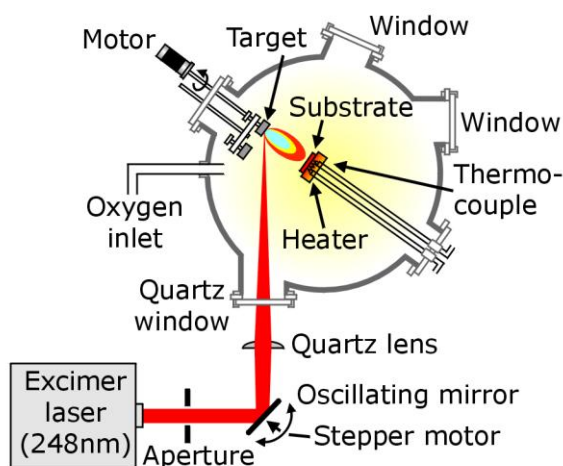


Figure 6.3 Schematic diagram of the deposition system used for laser ablation.

6.2.3 Standard procedure

I. Preparation of the instruments

1. Laser chiller, Laser, and the two mechanical pumps are first turned on and warm up for a few minutes. The mechanical pumps are turn on one at a time to prevent the current overflow and fuse break. The chiller must be keep on when the laser and/or turbo pump are running and the water pressure must not exceed 25 psi.
2. Remove the heater flange by removing the bolts and increasing pressure inside the chamber to push the flange outward.

II. Substrate preparation and installation

3. Clean two small beakers and a pair of tweezers using methanol.
4. Remove the substrates from packaging using Teflon tweezers and put in acetone for 1-2 minutes. Rinse the substrates in acetone and then in methanol.
5. While the substrate is soak in methanol, vent the chamber with oxygen (set pressure at 10 psi) through the backfill valve with the shutter closed on the substrate heater before removing the heater flange from the chamber. Remove the heater and immediately replaced with the blank flange.
6. Rinse the substrate with methanol, then de-ionized water, and finally clean with compressed air/nitrogen.
7. Apply a small drop of silver paint on the heater block and place the substrate carefully on the drop of paint and allow the paint to flow to the edges.
8. To dry the solver paint, turn the heater and increase the temperature to 150^oC which could be part of the heating up program to the final deposition temperature. Place the heater flange back into the chamber.

III. Base Pressure Pump-down

9. Open the right angle valve to pump #2 (roughing pump directly connected to chamber) to begin the pump-down sequence and raise the shutter.
10. Continue to run the heater program to deposition temperature while the roughing pump is evacuating the chamber.
11. At approximately 50 mTorr oxygen is introduced into the system to flush out contaminants. This is repeated several times to ensure a better and faster pump-down.
12. The right angle valve to pump #1 is then opened to rough out the turbo-pump while the heater reaches the desired temperature.
13. Once the pressure on Convectron gauge is below 20 mTorr, start the turbo-pump.
14. Close the right angle valve to pump #2, and open the gate valve to switch to the high vacuum turbo-pump.
15. Allow the system to pump-down for 1.5 hours at minimum, or until the pressure is in the range of 5 to 8×10^{-6} Torr.

IV. Oxygen Pre-anneal

16. Turn the switch on the MKS oxygen controller to AUTO and close the gate valve immediately. Turn on the right angle valve to pump #2 by two turns using the screw on the handle to judge to stabilize at the desired pressure. Shut off the turbo-pump and close the right angle valve to pump # to isolate the turbo. Vent the turbo-pump by attaching the plastic tube to nitrogen cylinder and let the nitrogen into the turbo-pump for 10 seconds.
17. Adjust the pressure on MKS controller to the desired value. Allow the substrate to equilibrate and burn off organic residue for a minimum of 1 hour before film deposition.

V. Film Deposition

18. Turn on the laser to allow the pulse energy to stabilize. Using the laser power meter in front of the beam, measure the power output for a 40 second trend to ensure the stability. Turn off the laser beam.

19. Un-cover the lens assembly, laser port, and close the shutter on the heater flange.

Select the target and start the target rotation.

20. Open the beam stop to begin the film deposition for the predetermined time. Turn on the laser.

21. After deposition for the desired time, stop the laser using first the beam stop and then the keypad to stop the deposition.

22. Close the right angle valve to pump #2, turn the switch on the MKS controller to CLOSE, and stop the target rotation.

VI. Post-deposition anneal

23. Shut off the heater or allow it to continue with the cool down/annealing program.

24. Fill the chamber with 1 atm oxygen at the beginning of the annealing segment.

25. After the annealing procedure the heater automatically switch off and reset.

VII. Cooling and Shut-down

26. Shut down all equipments if not continuing with another film/layer (Convectron and turbo-pump controller) deposition.

6.2.4 Deposition of bottom electrode

A commercial SrRuO_3 (SRO) target with purity 99.9+ % purchased from Super Conductor Materials Inc., Suffern, NY was employed to deposit a bottom electrode on a (001)- SrTiO_3 (STO) substrate. Deposition of the SRO was following the same procedure described in previous section. SRO was deposited at a substrate temperature of 800 °C, 150 mTorr oxygen pressure, 200 mJ laser energy, 5 Hz laser repetition rate, and deposition rate of 40 minutes/100 nm. Following the deposition, the SRO layer was annealed in the PLD chamber at 650 °C for 1 hour under 1 atm oxygen pressure and then cooled to room temperature

6.2.5 Deposition of top electrode

Prior to deposition of top electrodes, the surface of the deposited film was cleaned using nitrogen/air, upon removal of the sample from the PLD chamber. Gold top electrodes were deposited using DC sputtering technique (EMS150T ES) at room temperature. Electrodes were patterned using a shadow mask (Stencils Unlimited Inc., Lake Oswego, OR) with circular patterns of 200 μm diameter mounted on top of the sample. The chamber was first evacuated once the pressure inside the chamber reaches 10^{-5} Torr. Then Argon was allowed to flow in the chamber keeping with the pressure at 5×10^{-5} Torr. The deposition was performed for 5 minutes.

6.3 Bismuth ferrite based thin films

6.3.1 Bismuth ferrite

BFO ceramic target was prepared as previously explained in Section 6.2.1, following by thin film deposition described in Section 6.2.3. Deposition parameters for BFO composition were set as follows: substrate temperature of 750 °C, 150 mJ laser energy, 10 Hz repetition rate, oxygen background pressure of 20 mTorr, and 90 minutes/500 nm.

Figure 6.4a present the surface morphology of BFO thin film sample deposited at mentioned conditions. It is clear that that BFO film consist of block-type hills and porous microstructure. Similar features have been reported for bismuth ferrite thin films deposited at oxygen partial pressure lower than 50 mTorr with similar degree of roughness¹⁰. The BFO surface roughness and the grain size dramatically depend on the oxygen partial pressure^{10,11}, but it could be related to other parameters such as substrate temperature, and deposition rate. It is found that 15% La doping results in improvement of the surface morphology as shown in Figure 6.4b. **Note:** The electrical properties of BFO-La doped thin films showed poor hysteresis loop similar to pure BFO, and this specific composition is not part of this thesis.

XRD in Figure 6.5 revealed the structure and phase of the as grown for pure BFO films. The sample was scanned in the 2theta range of 20 - 60°. Only (100) diffraction peaks corresponding to the BFO perovskite phase were detected for BFO films, indicating the preferred orientation with no trace of impurities phases.

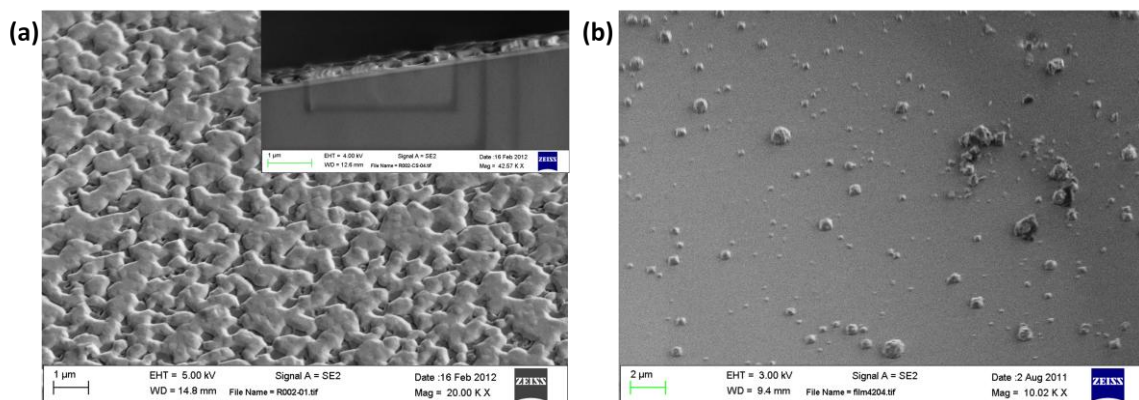


Figure 6.4 FESEM surface image of (a) BFO (inset: BFO cross section), and (b) BFO-La doped thin film.

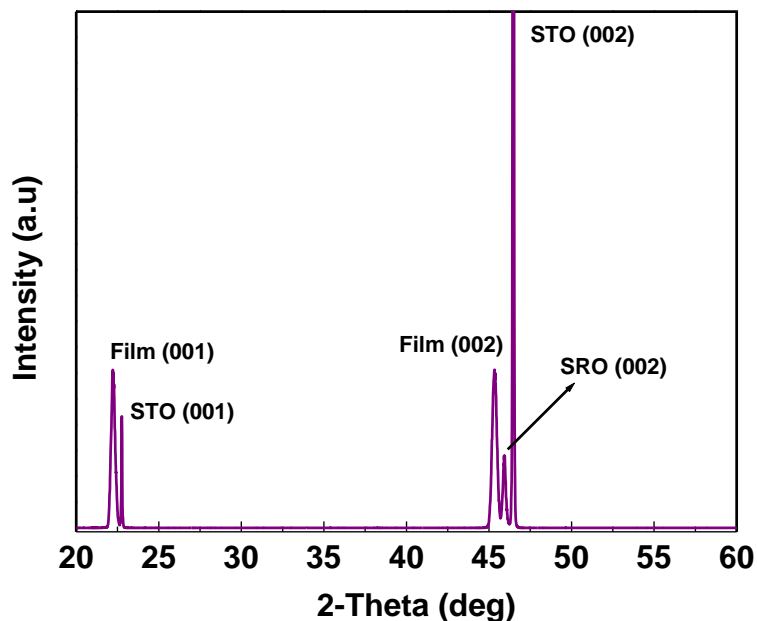


Figure 6.5 X-ray diffraction pattern for pure BFO thin film.

Figure 6.6 shows the polarization-electric field hysteresis loop measured at room temperature and a frequency of 1 kHz. For an electric field of 200 kV/cm the polarization is low compared to reported values by Wang *et al*⁸ and its banana-like shape is indicative of a strongly resistive contribution. Despite that BFO-La doped exhibited higher quality surface morphology compared to un-doped samples (Figure 6.4); similar P-E loop was

observed due to the high leakage current which is the main problem of BFO thin films. The main reason for the leakage current at room temperature has been attributed to oxygen vacancies. Such vacancies could be a result of a charge imbalance in the BFO composition.

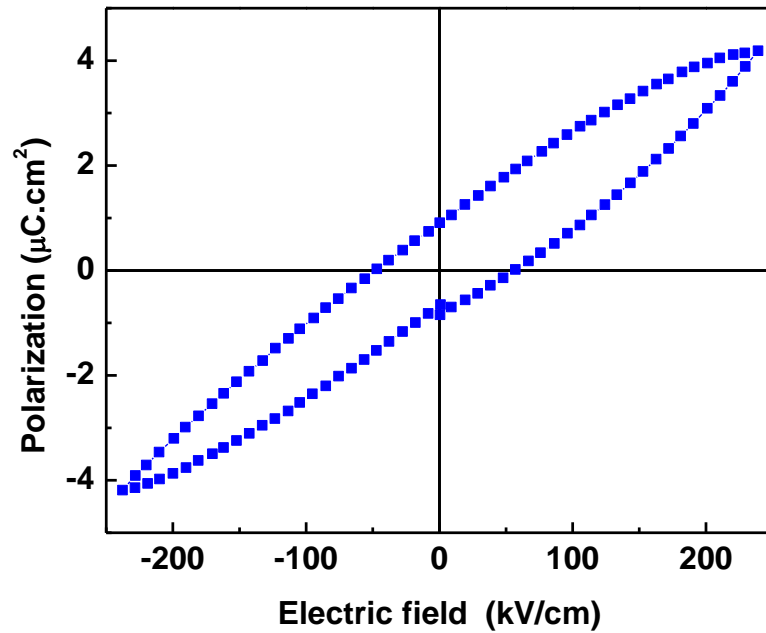


Figure 6.6 Polarization-Electric Field (P-E) hysteresis loop for single layer bismuth ferrite thin film measured at 1 kHz and room temperature.

Therefore, in order to reduce the leakage current and improve the quality of films and ferroelectric behavior two approaches are addressed in the following sections: first, using target with compositions of BFO-BKT, and second, fabrication of bi-layered thin film of BFO/BNT-BKT-BT. Such approaches are expected to suppress the formation of oxygen vacancies and minimize the leakage current.

6.3.2 Effects of oxygen pressure on $0.6\text{BiFeO}_3\text{-}0.4(\text{Bi}_{0.5}\text{K}_{0.5})\text{TiO}_3$ thin films

A BFO-BKT ceramic target was prepared as previously explained in Section 6.2.1, following by thin film deposition described in Section 6.2.3. Deposition parameters for BFO-BKT sample were set as follows: substrate temperature of 800 °C, 170 mJ laser energy, 10 Hz repetition rate, for 90 minutes. The oxygen background pressure for BFO-BKT thin films was varied in a range of 300 to 500 mTorr while other parameters were kept fixed. The ferroelectric, dielectric, and leakage current were characterized as a function of oxygen pressure.

Two-theta XRD spectrum for BFO-BKT thin films grown under different oxygen pressures are shown in Figure 6.7. The XRD patterns show that a single perovskite phase has been formed for sample prepared at all oxygen partial pressure. Peak integration parameters for the $h00$, $h = 2$, and 4 peak profile from 2-theta versus intensity plots shown in Table 6.4 reveals that the (200) peak has shifted toward a lower angle for 300 mTorr. Considering the film thickness of ~ 600 nm, the peak shift can't be related to induce strain by the lattice mismatch between the film and the substrate. At this thickness the film is considered to be strain relieve. Therefore, the peak shift could be related to changes in film compositions which is confirmed by RBS results.

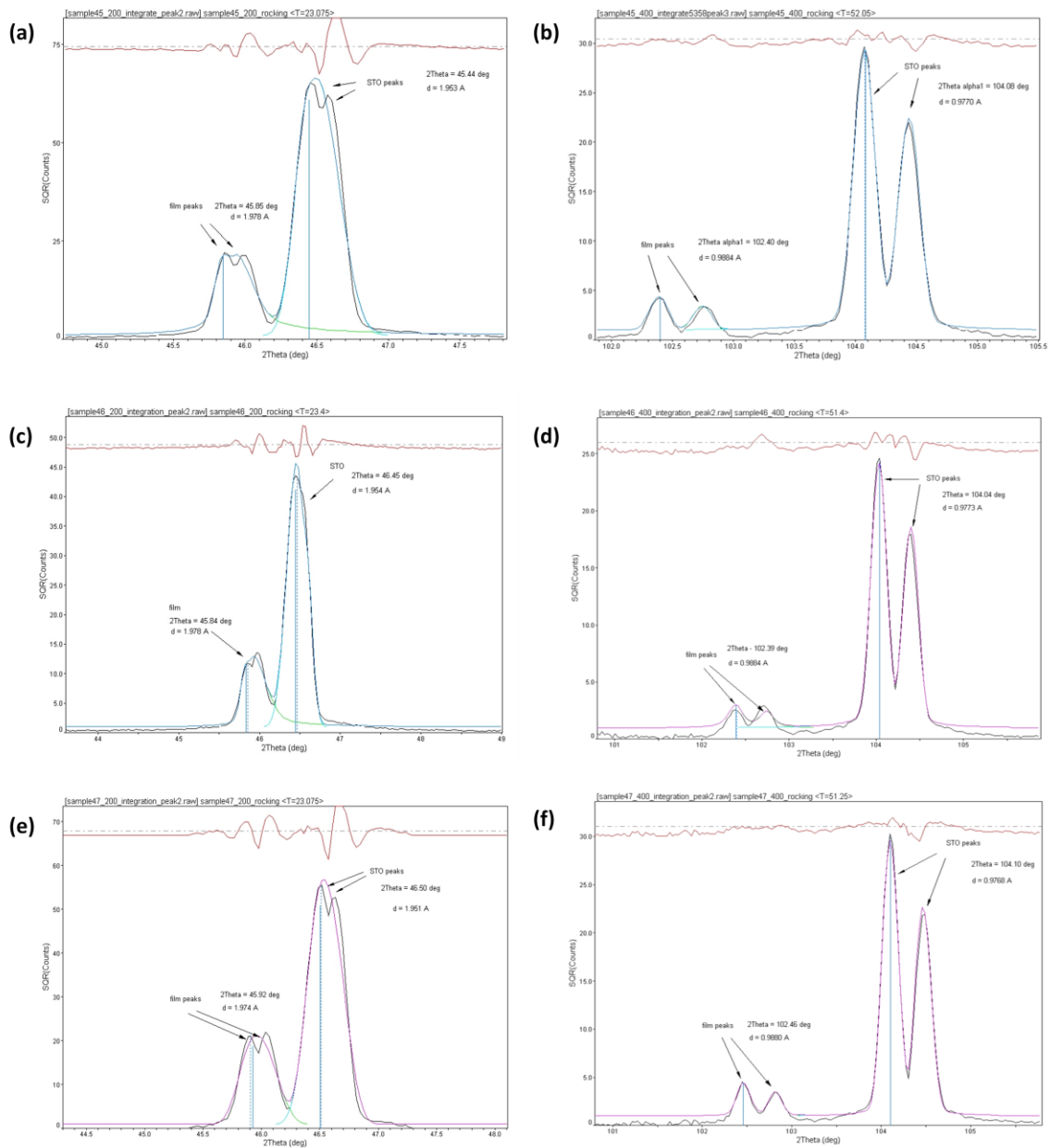


Figure 6.7 X-ray diffraction pattern for BFO-BKT thin films deposited at (a-b) 300 mTorr, (b-c) 400 mTorr, and (c-d) 500 mTorr. The left side images (a, c, d) are for 200, and right side images (b, d, e) are for 400 integration.

Table 6.4 Peak integration parameters for (200) peak profiles

BFO-BKT thin film	2-theta	d-spacing (Å)	FWHM
300mtorr (200)	46.435	1.9535	0.186
400mtorr (200)	46.447	1.9535	0.167
500mtorr (200)	46.504	1.9512	0.195

Figure 6.8 shows the field emission SEM images of surface and cross section for BFO-BKT films grown under different oxygen partial pressure. Firstly, it was observed that surface and cross section images of thin films deposited under different oxygen pressure is uniform, dense, and crack free. Second, there are some obvious particulates in samples deposited at 300 and 400 mTorr oxygen partial pressure. In this case the thin film surface does not appear to change dramatically as a function of oxygen pressure. The SRO bottom electrode and BFO-BKT film thickness was measured from the cross image to be approximately 100 and 600 nm respectively.

Rutherford Backscattering Spectrometry (RBS) results for BFO-BKT thin films deposited under different oxygen pressure are shown in Figure 6.9. The peaks for K, Fe, and Ti overlapped with Bi peak and can't be clearly identified in the spectra. Such overlapping is due to close atomic numbers. Comparing RBS spectrum for different thin films, the simulated data is well fitted to the experimental results. The main effect of varying the oxygen pressure down to 300 mTorr causes the slope of Bi narrowing towards lighter elements. The RBS results indicate that the films, within the detection limit are free of impurities. The Bi/Fe ratio is shown in Table 6.5. According to the

simulation, the Bi/Fe ratio can go down as low as 1.16 without any Fe_2O_3 formation according to XRD results.

The calculated thickness according to RBS results for samples deposited at 300 and 400 mTorr is in agreement with SEM measurements of ~ 600 nm.

Table 6.5 Bi/Fe ratio according to RBS simulation

	Stoichiometry	300 mTorr	400 mTorr	500 mTorr
Bi/Fe ratio	1.33	1.26	1.18	1.16

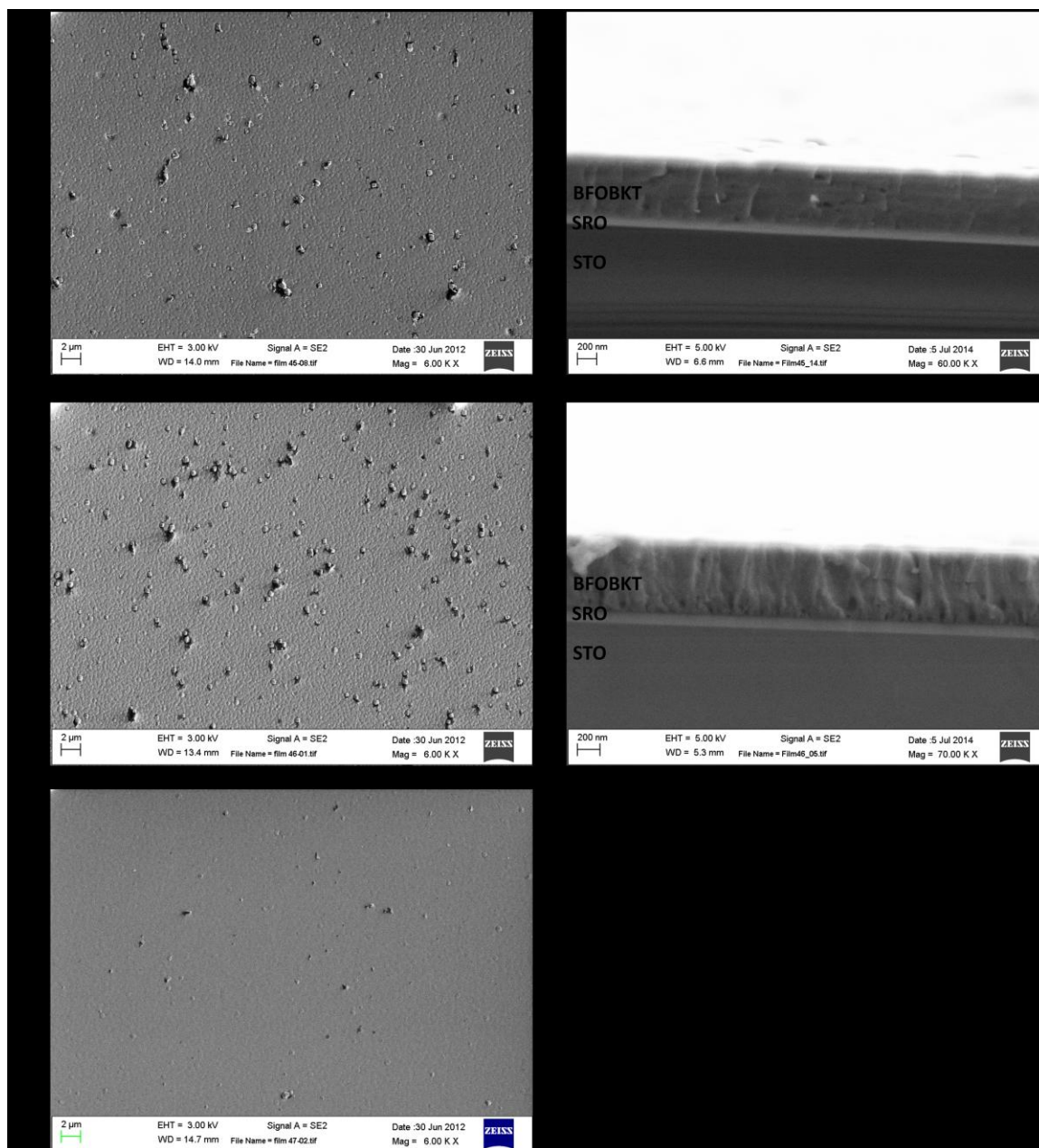


Figure 6.8 Field emission SEM micrographs of surface and cross section for BFO-BKT thin films deposited under different oxygen pressure. (a-b) 300 mtorr, (c-d) 400 mtorr, and (e-f) 500 mTorr.

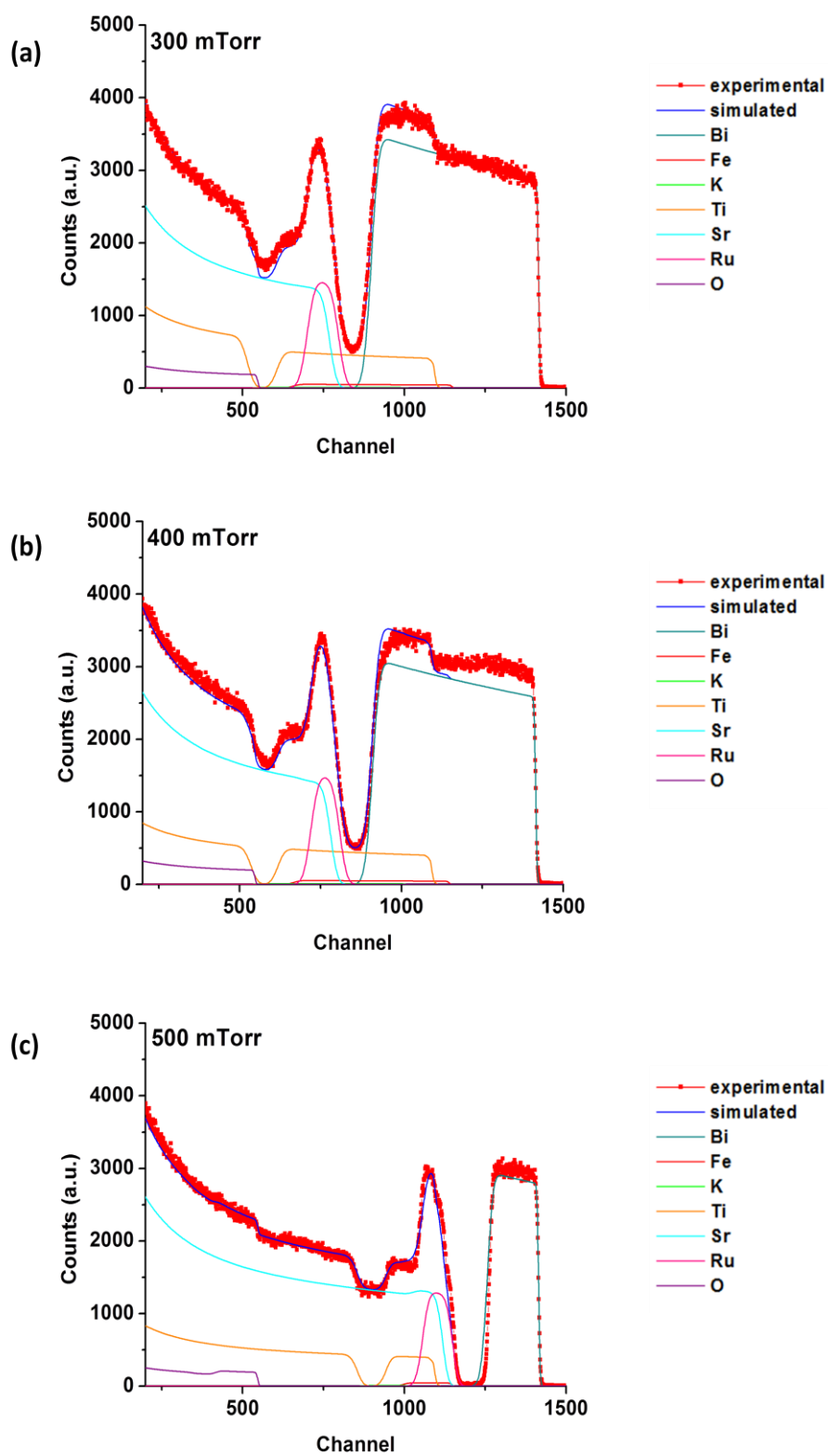


Figure 6.9 RBS spectrum for BFO-BKT thin film deposited at different oxygen pressure.

Polarization-electric (P-E) field hysteresis and leakage current measurements were performed on BFO-BKT thin films deposited under different oxygen partial pressure. Ferroelectric measurements were done at room temperature at 1 kHz. Figure 6.10 shows the hysteresis loop and leakage current results. The BFO-BKT thin films show a well-shape ferroelectric hysteresis loop with no leakage current component in contrast with pure BFO thin films in Section 6.3. P-E hysteresis loops (Figure 6.10a) show remnant polarizations of $2P_r = 33.2, 19.0$ and $16.6 \mu\text{C}/\text{cm}^2$ and coercive fields of $2E_c = 200, 80$ and $80 \text{ kV}/\text{cm}$ for films deposited at oxygen partial pressures of 300, 400 and 500 mTorr, respectively. The remnant polarization and coercive field are higher for thin films deposited at lower oxygen pressure of 300 mTorr. As discussed in the introduction and background sections, bismuth is major contributor to the spontaneous polarization values in BFO. Correlating the composition results from RBS presented in Table 6.4 to the change in remnant polarization values, it is not surprisingly the canting of hysteresis loop for thin films deposited at 400 and 500 mTorr. When more Bi vacancies are introduced the gradual canting in the ferroelectric loop is expected.

Figure 6.10b shows the leakage current density of the BFO-BKT thin films as a function of electric field. It was observed that the leakage current is very sensitive to oxygen partial pressure during the deposition. The leakage current for thin films deposited at 300 mTorr is suppressed by four orders of magnitude compared to the thin films grown at higher oxygen pressure. For thin films deposited at 400 and 500 mtorr the leakage current exhibited an abrupt increase with the applied field above $100 \text{ kV}/\text{cm}$ while samples deposited at 300 mTorr showed a more asymmetric behavior. Similar trend is observed for pure BFO thin films grown by PLD in an oxygen partial pressure range of

150 to 10 mTorr¹⁰. However, the leakage current density is higher (10^{-3} A.cm⁻²) than BFO-BKT thin films (10^{-5} A.cm⁻²) at an applied electric field of 150 kV/cm reported in this investigation.

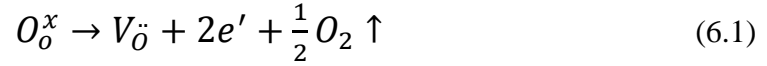
The remnant polarization values for other BFO based solid solution thin films such as: 0.70BiFeO₃-0.3(Bi_{0.5}Na_{0.5})TiO₃ exhibited higher values of 2P_r and 2E_C of 52 μ C/cm² and 560 kV/cm respectively¹. Such reported ferroelectric measurements by *Hieno* were carried out at -190 °C. *Wu et al* reported high polarization values for 0.95BiFeO₃-0.05(Bi_{0.5}Na_{0.5})TiO₃ [100] oriented thin films as 2P_r of 118.2 μ C/cm²¹². Polarization and leakage current density values for different BFO based solid solution reported by other groups are shown in Table 6.6.

Table 6.6 Ferroelectric values for BFO based thin film solid solution.

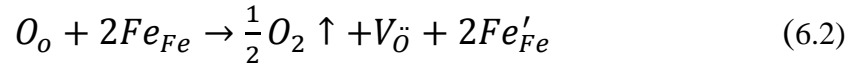
Composition	Deposition method	Measurements Conditions	2P _r (μ C/cm ²)	J _{SC} (A/cm ²) @ 200 kV/cm
0.7BFO-0.3BNT ¹	Sol-gel	-190 C	52	10 ⁻²
0.95BFO-0.05BNT ¹²	RF Sputtering	RT, 1 kHz	118.2	10 ⁻⁵
BFO-BCO ¹³	Sol-gel	RT, 5 kHz	40	10 ⁻⁶
0.6BLFO-0.40PZT ³	RF Sputtering	RT, 5 kHz	122.6	-
0.67BFO-0.33BaTO ¹⁴	PLD (0.25mbar)	RT, 1 kHz	20*	-
0.8BFO-0.2BaT ¹⁵	PLD (0.067mbar)	RT, 10 kHz	38	-
0.6BFO-0.4BKT	PLD (0.40mbar)	RT, 1 kHz	33.2	10 ⁻⁵
This work				

(*) Hysteresis loop not saturated

The leakage behavior in BFO depends on the phase purity, grain size, and defects such as oxygen vacancy, and $\text{Fe}^{3+}/\text{Fe}^{2+}$ ions. The oxygen vacancy plays an important role and is described by the following reaction:



or alternatively the reduction of Fe^{3+} to Fe^{2+} that occurs to compensate the space charge:



The oxygen vacancies formed during the thin film growth cause part of the Fe^{3+} to reduce and become Fe^{2+} . The Fe^{2+} ions are responsible for the high leakage of BFO and the oxygen vacancies act as a space charge, and causes strong domain pinning. Domain pinning creates a mechanical barrier against domain wall and interferes with its movement. An increase in the concentration of oxygen vacancies defects results in a decrease in the remnant polarization¹⁶, and increase coercive field.

The dielectric behavior of the BFO-BKT films was examined in terms of the relative permittivity, ϵ_r , and the dissipation factor ($\tan \delta$) as a function of frequency at room temperature for samples grown under different oxygen partial pressure. Figure 6.11a shows that the films deposited at 500 mTorr have a relatively high dielectric constant at 1 kHz. The dielectric constant for thin films deposited at 300 and 400 mTorr show lower value of 400 but has similar trend vs. frequency. The dielectric constant is quite stable over the investigated frequency range. Figure 6.11b shows that the thin films deposited at lower oxygen partial pressure (300 mTorr) have higher dielectric loss compared to those deposited at 400 and 500 mTorr. The figure also shows the presence of a relaxation regime for samples deposited at 500 mTorr around 100 kHz.

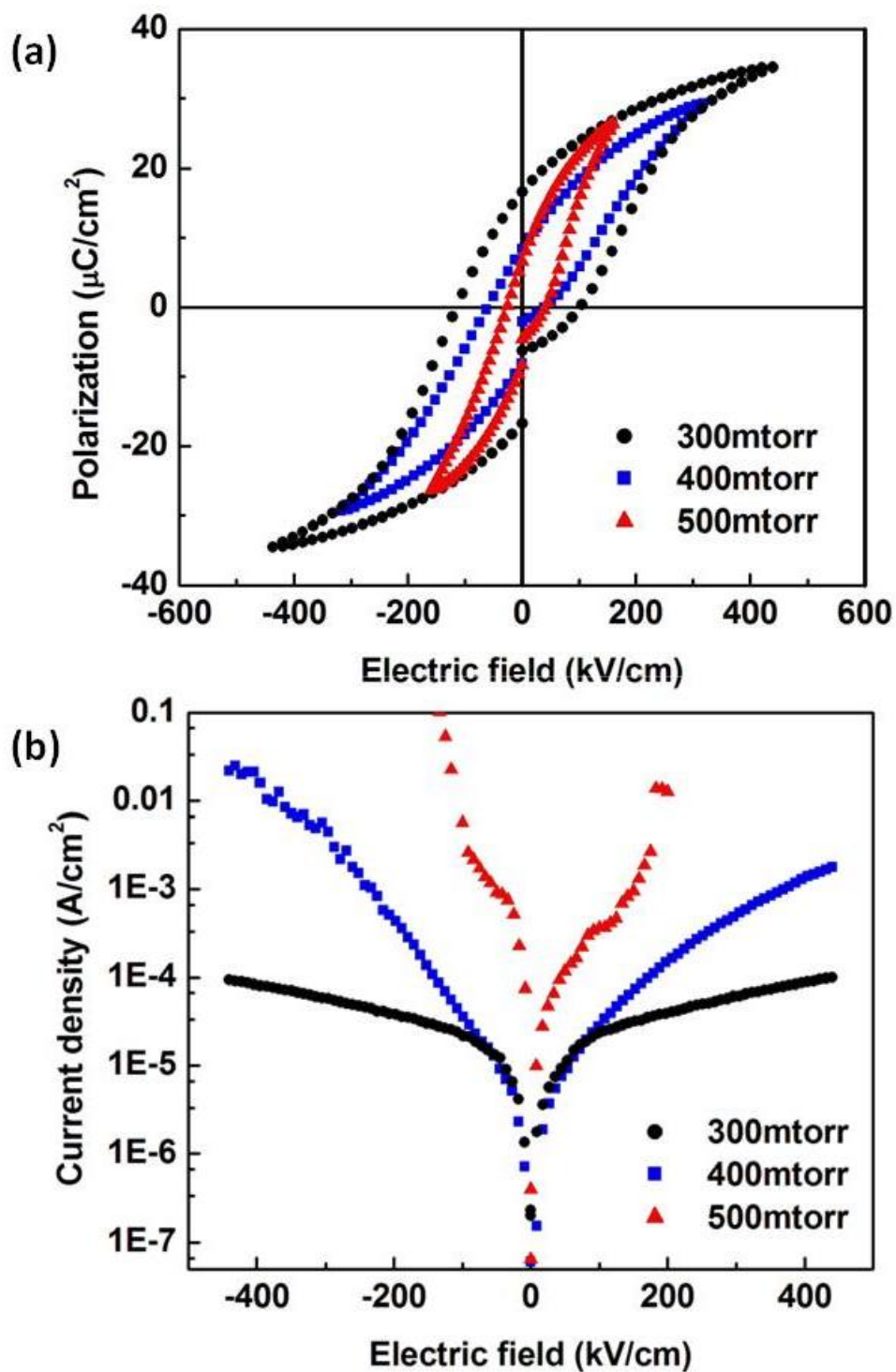


Figure 6.10 (a) Polarization-Electric field (P-E) loops and (b) leakage current characteristics for BFO-BKT thin films deposited in a range of oxygen partial pressure of 300 – 500 mTorr.

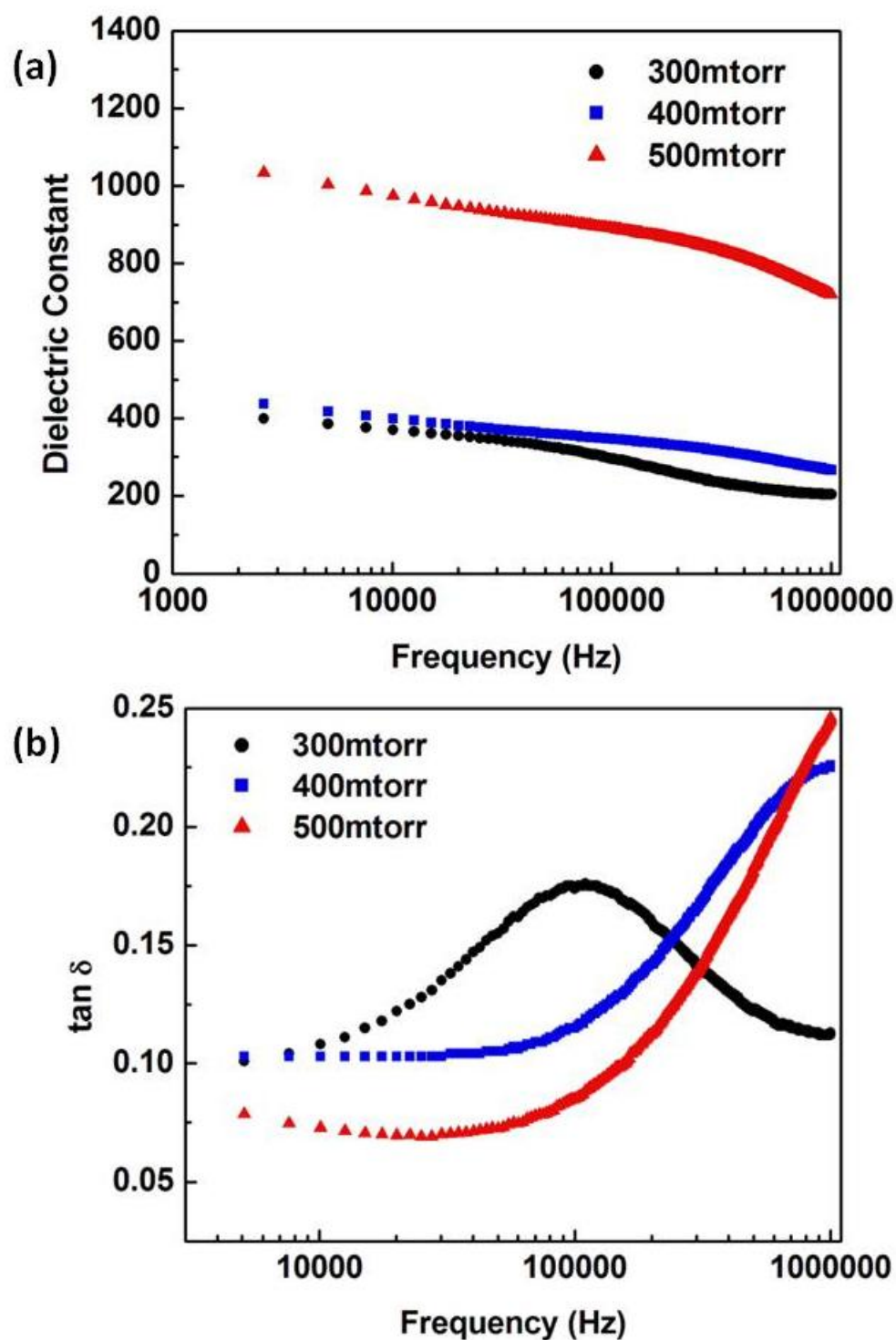


Figure 6.11 Dielectric properties of BFO-BKT thin films deposited in a range of oxygen partial pressure of 300 – 500 mTorr (a) relative dielectric constant, and (b) dielectric loss.

6.3.3 BiFeO₃/(Bi_{0.5}Na_{0.5})TiO₃-(Bi_{0.5}K_{0.5})TiO₃-BaTiO₃ bi-layered

For the fabrication of BFO/BNT-BKT-BT bi-layered thin films, BFO and BNT-BKT-BT ceramic targets were prepared as described previously. The 0.88BNT-0.08BKT-0.04BT composition in the morphotropic phase boundary (MPB) exhibited high electromechanical properties. The fabrication of bi-layered thin films carried out in the following steps: **(1)** deposition of bottom electrode as previously explained under same conditions, **(2)** deposition of BNT-BKT-BT layer at a substrate temperature of 800 °C, oxygen pressure 400 mTorr, laser energy 170 mJ and laser repetition rate 10 Hz, **(3)** deposition of BFO layer accomplished at: temperature of 750 °C, oxygen pressure of 20 mTorr, laser energy of 170 mJ and laser repetition rate of 10 Hz, and **(4)** deposition of metal top electrode (Au) using DC sputtering.

Figure 6.12 shows the XRD pattern for BFO/BNT-BKT-BT bi-layered thin film. Only the perovskite phase was observed where no secondary phase is detected. The XRD spectrum confirmed the epitaxial growth of bi-layered thin film favored by the selected deposition conditions.

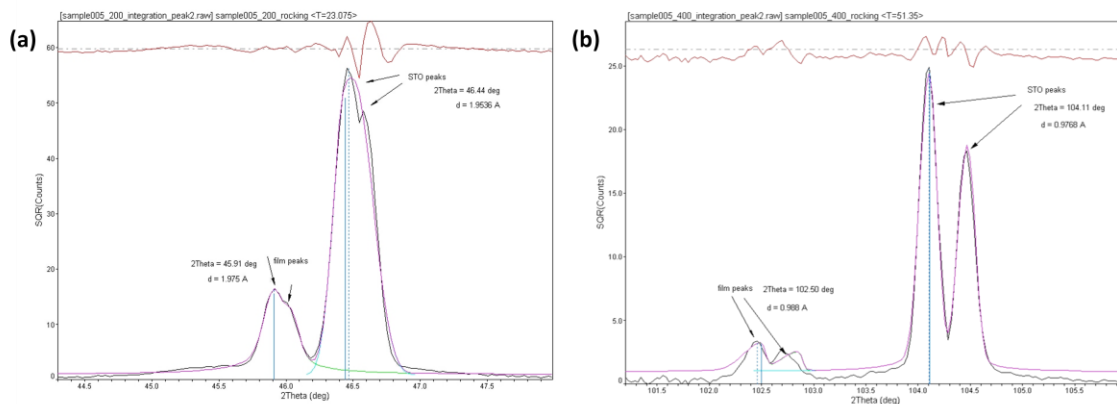


Figure 6.12 x-ray diffraction patterns for BFO/BNT-BKT-BT bi-layered thin film near the (a) (002) integration, and (b) (400) integration.

FESEM image of surface morphology for bi-layered is shown in Figure 6.13. The top layer is the BFO thin film while the BNT-BKT-BT is beneath. The surface appearance is similar as observed for pure BFO single layer thin film in Figure 6.4a. Similar surface characteristics in BFO/BFMO bi-layered microstructure grown by RF sputtering have been reported by *Wu et al*¹⁷. BNT-BKT-BT layer is expected to be smooth, uniform, crack, and pinholes free as found previously¹¹.

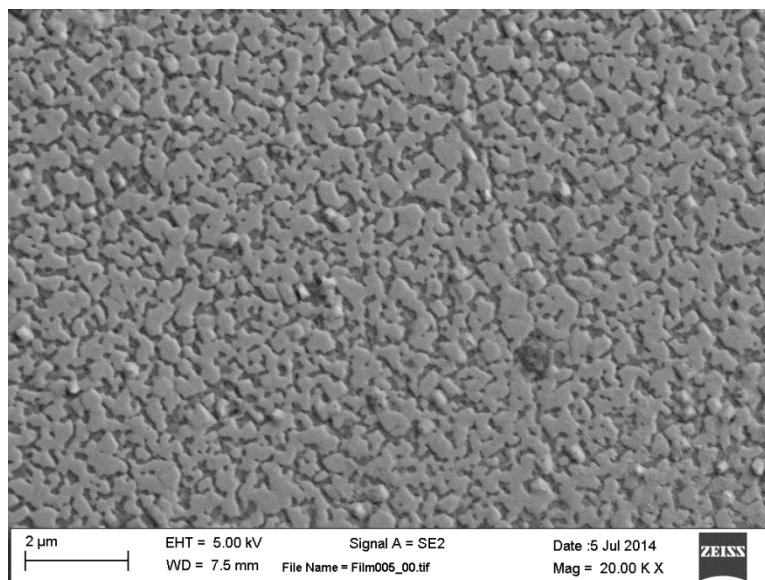


Figure 6.13 FESEM surface image of BFO/BNT-BKT-BT bi-layered.
NOTE: Top layer is BFO.

Hysteresis loop for bi-layered BFO/BNT-BKT-BT thin film in Figure 6.14 demonstrated an improved ferroelectric behavior compared to BFO single layer in Figure 6.6. As can be observed in Figure 6.14a, the P-E hysteresis loop showed a remnant polarization of $2P_r = 44.0 \mu\text{C.cm}^{-2}$ and a coercive field of $2E_c = 142 \text{ kV.cm}^{-1}$. Applying higher voltages to the film resulted in rounded P-E loop which was an indication of high leakage current. Figure 6.14b show the leakage current for single layer BFO, BNT-BKT-BT, and bi-layered BFO/BNT-BKT-BT thin films. Multilayer films showed lower

leakage current compared with pure BFO, but higher than BNT-BKT-BT. Multilayer thin films causes an increase in the leakage current due to the defects developed at the interface between the layers.

The dielectric constant and dielectric loss as a function of frequency for BFO/BNT-BKT-BT bi-layered and BFO single layer thin films are shown in Figure 6.15. *Abazari et al* reported a dielectric constant of 750 at 1 kHz for BNT-BKT-BT thin films ¹⁸. Considering a series connection between BFO and BNT-BKT-BT layers, the equivalent dielectric constant can be calculated using equation 6.3 for bi-layered or multilayer structure which is not in agreement with the obtained experimental results in Figure 6.15a. The dielectric loss values for BFO and BFO/BNT-BKT-BT thin films are similar regardless of the introduction of BNT-BKT-BT layer, confirming the low free movable charge density existing in the BFO films ¹⁹. There is noticeable increase in the dielectric loss for higher frequencies range corresponding to a decrease in the dielectric constant values.

$$\frac{1}{K_{eq}} = \frac{1}{K_{BFO}} + \frac{1}{K_{BNTBKTBT}} \quad (6.3)$$

Some factors that contribute to the improved ferroelectric properties of BFO/BNT-BKT-BT bi-layered thin films in this investigation could be: (1) Reduction of leakage which resulted from introducing of BNT-BKT-BT. (2) The interface coupling between BFO and BNT-BKT-BT should partly enhance the remnant polarization. It is necessary to consider further study the space charge developed at the interface between BFO and BNT-BKT-BT which may bring some complications ⁴. The presence of space charges at the interface has played an important role in the overall ferroelectric behavior of BFO/BNT-BKT-BT thin film.

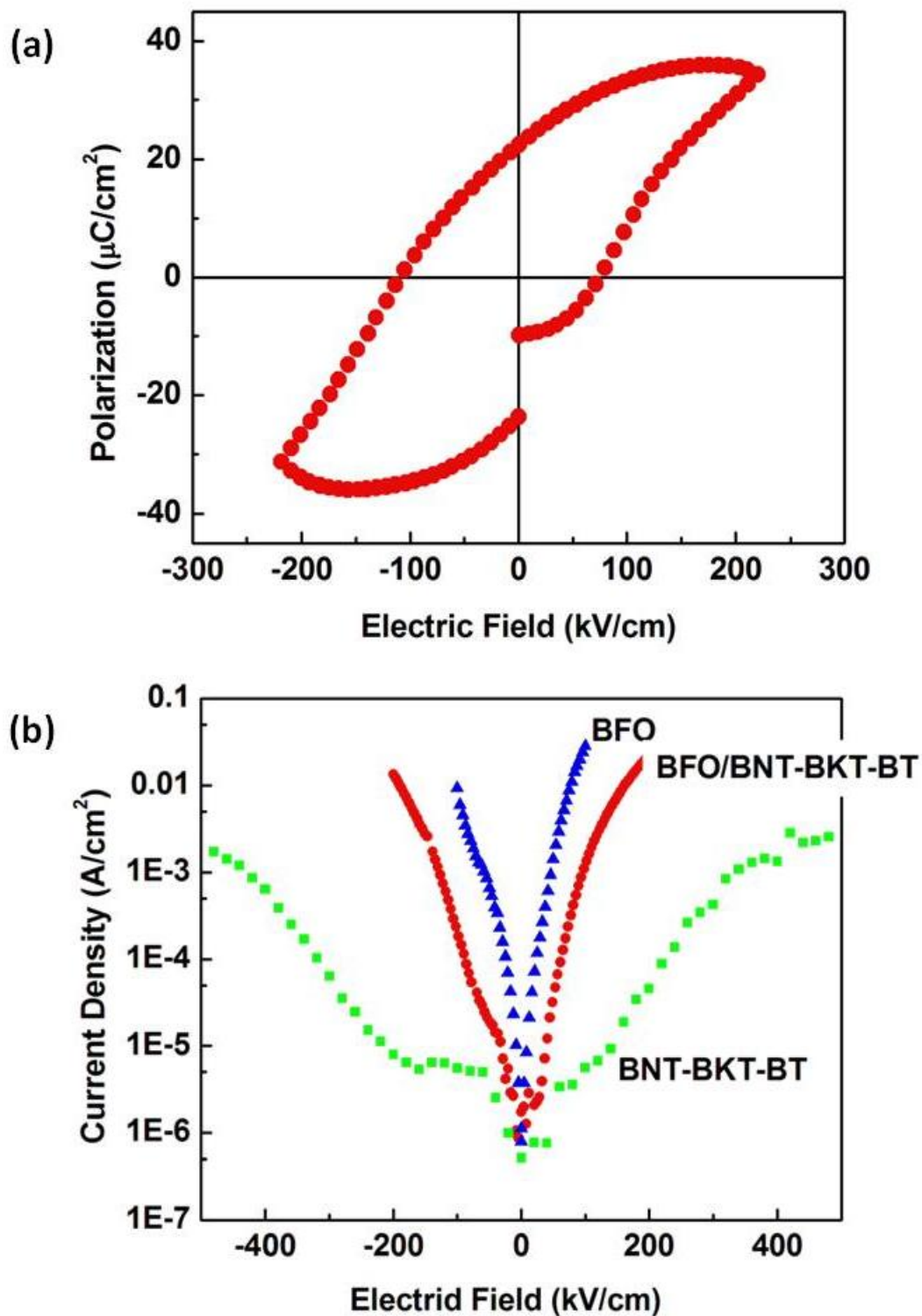


Figure 6.14 (a) P-E loop for BFO/BNT-BKT-BT bi-layered thin film, and (b) leakage current characteristics for BFO, BNT-BKT-BT, and BFO/BNT-BKT-BT thin films.

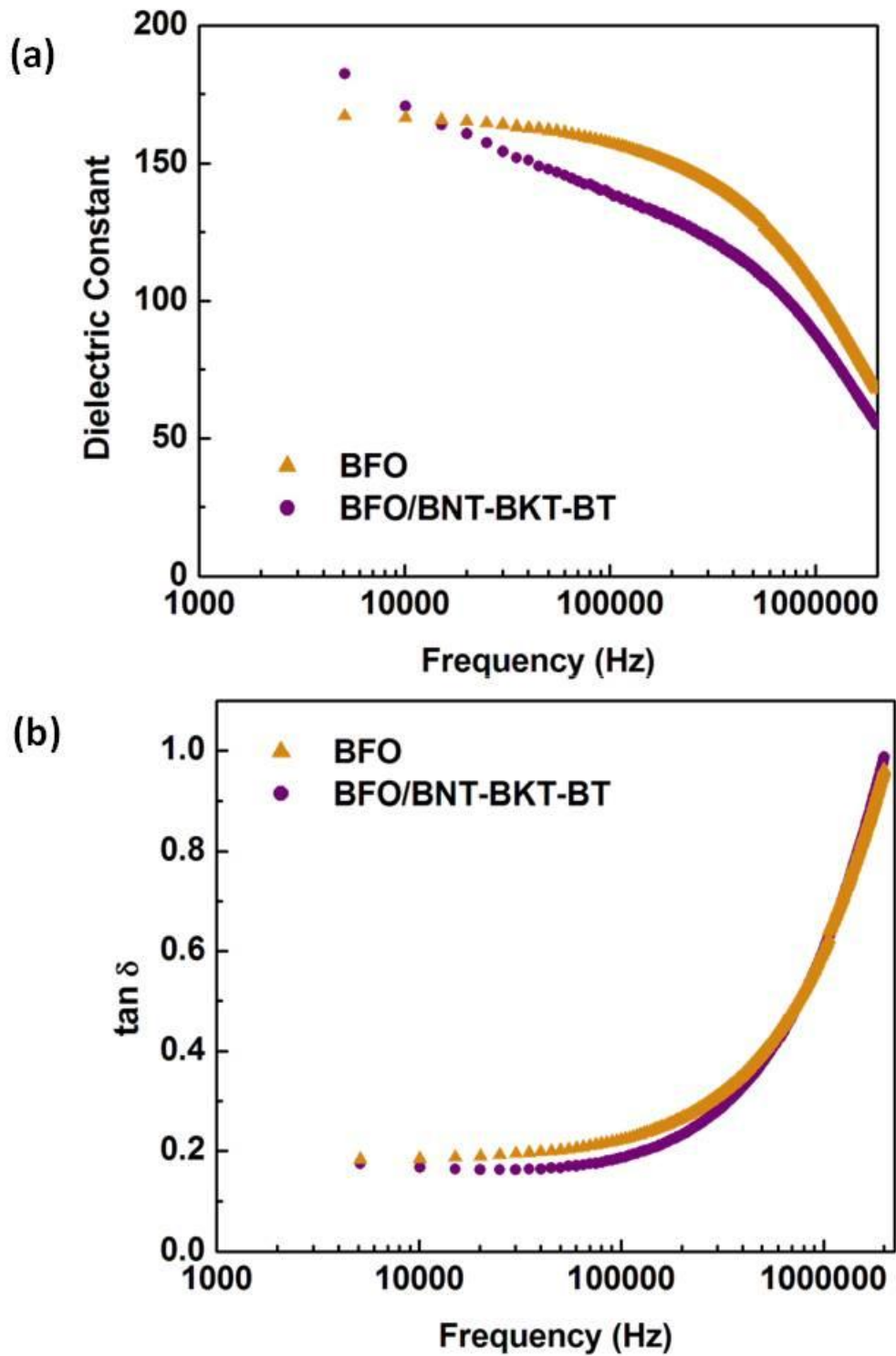


Figure 6.15 Dielectric properties of BFO/BNT-BKT-BT bi-layered thin film (a) relative dielectric constant, and (b) dielectric loss.

6.4 Summary

The fabrication and characterization of BFO-based solid solution and bi-layered thin films have been studied. The thin films were deposited by PLD, and its phase, crystalline structure, surface morphology, composition and ferroelectric properties were characterized. Pure bismuth ferrite thin film showed undesirable ferroelectric properties with high leakage current which correlates with the porous microstructure.

The effect of oxygen background pressure was studied on the fabrication of BFO-BKT solid solution thin films with the objective to improve the ferroelectric properties of BFO. BFO-BKT optimum properties were obtained at 300 mTorr oxygen partial pressure with a remnant polarization of $16.2 \mu\text{C}/\text{cm}^2$, and minimum leakage current of $10^{-4} \text{ A}/\text{cm}^2$. The leakage current was suppressed by four orders of magnitude compared to thin films deposited at 500 mTorr. Thin films exhibited better crystallinity and optimum Bi/Fe ratio in for samples deposited at 300 mTorr which correlate with the properties enhancement.

As a second approach to improve the properties of BFO, a bi-layered design was also studied. BFO/BNT-BKT-BT bi-layered was deposited also by PLD. The surface microstructure studied by FESEM exhibited similar characteristics to pure BFO. However, the BNT-BKT-BT layer beneath BFO promotes improvement ferroelectric properties and leakage current. Bi-layered thin film exhibited remnant polarization values of $22.0 \mu\text{C}.\text{cm}^{-2}$ and leakage current of $2.2 \times 10^{-4} \text{ A}.\text{cm}^{-2}$ at $100 \text{ kV}.\text{cm}^{-1}$.

The results showed that BFO-BKT and bi-layered BFO/BNT-BKT-BT thin films approaches effectively enhance ferroelectric and electrical properties pure BFO thin films.

6.5 References

1. Hieno, A., Sakamoto, W., Moriya, M. & Yogo, T. Synthesis of BiFeO₃--Bi_{0.5}Na_{0.5}TiO₃ Thin Films by Chemical Solution Deposition and Their Properties. *Jpn. J. Appl. Phys.* **50**, (2011).
2. Achenbach, G. D., James, W. J. & Gerson, R. Preparation of Single-Phase Polycrystalline BiFeO₃. *J. Am. Ceram. Soc.* **50**, 437–437 (1967).
3. Wu, J., Zhang, B. & Wang, X. Bismuth ferrite composite thin films. *Appl. Phys. A* **111**, 1017–1020 (2013).
4. Wu, J., Kang, G., Liu, H. & Wang, J. Ferromagnetic, ferroelectric, and fatigue behavior of (111)-oriented BiFeO₃/(Bi_{1/2}Na_{1/2})TiO₃ lead-free bilayered thin films. *Appl. Phys. Lett.* **94**, 172906 (2009).
5. Ihlefeld, J. F. *et al.* Adsorption-controlled molecular-beam epitaxial growth of BiFeO₃. *Appl. Phys. Lett.* **91**, 071922–071922–3 (2007).
6. J. F. Ihlefeld, N. J. P. Optical band gap of BiFeO₃ grown by molecular-beam epitaxy. *Appl. Phys. Lett. - APPL PHYS LETT* **92**, 2908–142908 (2008).
7. Wang, C. *et al.* Leakage current of multiferroic (Bi_{0.6}Tb_{0.3}La_{0.1})FeO₃ thin films grown at various oxygen pressures by pulsed laser deposition and annealing effect. *J. Appl. Phys.* **99**, 054104 (2006).
8. Wang, J. *et al.* Epitaxial BiFeO₃ Multiferroic Thin Film Heterostructures. *Science* **299**, 1719–1722 (2003).
9. Ahadi, K., Mahdavi, S. M., Nemati, A. & Kianinia, M. Photoconductivity and diode effect in Bi rich multiferroic BiFeO₃ thin films grown by pulsed-laser deposition. *J. Mater. Sci. Mater. Electron.* **22**, 815–820 (2011).
10. Yun, K. Y. *et al.* Structural and multiferroic properties of BiFeO₃ thin films at room temperature. *J. Appl. Phys.* **96**, 3399–3403 (2004).
11. Hejazi, M., Jadidian, B. & Safari, A. Lead-free (Bi_{0.5}Na_{0.5})TiO₃-based thin films by the pulsed laser deposition process. *IEEE Trans. Ultrason. Ferroelectr. Freq. Control* **59**, 1855–1863 (2012).
12. Wu, J. & Wang, J. Multiferroic behaviour and orientation dependence of lead-free (1 – x)BiFeO₃–x(Bi_{0.50}Na_{0.50})TiO₃ thin films. *J. Phys. Appl. Phys.* **42**, 195405 (2009).
13. Singh, S. K., Shanthi, S. & Ishiwara, H. Reduced leakage current in BiFeO₃-BiCrO₃ nanocomposite films formed by chemical solution deposition. *J. Appl. Phys.* **108**, 4102 (2010).
14. Michael Lorenz, V. V. L. Multiferroic BaTiO₃–BiFeO₃ composite thin films and multilayers: strain engineering and magnetoelectric coupling. *J. Phys. Appl. Phys.* **47**, 135303 (2014).
15. Sasaki, T., Hirabayashi, Y., Kobayashi, H. & Sakashita, Y. Effect of Dopant on Piezoelectric Properties of Lead-Free BiFeO₃–BaTiO₃ Film. *Jpn. J. Appl. Phys.* **50**, 09NA08 (2011).
16. Noguchi, Y., Miwa, I., Goshima, Y. & Miyayama, M. Defect Control for Large Remanent Polarization in Bismuth Titanate Ferroelectrics –Doping Effect of Higher-Valent Cations–. *Jpn. J. Appl. Phys.* **39**, L1259 (2000).
17. Wu, J. *et al.* Effect of bilayer structure and a SrRuO₃ buffer layer on ferroelectric properties of BiFeO₃ thin films. *Appl. Phys. A* **109**, 57–61 (2012).

18. Abazari, M., Safari, A., Bharadwaja, S. S. N. & Trolier-McKinstry, S. Dielectric and piezoelectric properties of lead-free (Bi,Na)TiO₃-based thin films. *Appl. Phys. Lett.* **96**, 082903 (2010).
19. Wu, J., Wang, J., Xiao, D. & Zhu, J. Combined effects of bilayer structure and ion substitutions on bismuth ferrite thin films. *J. Appl. Phys.* **109**, 4101 (2011).

7 Bismuth Ferrite Nanofibers by Electrospinning

7.1 Introduction

Bismuth ferrite has attracted extensive research activities because its multiferroic properties. While investigators are studying the ferroelectric properties from a fundamental physical and experimental perspective, the understanding of its optical properties such as band gap, photoconductivity for novel applications is emerging. Recent investigations on BFO photovoltaics cause a great interest in its novel multifunctional applications. Bismuth ferrite is a semiconductor material with an optical band gap between 2.17-2.81 eV which falls in the visible light region.

On the other hand, one dimensional nanostructures, including nanofibers (lateral size < 100 nm), nanowires (lateral size > 100 nm), and nanotubes have received considerable attention due to their tunable electromechanical, photovoltaic and optoelectronic properties¹.

This chapter presents the optimization process to develop bismuth ferrite nanofibers with different diameter by electrospinning technique. The phase, structure, composition, morphology, valence state, and electronic properties are characterized. Developed bismuth ferrite nanofibers have been used to fabricate field effect transistor devices.

7.2 Experimental procedure

7.2.1 Electrospinning setup

The electrospinning technique is a simple and yet versatile method to fabricate ultra thin fibers from a diversity of materials which includes polymers, composites, and ceramics.² Electrospinning is continuous process and therefore suitable for high-volume production. The electrospinning principal is based on an electrostatic force interaction in which a high electric field is applied on a droplet of a polymer based solution held by its surface tension at the tip of a syringe needle³. The droplet is highly charged and the induced charges are distributed over its surface. By adjusting the electric field, the shape of the droplet is distorted and form a conical form known as a “Taylor cone”^{4,5}. When the electric field is high enough to overcome the surface tension of the droplet the repulsive forces dominates and the liquid emerges from the cone tip as jet (stream). The jet is accelerated toward the collector and quickly thins and dries as a result of solvent evaporation and elongation³. Finally, the solidification occurs at the surface of the collector or substrate as randomly oriented mat.

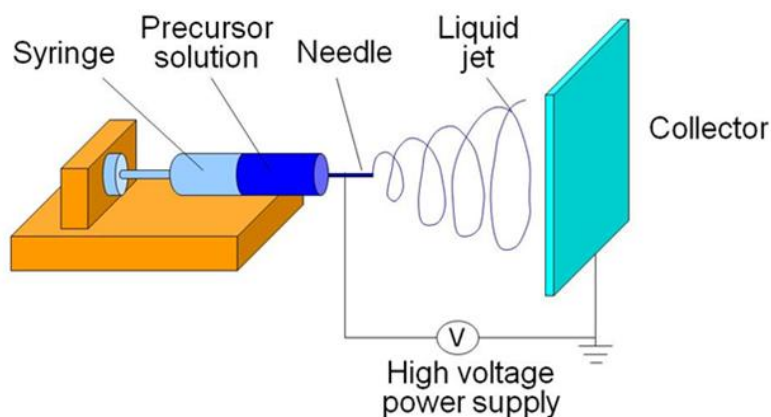


Figure 7.1 Schematic for electrospinning setup.

The physical characteristics of electrospun nanofibers such as diameter depend on various parameters which can be grouped in following three categories:

- (1) Solution properties (viscosity, concentration, polymer molecular weight, and surface tension)
- (2) Processing conditions (applied voltage, flow rate, spinning distance and needle diameter), and
- (3) ambient conditions (temperature, humidity, and atmosphere pressure) ⁶.

Different applications require nanofibers with desired characteristics, suggesting the importance of the process protocol ³. Control over the fiber diameter still is not well established in experimental procedure. Some empirical observations suggest that the diameter could be varied by the flow rate. Considering that electrospun nanofibers are produced from a precursor solution, the dry nanofibers diameter can be controlled with the solution concentration ⁷.

7.2.2 Standard operation procedure (SOP)

1. Polymer selection:

- a. Select a polymer according to the desired specifications such as biodegradable, thermoplastic, and cross-linkable.
- b. Select the appropriate solvent for polymer.
- c. Choose a substrate based on your application (glass, metal, plastic or silicon wafer).

2. Collector selection:

- a. Select a collector geometry based on your desired nanofibers alignment/orientation. Aligned nanofibers can be obtained using rotating wheels, drums, rods or parallel plates. Random nanofibers can be obtained in stationary plates.
- b. The collector must be conductive and need to be grounded.

3. Approximate entangle concentration:

- a. Prepare several precursor solution concentrations which are liquid but do not form a gel.
- b. Start the electrospinning setup.
 - i. Load the precursor solution onto the syringe
 - ii. Load the syringe pump and set the pump speed
 - iii. Ground the collector (20 cm apart from the needle, to start) and connect to the high voltage wire to the needle.
 - iv. Fix the substrate with a double sided tape on the collector.
 - v. Make sure the power supply is set to zero before turning on.

- vi. Turn ON the power supply and wait to warm up for five minutes.

Note: Safety precautions must be taken when working with high power supply.

- vii. Turn the HV ON and wait to warm up for few minutes.

4. Observe the jet:

- i. Ramp the voltage (5kV to start) slowly and watch the drop of the solution at the end of the needle.
- ii. Increase the voltage to obtain a steady solution jet.

Note: If steady solution jet cannot be obtained adjust the solution concentration, flow rate or distance between the needle and the collector.

5. Troubleshooting – the jet:

- a. Trouble viewing the jet: use a dark matte background.
- b. Dripping from the syringe tip: make sure the conductor wire is making contact and collector is properly connected to ground.
- c. Large globs at the syringe tip: swipe the glob away with a paper towel.
Note: Attached the paper towel to a non-conductive stick
- d. Oscillating or “wagging” jet: decrease the voltage or increase the distance between the needle and the collector.

6. Troubleshooting – fiber morphology:

- a. Beading: increase solution concentration or the distance between the needle and the collector.

- b. Forming ribbons: use a higher concentration of polymer or a solvent with higher evaporation rate.
- c. Porosity: if porous fibers are desired use a high rate evaporating solvent, if porous fibers are not desired add a small amount of co-solvent that is less volatile than the major solvent.
- d. Alignment: increase the alignment by increasing the speed of rotation tool (wheel, drum, rods or plates).

7.2.3 Sol gel solution preparation

The preparation of BFO nanofibers involves the following general steps:

- (1) preparing the precursor solution
- (2) electrospinning to obtain inorganic/organic nanofibers
- (3) Heat treatment of the as spun nanofibers to remove the polymer and obtain dense and crystalline BFO fibers.

The sol gel solution was prepared as follows. The nitrates based solution, referred as Solution A, was prepared by dissolving $\text{Bi}(\text{NO}_3)_3 \cdot 5\text{H}_2\text{O}$ and $\text{Fe}(\text{NO}_3)_3 \cdot 9\text{H}_2\text{O}$ in a combination of 2-methoxyethanol and glacial acetic acid with 2:1 ratio. The solution was under constant stirring for one hour at room temperature. Then, a 15 wt% polymer solution referred as Solution B, was prepared by adding polyvinyl pyrrolidone (PVP) with a molecular weight (MW) of 630,000 to dimethyl formamide (DMF) with a ratio of 1:5 (wt/wt) respectively. The solution was stirred for two hours or until the polymer had completely dissolved in DMF. To obtain a homogenous distribution of BFO solution into the polymer, nitrates solution was added drop by drop to polymeric solution while stirring

at room temperature. **Note:** The PVP was added to assist in the fiber formation which later is removed by heat treatment. In order to prepare nanofibers of different diameter, solutions with different concentrations in the range of 0.4 - 1.4 M were prepared. Using an electrospinning apparatus, BFO nanofibers were deposited on Si/SiO₂ and quartz substrates. Electrospinning was conducted at 12 kV with 20 cm separation between the needle tip and the collector. The obtained nanofibers were dried in a closed furnace at 120 °C for 1 hour, followed by a polymer removal step at 400 °C for 1 hour, and final crystallization at 550 °C for 2 hours.

7.3 Fabrication and characterization of bismuth ferrite nanofibers

Following SOP described in Section 7.2.2, this section focused in the process optimization for the development of BFO nanofibers with different diameter. Bismuth ferrite nanofibers with good physical properties (morphology) have been fabricated earlier by *Baji et al.*¹. However, there are no report on the variation of nanofibers diameter and its effect on the electrical properties. Starting solution parameters such as polymer, solvent, co-solvent ratio, and raw materials have been obtained from the literature. To ensure the good morphology and microstructure of the nanofibers, the apparatus settings such as driving voltage, flow rate, and distance between the collector and syringe are optimized. Control over the nanofibers diameter is accomplished by varying the precursor solution concentration. The crystal structure, morphology, grain size, valance state of the nanofibers were studied.

7.3.1 Optimization of processing and solution conditions

A BFO precursor solution of 0.6 M concentration was used to determine the optimum processing conditions and to achieve a continuous solution jet to result in good fiber morphology. The collector geometry was selected as a stationary plate which resulted in randomly deposited nanofibers. The starting distance between the needle and the collector was initially set to 20 cm. The processing optimization results are summarized in the following tables.

Table 7.1 Electrospinning processing optimization: **Flow rate**

Flow rate	Troubleshooting the jet
1.0ml/hr	Beaded-nanofibers, solution dripping continuously
0.8ml/hr	Beaded-nanofibers, solution dripping continuously
0.6ml/hr	Beaded-nanofibers, solution dripping at further distance
0.4ml/hr	Beaded-nanofibers reduced, droplet stable at the tip
0.2ml/hr	Free-beaded nanofibers, droplet stable at the tip *

Table 7.2 Electrospinning processing optimization: **Voltage**

Voltage	Troubleshooting the jet
6 kV	Droplet at the needle tip
8 kV	Droplet at the needle tip, which slowly deforms and dripping down
10 kV	Drop forms at the needle tip, slowly deforms, and a jet is ejected. However, the jet is short and discontinuous.
12 kV	Drop forms at the needle tip, slowly deforms, and a continuous jet is occurring. *
14 kV	Drop forms at the needle tip, more quickly deforms and the jet is ejected. The jet is moving from side to side (“wagging”).

Table 7.3 Electrospinning processing optimization:
Spinning distance (between the needle and the collector)

Distance	Troubleshooting the fiber morphology
15 cm	Fibers with beads of different size in diameter, the coverage area by fibers is large
20 cm	Fibers with less amount of beads, the coverage area by fibers is large *
25 cm	Fibers with no beads, the coverage area by fibers decreased
30 cm	Fibers with no beads, the coverage area by fibers decreased noticeable. Longer deposition time is needed to obtain a dense fibers coverage area.

The effect of the spinning distance on the nanofiber morphology is also shown in Figure 7.2 through optical images. The beads present within the fibers are pointed with a red arrow.

Optimum processing parameters to make uniform and continuous nanofibers have found to be as: 0.2 ml/hr flow rate, 10kV driving voltage, and 25 cm spacing between the needle tip and the conductive collector.

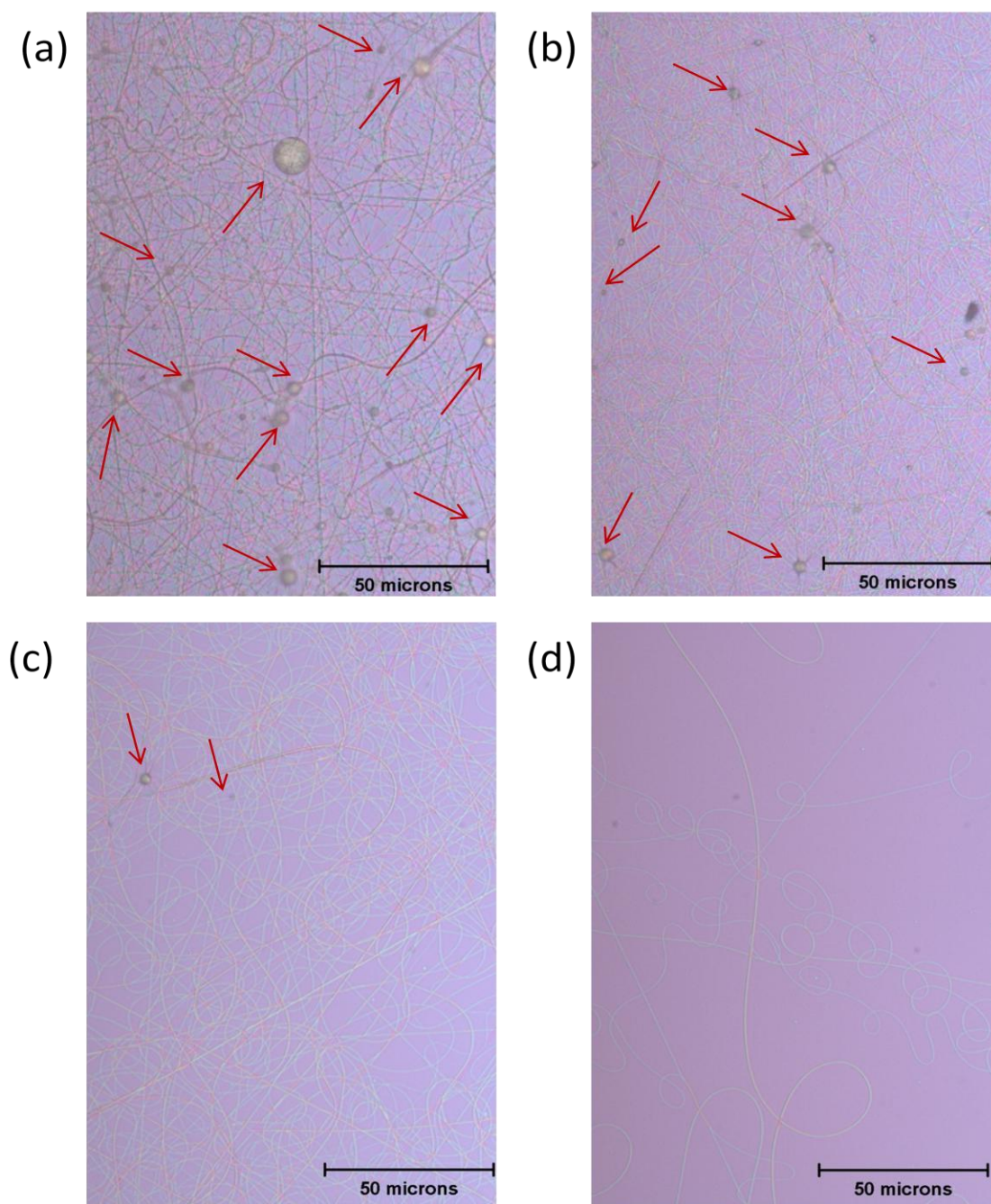


Figure 7.2 Nanofibers deposited at separated distance between the needle and collector of (a) 15, (b) 20, (c) 25, and (d) 30 cm.

7.3.2 Characterization of bismuth ferrite nanofibers

It is difficult to perform XRD analysis directly on electrospun nanofibers because of the low coverage area of nanofibers and high background contribution from the substrate. Hence, to ensure pure perovskite phase of BFO nanofibers, thin films with thickness of 100 nm were prepared by spinning the same precursor solution batches. The XRD pattern of the films in Figure 7.3 revealed pure perovskite phase with a rhombohedral structure. To further confirm the structure and phase of BFO nanofibers, Raman Spectroscopy and TEM analysis was carry out.

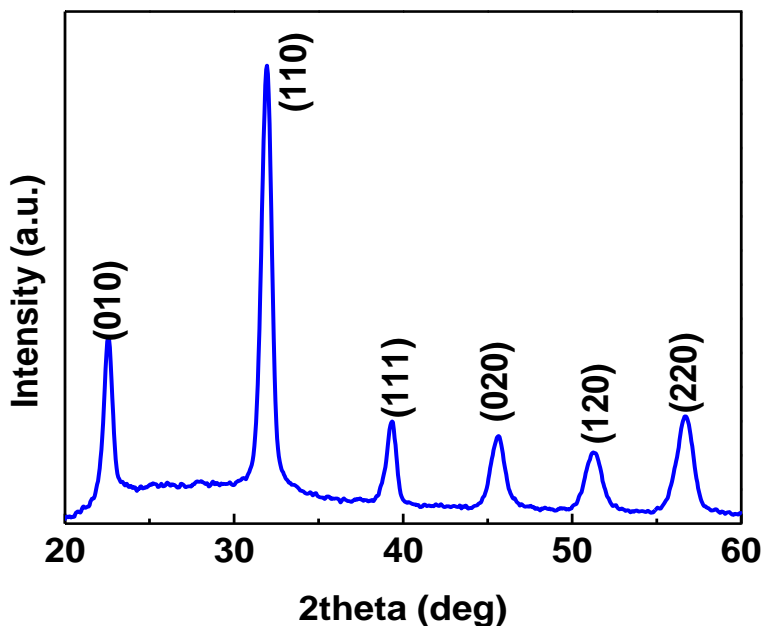


Figure 7.3 X-ray diffraction pattern for a BFO thin film of the same precursor solution as the nanofibers.

For further insight into the lattice properties and spin-phonon mode coupling, **Raman scattering** studies have also been carried out on BFO nanofibers. Figure 7.4 shows the Raman spectra of the nanofibers mat at room temperature. **NOTE:** A fiber mat is a very dense area filled with nanofibers in which the substrate is 90% covered. The fiber mat was prepared under the optimum conditions from a 0.6 M BFO precursor solution with a deposition time of 2 hours. The rhombohedral (R3c) structure of BFO give rises to 13 Raman actives modes listed as $4A_1 + 9E$ as shown in Table 5.1^{8,9}. The observed natural frequency (cm^{-1}) of each peak position can be designed to a different Raman active mode. It appears that several peaks is absent in in Fig 7 spectra based on Raman phonon peaks in Table 5.1. The absence of some of the Raman peaks may be due to the higher local stress in the nanofibers as has been discussed by *Singh et al*¹⁰.

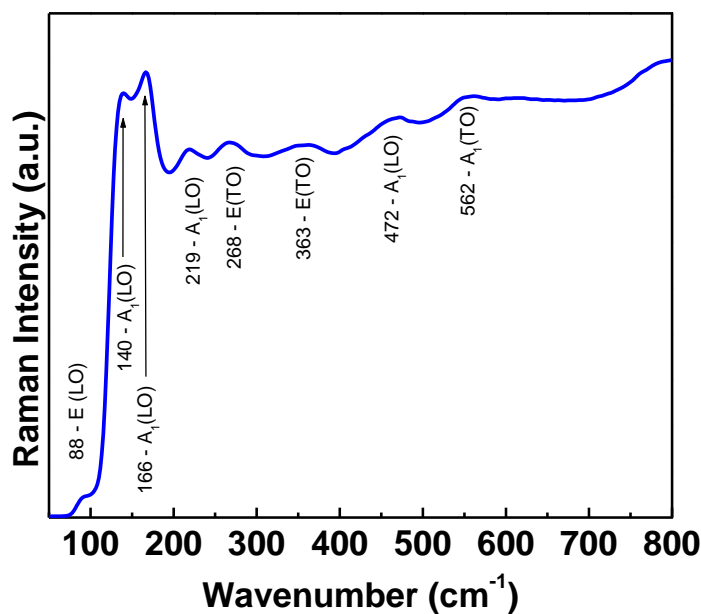


Figure 7.4 Raman Spectroscopy for 0.6M BFO nanofibers mat.

The Figure 7.5 shows the **TEM** image for a single BFO nanofiber deposited under optimum condition with a diameter of 100 nm. TEM results reveal the nanocrystalline nature of electrospun nanofibers. The d-spacing for the BFO nanofiber from the selective area diffraction (SAED) pattern in Figure 7.5b corresponding to R3c space group which is shown in Table 7.4. Raman and TEM results confirmed that BFO nanofibers are well crystallized with single phase rhombohedral structure.

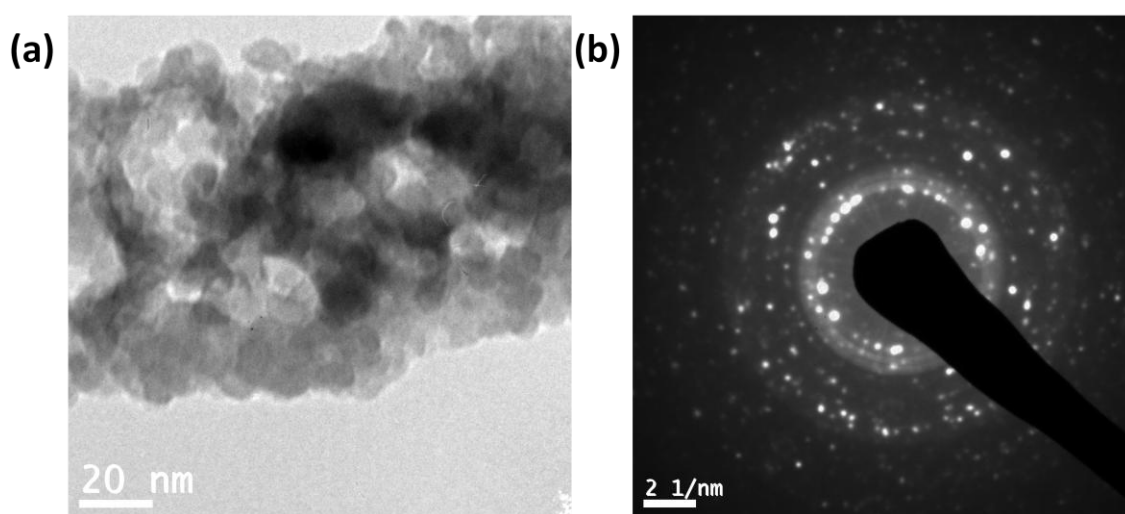


Figure 7.5 Transmission electron microscope (TEM) image for a 100 nm nanofibers. (a) surface image, and (b) diffraction pattern

Table 7.4 d-spacing for single BFO nanofibers from TEM

d-spacing Standard Hexagonal (R3c)	d-spacing from this work
0.3968 (012)	0.390
0.2818 (104)	0.274
0.2391 (113)	0.240
0.2311 (202)	0.230
0.2284 (202)	0.221
0.1984 (024)	0.190
0.1618 (214)	0.160
0.1397 (220)	0.135
0.1252 (134)	0.121
0.1195 (226)	0.119

7.3.3 Nanofibers with different diameters

Leach et al. reported solution concentration plays an important role on the final grain size using a similar deposition technique ¹¹. Solution surface tension and solution viscosity are also important determining parameters to define the concentrations of solution and hence surface quality of continuous nanofibers prepared by electrospinning method ⁷. Under certain viscosity range, the surface tension plays a dominant rule on the fiber morphology. Above certain viscosity the production of nanofibers cannot be possible.

One of the objectives of this research is to fabricate BFO nanofibers with different diameters. The polymer solution concentration and electrospinning processing parameters were kept constant (0.2 ml/hr flow rate, 10kV driving voltage, and 20 cm spacing between the needle tip and the conductive collector) as optimized in Section 7.3.1; and only BFO nitrates solution concentration was varied between 0.4 and 1.4 M. It was observed that below 0.4 M concentration there were a combination of fibers and beads, and the formation of a continuous jet was not obtained for solution concentrations higher than 1.4 M. For the higher concentration forcing the solution through the syringe needle was difficult, and the needle clogged. Nanofibers free of beads were obtained from solution concentrations between 0.4 and 1.4 M. the amount of collected nanofibers per area also increases as the concentration reach to 1.4 M. The nanofibers morphology and diameter was analyzed using the SEM. Micrographs for nanofibers of different solution concentrations are shown in Figure 7.6. The obtained SEM micrographs were utilized to quantify the nanofibers diameter using the software Image J. It was found that by increasing the precursor solution concentration the nanofibers diameter increases as

shown in Figure 7.7. The high standard deviation at the high solution concentration is related to fibers that joint each other as shown in Figure 7.8.

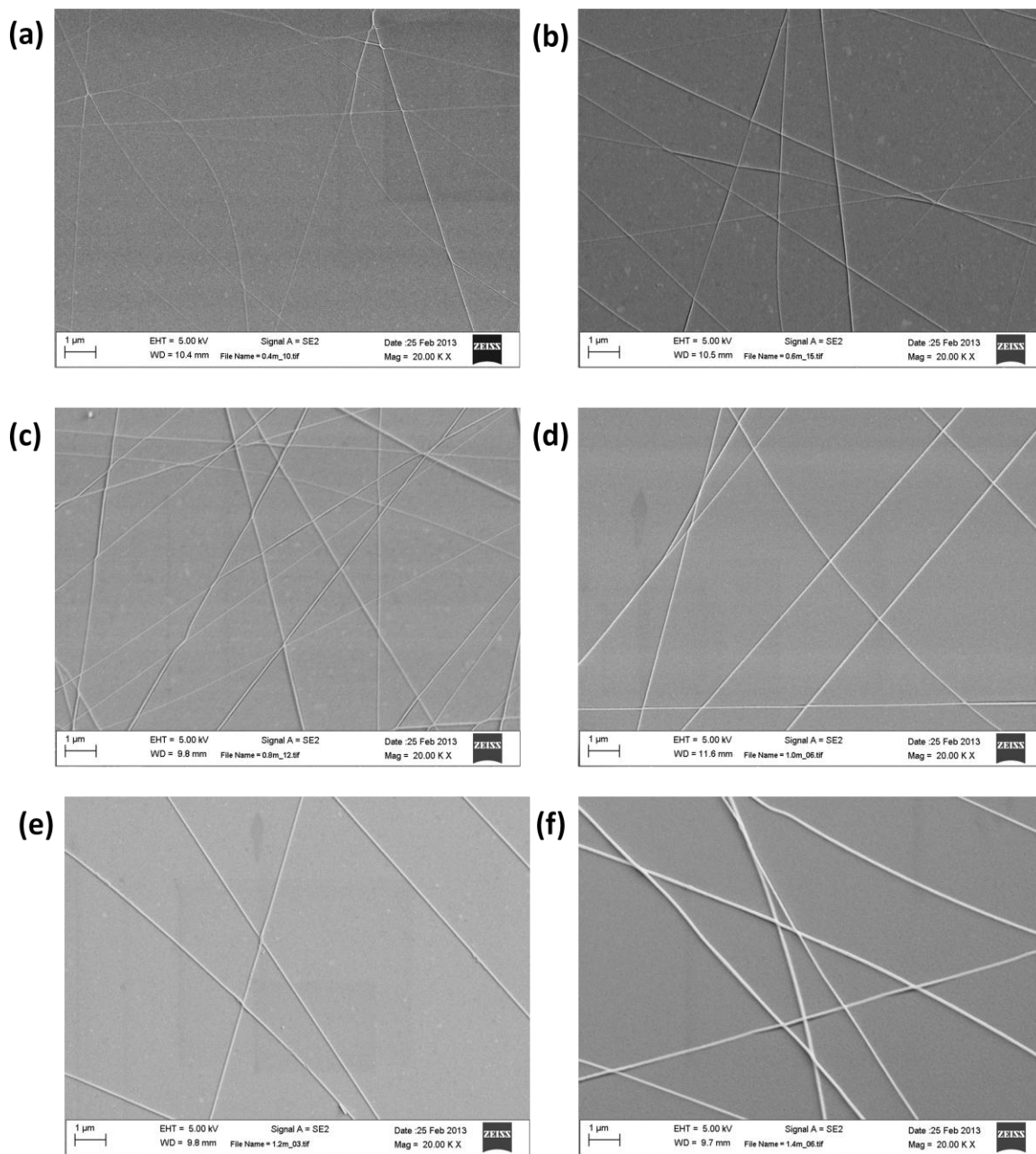


Figure 7.6 SEM surface micrographs for electrospun nanofibers of different precursor solution concentrations. (a) 0.4M, (b) 0.6M, (c) 0.8M, (d) 1.0M, (e) 1.2M, and (f) 1.4M

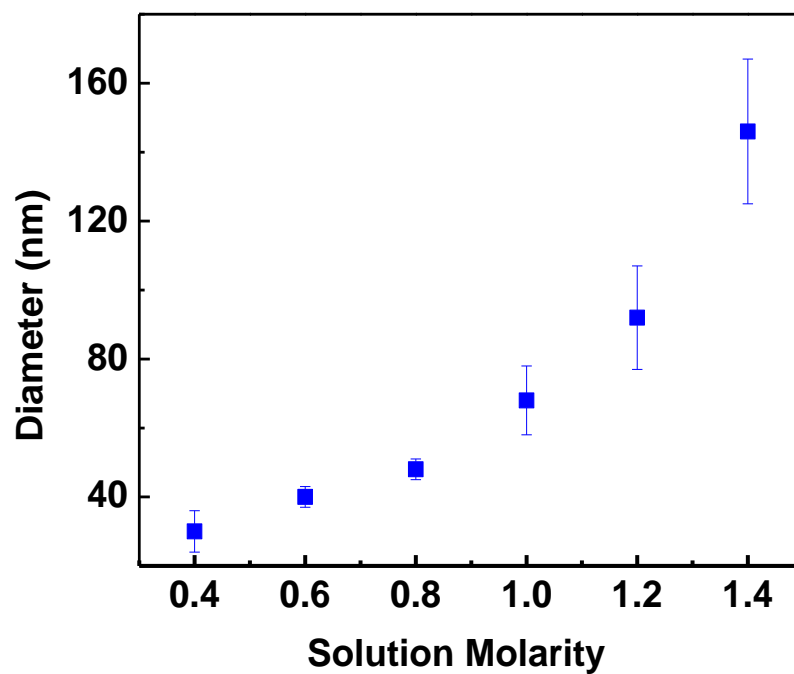


Figure 7.7 Nanofibers diameter as a function of precursor solution concentration.

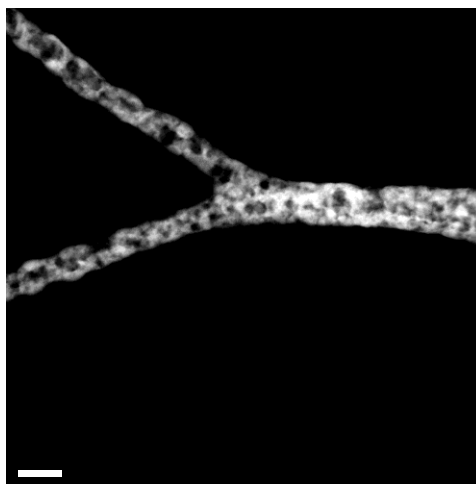


Figure 7.8 High resolution transmission electron microscope (HRTEM) image of a joint BFO nanofibers with high solution concentration.

7.3.3.1 Grain size

As previously mentioned electrospun nanofiber consisted of nanograins. The physical and chemical properties of the nanofibers could be co-related with the size of nanograins. In this study the grain size as a function of nanofiber diameter was measured with the TEM and the results are shown in Figure 7.9. The grain size increases sharply up to 60 nm nanofibers diameter and then saturates at higher diameter. There are approximately seven nanograins in a nanofiber with 40 nm diameter.

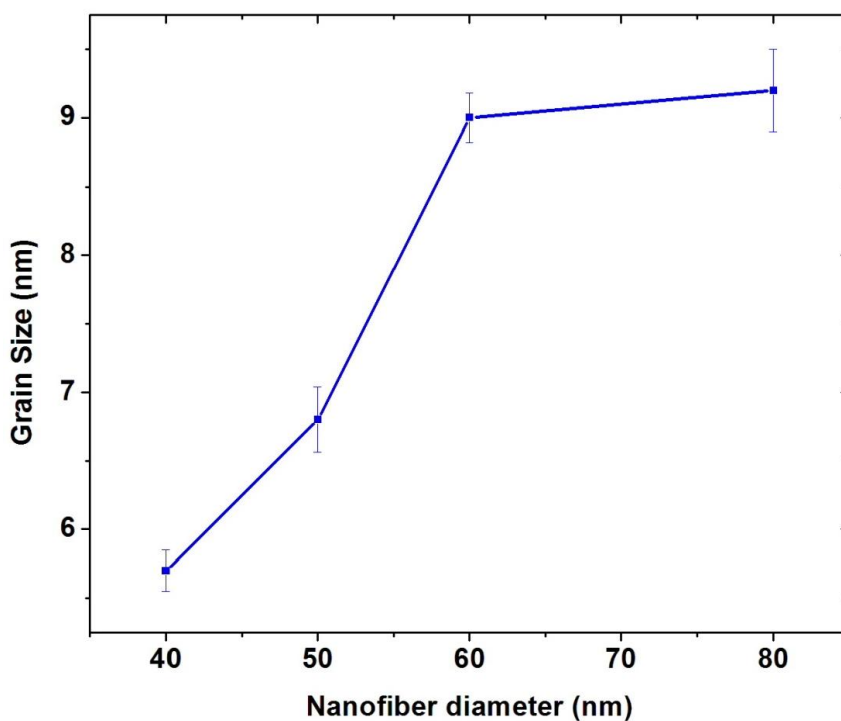


Figure 7.9 Average grain size as a function of fiber diameter obtained from TEM.

7.3.3.2 Iron valence state

Iron valence state is an important feature in BFO system because it influences the electrical properties of nanofibers. Electron Energy Loss Spectroscopy (EELS) experiment was performed on individual nanofibers of different diameters to determine the valence state of iron. The results in Figure 7.10 show that nanofibers with smaller diameter (40 nm) are composed mostly of Fe^{3+} valence state while nanofibers with larger diameters (80 nm) are mostly composed of Fe^{2+} valence. The valence state of Fe (3+ and 2+) of the nanofibers with diameter in between the two extreme value have a combination of Fe^{2+} and Fe^{3+} . For nanostructures, it is energetically unfavorable to create defects in the core of the particles, then possible surface impurities of nanostructure may have effect on the variation of valence state¹². The observation of valence state fluctuation can be due to reduced coordination number of the atoms at the surface of the BFO nanofibers due to reduced grain size (Figure 7.9). If considering a reduced coordination number, the electron density around Fe^{3+} ions on the surface of the nanofibers would be less and hence the shielding of the iron nucleus is decreased causing the electrons to be pulled closer¹². Another reason behind the observation of iron valence fluctuation can be due organic polymer removal stage. In the process of polymer burn out, organic binders are thermally removed before completing crystallization. For the incomplete burn out, the trapped organic residues will be a contamination source and affects the oxidation of the final sample. On the other hand, if the burn out is carried hastily; defects in the green samples will form. Considering, different various diameter of the nanofibers, larger amount of organic polymer must be removed from nanofibers with larger diameters¹³.

When removing the organic polymer, oxygen defects maybe created in which inducing charge balance compensation (Fe^{3+} to Fe^{2+}).

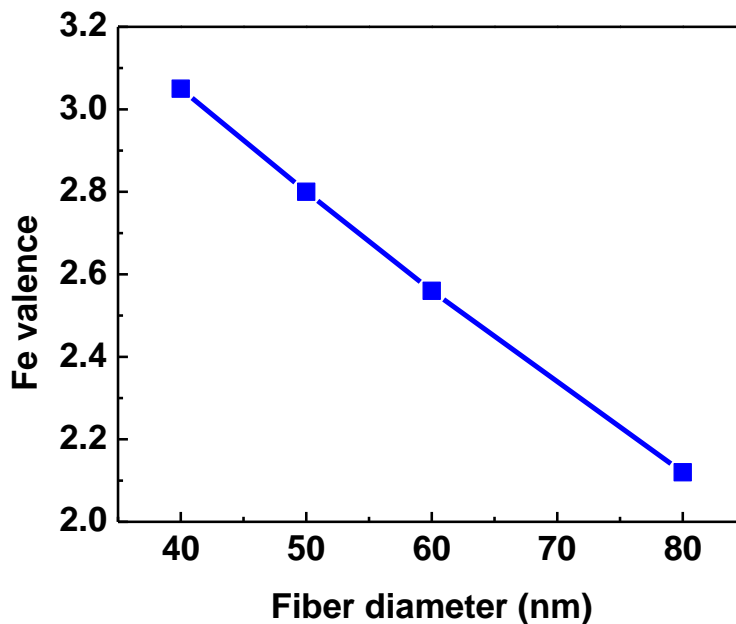


Figure 7.10 Fe valence state as a function of fiber diameter obtained from EELS analysis.

7.3.3.3 Chemical composition

Rutherford Backscattering Spectrometry (**RBS**) results for BFO nanofibers mat of 1.0, 0.8, and 0.6 M corresponding to different average diameters are shown in Figure 7.11 to 7.13. The peaks for Bi and Fe are clearly indentified in the RBS spectra. The simulated data is well fitted to the experimental results for nanofibers different diameter. The RBS results indicate that the nanofibers, within the detection limit are free of impurities. The composition derived from the simulation was found to be more deficient in iron compare to stoichiometric composition (BiFeO_3), especially for nanofibers prepared with high molarity.

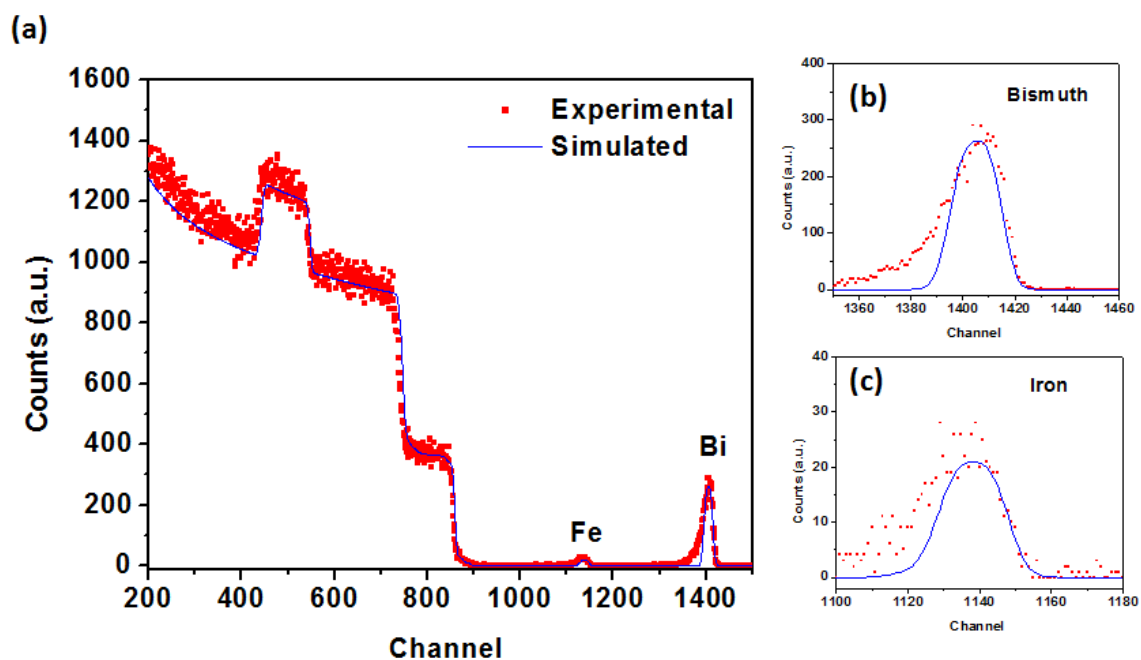


Figure 7.11 Rutherford backscattering spectrometry results for 1.0 M (80 to 100 nm in diameter) BFO multiple-nanofibers.

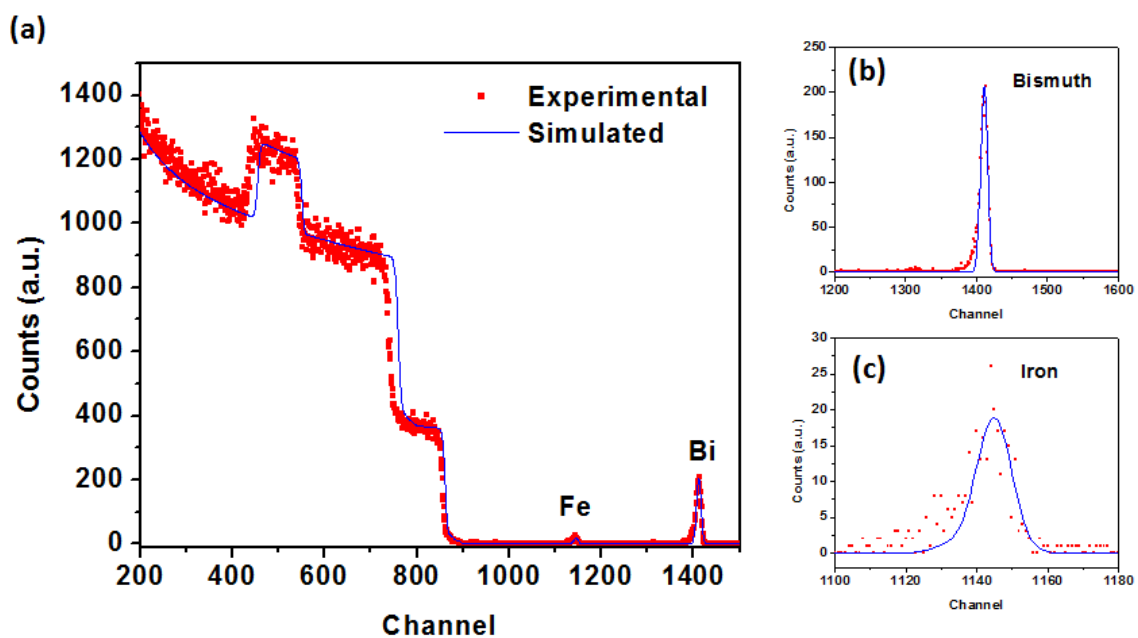


Figure 7.12 Rutherford backscattering spectrometry results for 0.8 M (50 to 70 nm in diameter) BFO multiple-nanofibers.

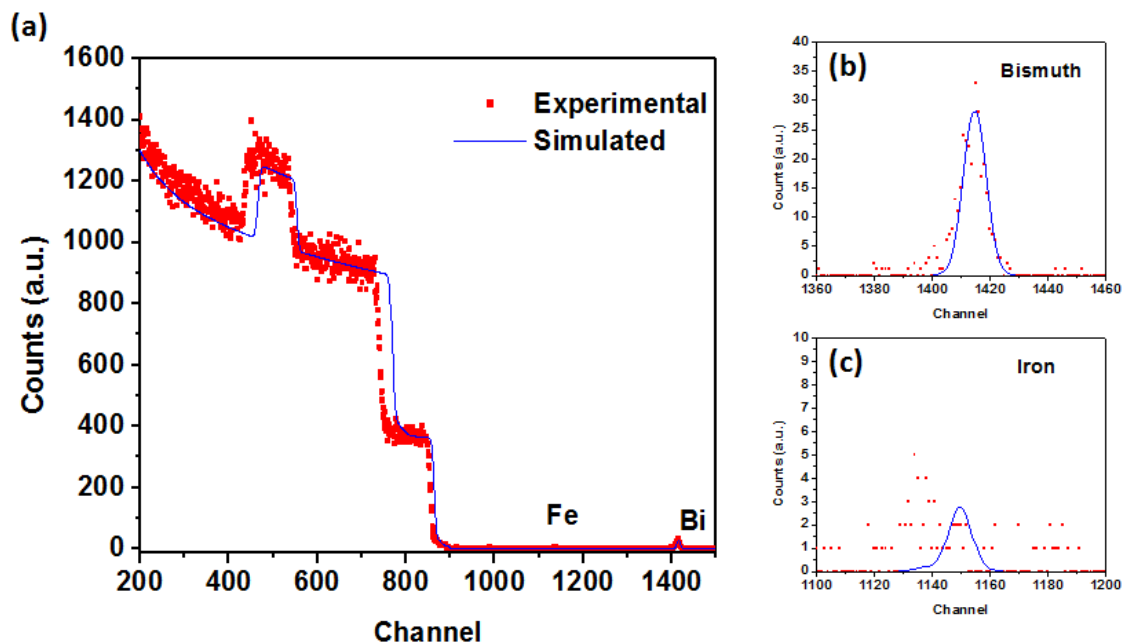


Figure 7.13 Rutherford backscattering spectrometry results for 0.6 M (30 to 50 nm in diameter) BFO multiple-nanofibers.

Table 7.5 Chemical composition for BFO multiple-nanofibers (mat)

1.0 M	$\text{Bi}_{0.85}\text{Fe}_{0.78}\text{O}_x$
0.8 M	$\text{Bi}_{0.92}\text{Fe}_{0.82}\text{O}_x$
0.6 M	$\text{Bi}_{0.96}\text{Fe}_{0.88}\text{O}_x$

7.4 Electrical properties of BFO nanofibers

7.4.1 Current vs Voltage characteristics for single nanofibers

The electronic behavior of BFO nanofibers have been studied as a function of nanofiber diameter. Samples of BFO nanofibers with different diameter were prepared as explained in Section 7.3. The nanofibers were deposited on SiO_2/Si substrate, polymer was removed, and finally the nanofibers were crystallized at 550°C for 2 hours. Optical microscope was used to locate single nanofibers with respect to the pre-defined markers. Metallic contacts were designed for individual nanofibers. The contacts, consisting of 10 nm Ti and 50 nm Au, were deposited through e-beam lithography. The electrodes distance varied between $3.0\text{ }\mu\text{m}$ to $20\text{ }\mu\text{m}$ depending on the location of the individual nanofibers and electrode design. A single nanofiber was contacted in four different locations as shown in Figure 7.14 (same was done for different samples). The diameter and electrode distance between each metal contact was measured through SEM.

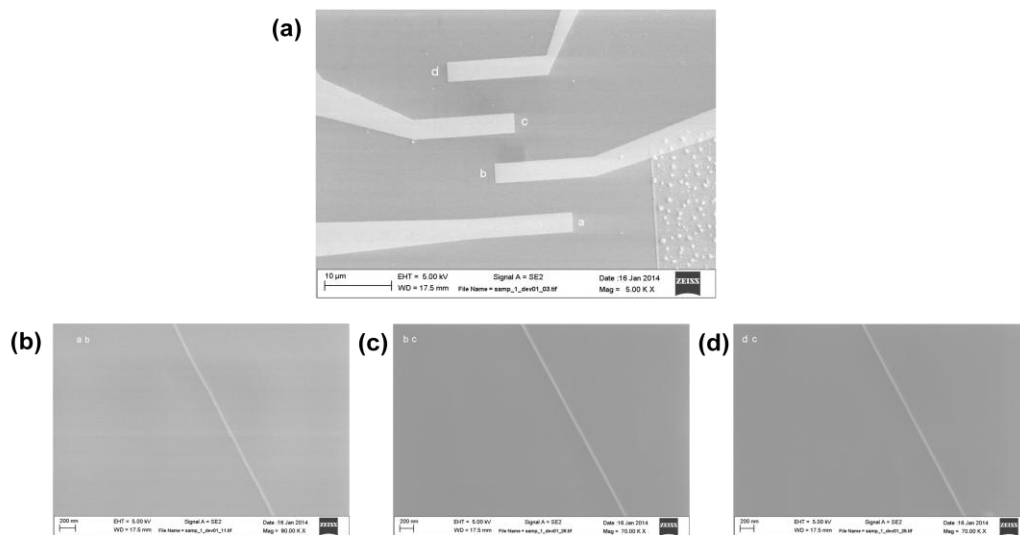


Figure 7.14 SEM surface images for BFO single nanofiber (a) top view of metal electrode, (b-d) zoom in image of the nanofiber between each metal electrode

The current vs voltage (I - V) measurements were made using two-probe method using a *HP-Agilent* source meter. Voltage was applied between the two gold electrodes and current passing between them was measured as a function of applied voltage. I - V characteristic were plot for each nanofiber with various diameters and results are shown in Figure 7.15. Current was normalized as function of the electrodes length. I / V characteristics for all diameters exhibited a non-linear behavior. The current flow increases as a function of nanofiber diameter. Similar conductivity dependent with diameter has been reported for different materials such as GaN^{14,15}.

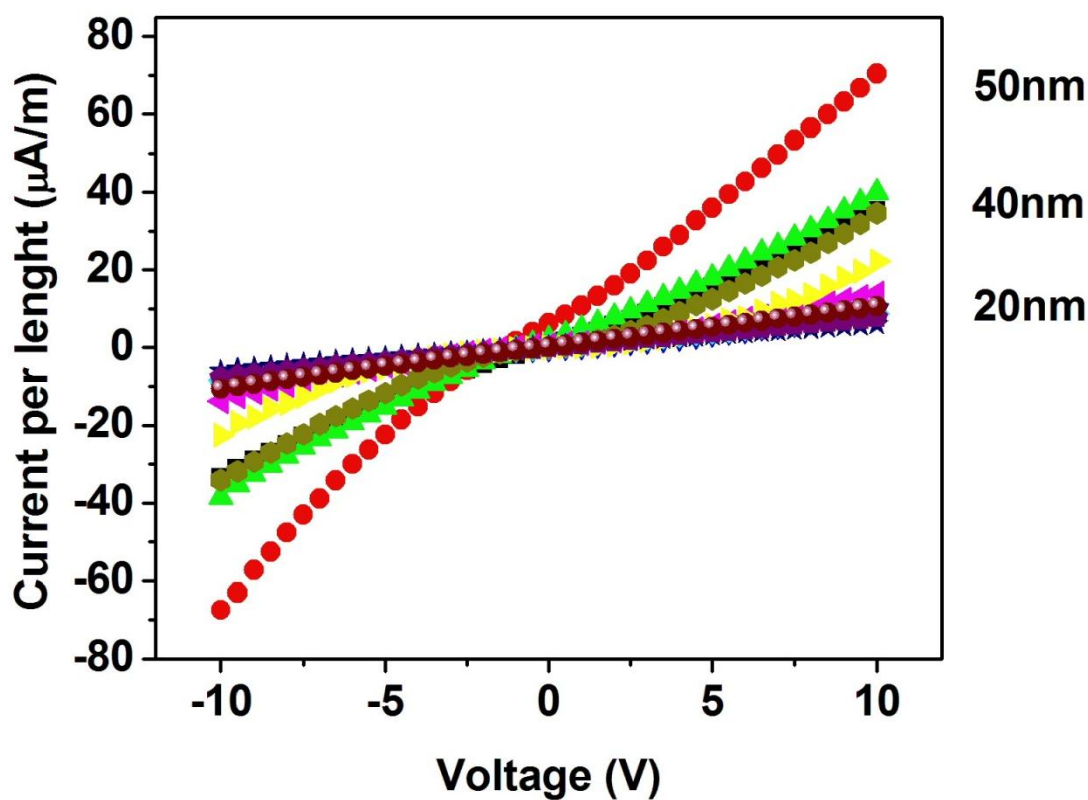


Figure 7.15 Current vs Voltage for single nanofibers of different diameters at RT.

7.4.2 Size dependent on the photoconductivity of multiple-nanofibers

The photoconductivity of bismuth ferrite nanofibers mats with different average diameters was studied. The electrical measurements was carry out using a two-probe system and a *HP-Agilent* source meter and a solar simulator with AM 1.5 spectra output was chosen as the light source. To study the photoresponse a constant voltage (10V) was applied and the variation in the current was measured upon illumination of the fibers to light (Figure 7.16).

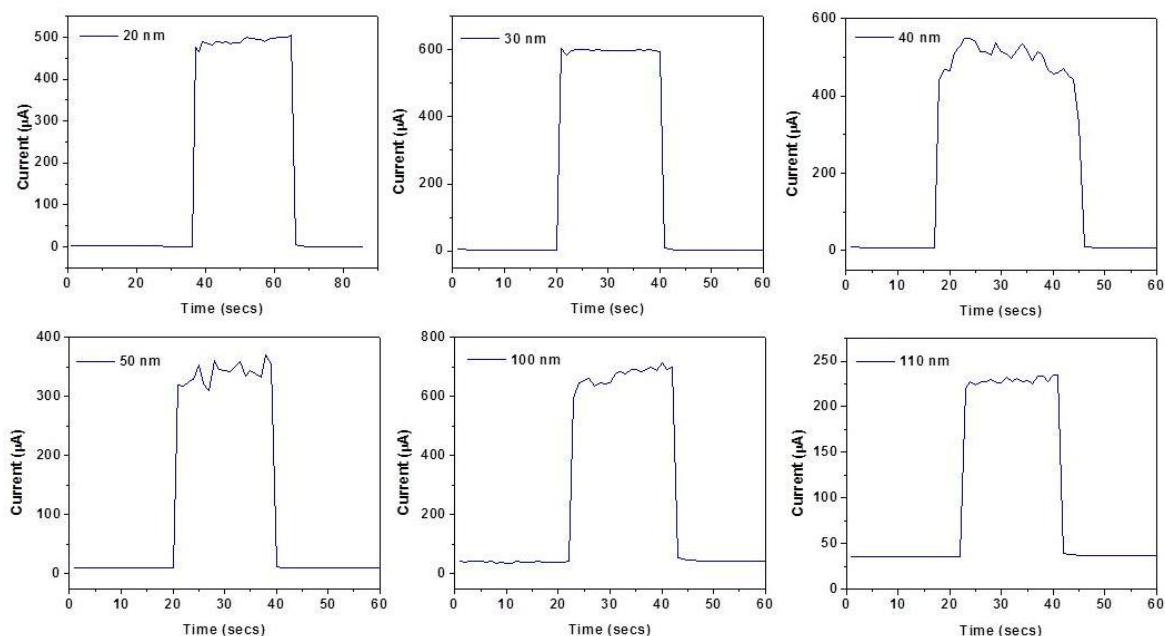


Figure 7.16 Current vs time at constant voltage (10V) upon illumination

The ratio of the current when the light is ON to the current when the light is OFF (photoconductivity) was calculated for different diameters and shown in Figure 7.17. Nanofibers with smaller diameter exhibited higher sensitivity to light compared to nanofibers with larger diameter. The photoconductivity response for nanofibers around 20 nm in diameter was found to be four hundred times higher than for nanofibers of 110 nm diameter. For diameters below 50 nm a sharp increase in the photoresponse is observed, while for nanofibers above 50 nm the On/Off ratio remains constant. Similar trend in photocunductivity for thinner and thicker nanofibers of GaN nanowires was reported¹⁶.

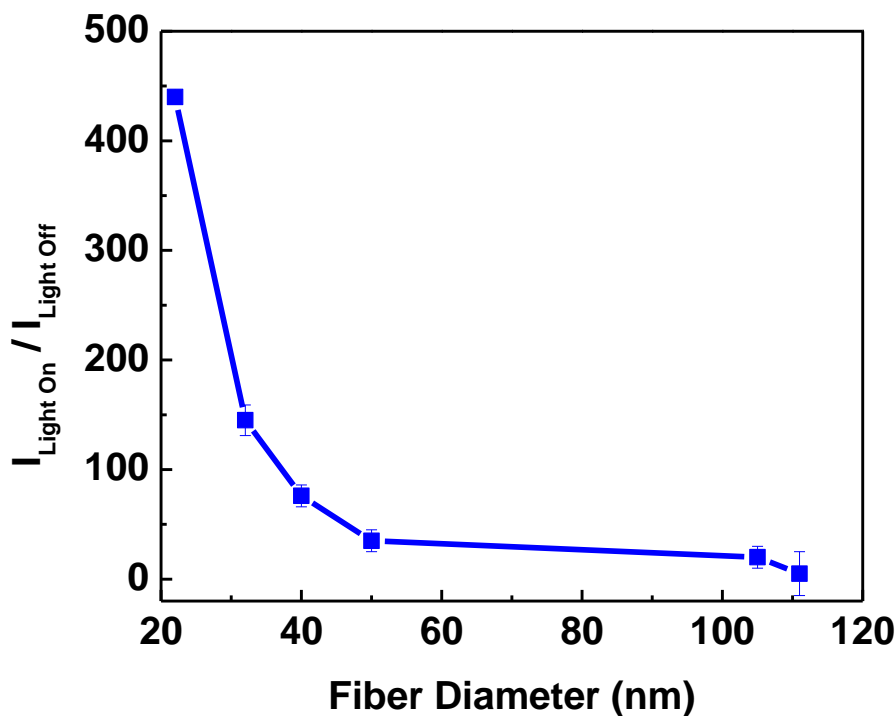


Figure 7.17 On/Off ratio for a multiple-nanofibers mat as a function of average diameter

The Figure 7.18 shows the nanofiber diameter in relationship with the On/Off ratio, grain size, and the iron valence state. Higher On/Off ratios are obtained for fiber with smaller grain size (smaller diameter) and higher content of Fe^{3+} .

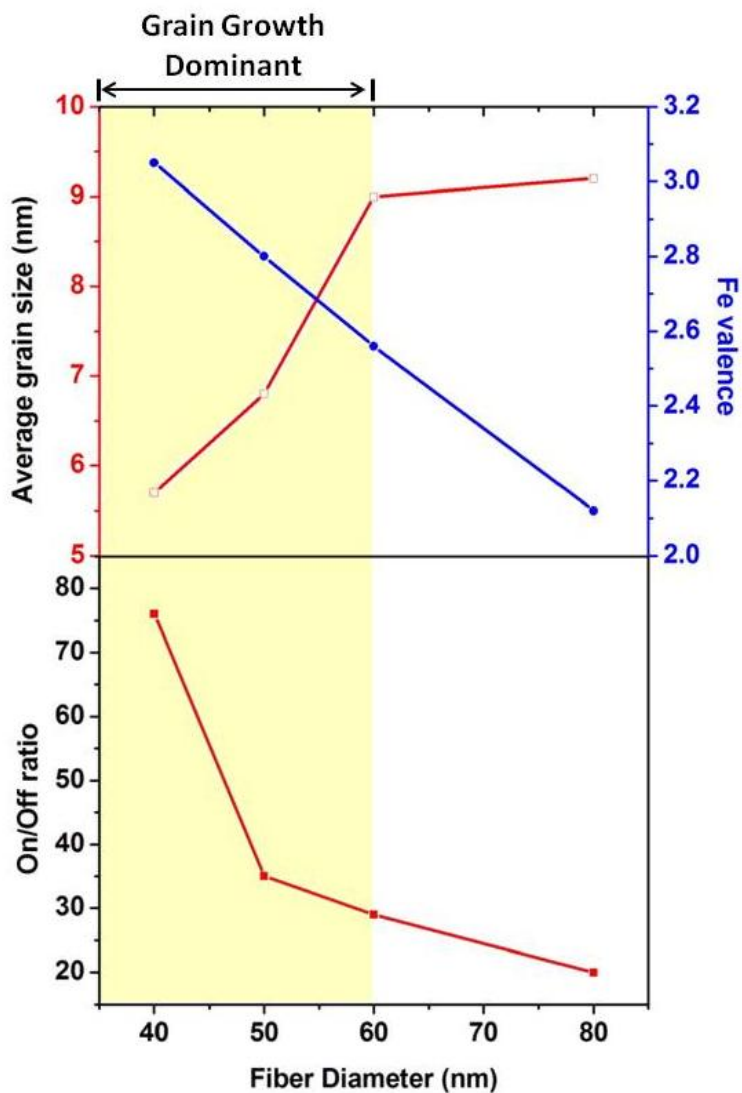


Figure 7.18 Plot of the On/Off ratio in comparison with BFO grain size and Fe state for single nanofibers

Wide band gap materials such as BFO possess high density of surface states within the band gap¹⁷. The density of surface states does not influence the optical properties of bulk materials and thin films; however effectively dominate in one-dimensional nanostructures due to large surface to volume ratios. The presence of surface states in the band gap is known to pin the Fermi level position in the semiconductor^{16,18}. Therefore, photons having energy lower than the band gap can be absorbed by the surface states as a result of faster availability of electronic transitions. Considering the high surface-volume ratio of the BFO nanofibers, sub-band transitions become dominant for optical absorption. In the bulk or thin films, the principal behind the reported photovoltaic effect is the internally generated electric field originated from the ferroelectric domains^{19,20}. Such internal generated electric field is responsible for the separation of photogenerated carriers on BFO nanofibers. Considering the nanostructure nature of BFO in this research, in addition to the ferroelectric polarization, there is a significant contribution of the surface potential.

Due to the Fermi level pinning within the forbidden band, semiconductor nanofibers exhibit a depletion space charge layer with the extension of the order of the nanofiber diameter. Conditional to the nanofiber diameter, completely depleted nanofibers or nanofibers with conducting channels exists. The energy bands at the surface of BFO nanofibers are bent due to trapped charges or surface defects, thus the resulting surface potential can separated the photogenerated charge carriers¹⁸.

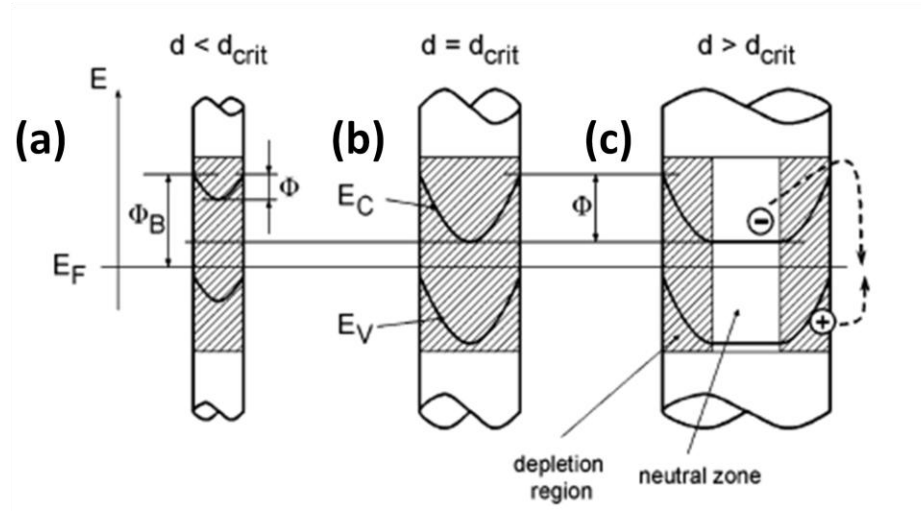


Figure 7.19 Band diagram for different nanofibers diameter. (a-b) completely depleted, and (c) thin channel exists. **NOTE:** Image have been copied from ¹⁶

In Figure 7.19c electrons are in the inner part of the “channel” while holes preferred to move to the surface. Because of the spatial separation, recombination of these carriers is reduced, taking into account the recombination via surface traps. Electrons need to overcome the conduction band barrier at the surface for recombination. A decrease in the diameter leads to complete depletion (Figure 7.19b) with unchanged surface barrier height for electrons in the conduction band. The recombination rate change slightly at the critical diameter. Further decreasing in the diameter (Figure 7.19a) causes less band bending and therefore reduction in the surface barrier for electron-hole recombination. From the On/Off ratio in Figure 7.17 is confirmed that decreasing the diameter of BFO nanofibers below a critical point results in strongly enhanced photoresponse.

7.5 Bismuth ferrite field effect transistor devices with single nanofiber and multiple-nanofibers

Bismuth ferrite nanofibers of ~ 50 nm diameter were prepared from a 0.6 M precursor solution, deposited on SiO_2/Si substrates, and crystallized at 550°C . Using the optical microscope, areas with single nanofibers and multiple-nanofibers were located in different samples for device fabrication. The contacts, consisting of (1) 10 nm Ti/50 nm Au, (2) 20 nm Al_2O_3 , and (3) 10 nm Ti and 50 nm Au were deposited through e-beam lithography. The aluminum oxide layer is used as top dielectric which will create an isolated top gate electrode for the device. A schematic of the final top gate device architecture is shown in Figure 7.20.

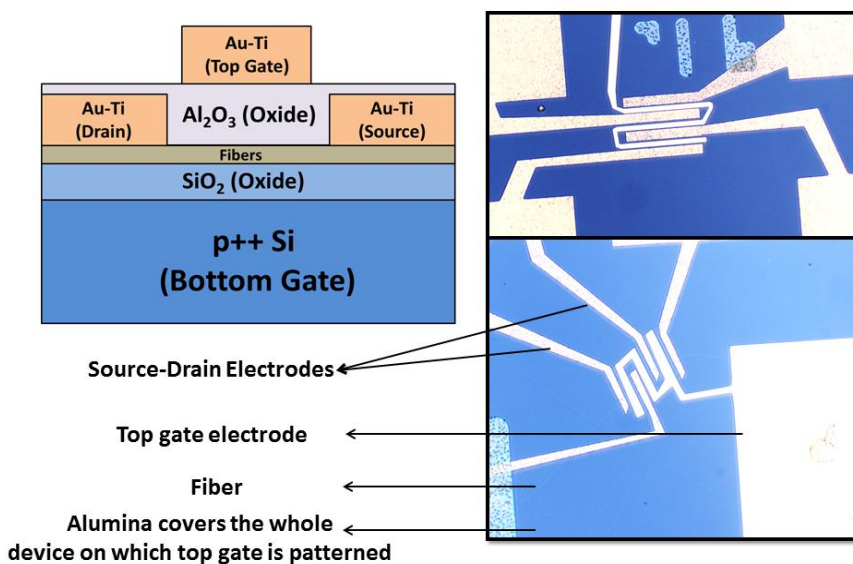


Figure 7.20 (a) Schematic of device fabrication for BFO nanofiber field effect transistor (FET). In the case of a single nanofiber device there is only one fiber between drain and source contacts. For a multiple-nanofibers device there are about ten nanofibers between drain and source contacts.

Figure 7.21 shows the transfer characteristic curve for a BFO-single nanofiber and multiple-nanofiber device. The FET was measured on top contact configuration in which the drain and source are deposited right on top of the active layer (BFO) nanofiber. A voltage is applied to the gate (V_g) that is sufficiently large to induce a conducting channel. Simultaneously a fixed voltage in the drain (V_d) is applied so that the current from drain to source (I_{ds}) begins to flow through the induced channel and is high enough to measure the flowing current. The V_g is applied in both negative and positive directions to determine if the device behaves as a p-type or n-type channel. A negative V_g resulted in an increase in I_{ds} .

The transfer characteristics in both cases exhibit a p-type channel behavior. The field effect transistor mobility (μ_{FET}) and the threshold voltage (V_{TH}) were calculated from the transfer characteristic curve in the linear operation region of a MOSFET expressed as^{17,21},

$$I_{DS} = \mu_{FET} C_{ox} \frac{W}{L} \left[(V_{GS} - V_{TH}) V_{DS} - \frac{V_{DS}^2}{2} \right] \quad (7.1)$$

The formula to calculate the mobility is obtained by taking the first order derivative of the Equation 7.1 with respect to V_{DS} .

$$\mu_{FET} = \frac{g_m L}{W C_{ox} V_D} \quad (7.2)$$

Where, L and W are the length and width of the channel (equivalent to the nanofiber diameter), and C_{ox} is capacitance per unit area of the dielectric layer (Al_2O_3), V_D is the voltage applied to the drain, and g_m is the transconductance.

$$g_m = \frac{\partial I_{DS}}{\partial V_{GS}} \quad (7.3)$$

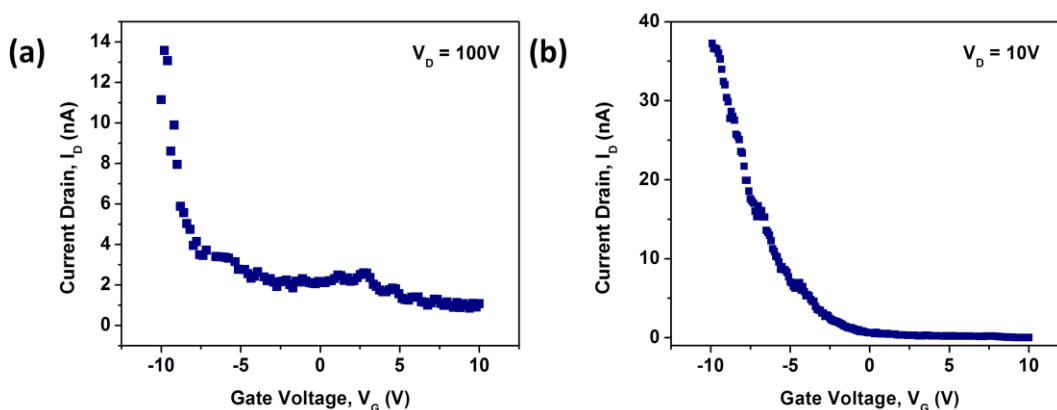


Figure 7.21 Field effect transistor device **transfer** characteristic for (a) single-nanofiber device, and (b) multiple-nanofiber device.

The carrier mobility for single-nanofiber and multiple-nanofiber devices was calculated to be as 0.2 and 0.25 $\text{cm}^2/\text{V.s}$ respectively. However, it is important to note that the required operating voltage for the different devices. Single nanofiber required an operating voltage of 100V while multiple-nanofiber device required only 10V.

The On/Off ratio of the devices is the ratio when the devices saturates for a given applied gate voltage to that of the value when no gate voltage is applied. The On/Off ratio for a multiple-nanofiber is ~ 60 . The ON current for a single-nanofiber and multiple-nanofiber device at $V_{GS} = -10V$ is in the range of 15 and 35 nA respectively. It should be point that this On/Off ratio is not related to photoconductivity but related to the devices On and Off operation (switch ON and OFF)

To further confirm the field effect transistor (FET) behavior nanofibers, different values of V_g are applied to control the conductivity in the channel. Figure 7.22 shows output characteristics of a BFO single-nanofiber and multiple-nanofiber FET device. The non-linear I_D - V_D curve with pinch off behavior indicates that the device works as a FET.

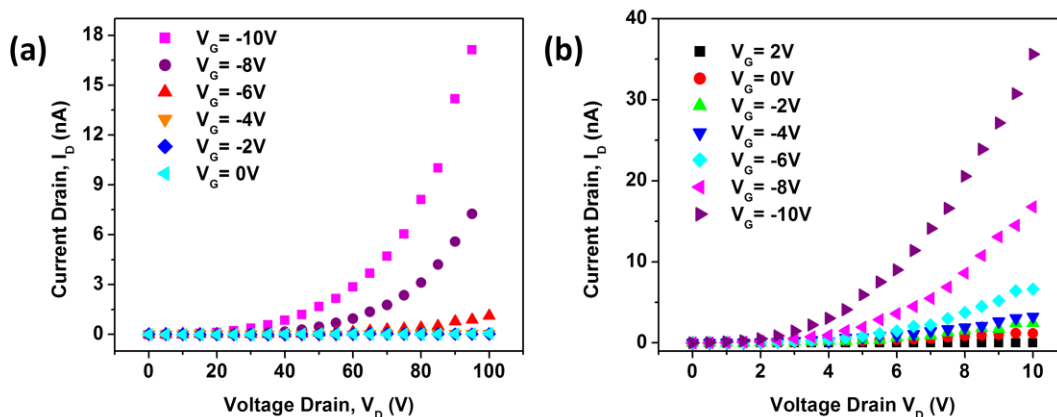


Figure 7.22 Field effect transistor device **output** characteristic for (a) single-nanofiber device, and (b) multiple-nanofiber device.

In general, the electronic properties of semiconductor nanofibers depend on its diameter. Nevertheless, the relationship between the nano-dimensions and properties is very complex, thus required careful experiments and deeper understanding. An experimental difficulty is that studying the effects of different diameters requires comparisons of individual nanofibers of one batch of precursor solution. Such comparison relies on the assumption that the different growth conditions (different batches) do not affect electronic properties nanofibers.

7.6 Summary

Bismuth ferrite nanofibers with excellent surface morphology have been fabricated by electrospinning technique. Nanofibers with controlled diameter were achieved by varying the precursor solution concentration. Bead free- nanofibers with diameter in a range of 20 - 110 nm were obtained. XRD, complementary Raman spectroscopy and TEM results show that BFO nanofibers have pure perovskite phase with rhombohedral structure. The grain size decreased sharply for nanofibers below 60 nm in diameter. The nanofibers are mostly a combination of Fe valence state, thinner nanofiber (20 nm) favored Fe^{3+} while thicker nanofibers are most likely Fe^{2+} .

The electrical properties of BFO nanofibers exhibited a diameter dependent which could be correlated to the grain size. Larger diameter resulted in higher current levels but lower electron-hole recombination in the photoconductivity process. BFO single and multiple nanofiber field effect transistors devices exhibited a p-type semiconductor behavior. The carrier mobility for both devices is $\sim 0.20\text{cm}^2/\text{V.s.}$ while the operating voltage for multiple-nanofibers devices is greatly reduced from 100 V to 10 V compared to single nanofiber device.

One dimensional BFO nanofibers are emerging as promising candidate for photoconduction and photovoltaic applications due to the strong light absorption which are result of large surface areas and direct charge transport along the geometry of the nanofibers.

7.7 References

1. Baji, A. *et al.* One-dimensional multiferroic bismuth ferrite fibers obtained by electrospinning techniques. *Nanotechnology* **22**, 235702 (2011).
2. Li, D. & Xia, Y. Electrospinning of Nanofibers: Reinventing the Wheel? *Adv. Mater.* **16**, 1151–1170 (2004).
3. Ziabari, M., Mottaghitalab, V. & Haghi, A. K. A new approach for optimization of electrospun nanofiber formation process. *Korean J. Chem. Eng.* **27**, 340–354 (2010).
4. Doshi, J. & Reneker, D. H. Electrospinning process and applications of electrospun fibers. *J. Electrostat.* **35**, 151–160 (1995).
5. Fong, H. & Reneker, D. H. in *Structure formation in polymeric fibers* **6**, (2001).
6. Tan, S.-H., Inai, R., Kotaki, M. & Ramakrishna, S. Systematic parameter study for ultra-fine fiber fabrication via electrospinning process. *Polymer* **46**, 6128–6134 (2005).
7. Deitzel, J. M., Kleinmeyer, J., Harris, D. & Beck Tan, N. C. The effect of processing variables on the morphology of electrospun nanofibers and textiles. *Polymer* **42**, 261–272 (2001).
8. Fukumura, H. *et al.* Raman scattering study of multiferroic BiFeO₃ single crystal. *J. Magn. Magn. Mater.* **310**, e367–e369 (2007).
9. Palai, R. *et al.* β phase and γ - β metal-insulator transition in multiferroic BiFeO₃. *Phys. Rev. B* **77**, (2008).
10. Singh, M. K., Jang, H. M., Ryu, S. & Jo, M.-H. Polarized Raman scattering of multiferroic BiFeO₃ epitaxial films with rhombohedral R3c symmetry. *Appl. Phys. Lett.* **88**, 042907 (2006).
11. Da-Ren Chen, D. Y. H. P. Electrospaying of conducting liquids for monodisperse aerosol generation in the 4 nm to 1.8 μ m diameter range. *J. Aerosol Sci.* 963–977 (1995). doi:10.1016/0021-8502(95)00027-A
12. Jaiswal, A. *et al.* Effect of Reduced Particle Size on the Magnetic Properties of Chemically Synthesized BiFeO₃ Nanocrystals. *J. Phys. Chem. C* **114**, 2108–2115 (2010).
13. Tsai, D.-S. Pressure buildup and internal stresses during binder burnout: Numerical analysis. *AIChE J.* **37**, 547 – 554 (2004).
14. Hou, J. J. *et al.* Diameter dependence of electron mobility in InGaAs nanowires. *Appl. Phys. Lett.* **102**, 093112 (2013).
15. Scheffler, M., Nadj-Perge, S., Kouwenhoven, L. P., Borgström, M. T. & Bakkers, E. P. A. M. Diameter-dependent conductance of InAs nanowires. *J. Appl. Phys.* **106**, 124303 (2009).
16. Calarco, R. *et al.* Size-dependent Photoconductivity in MBE-Grown GaN–Nanowires. *Nano Lett.* **5**, 981–984 (2005).
17. Neamen, D. A. *Semiconductor Physics And Devices: Basic Principles*. (McGraw-Hill, 2011).
18. Prashanthi, K., Gaikwad, R. & Thundat, T. Surface dominant photoresponse of multiferroic BiFeO₃ nanowires under sub-bandgap illumination. *Nanotechnology* **24**, 505710 (2013).
19. Alexe, M. & Hesse, D. Tip-enhanced photovoltaic effects in bismuth ferrite. *Nat. Commun.* **2**, 256 (2011).

20. Choi, T., Lee, S., Choi, Y. J., Kiryukhin, V. & Cheong, S.-W. Switchable ferroelectric diode and photovoltaic effect in BiFeO₃. *Science* **324**, 63–66 (2009).
21. MOSFET and Metal Oxide Semiconductor Tutorial. *Basic Electronics Tutorials* at <http://www.electronics-tutorials.ws/transistor/tran_6.html>

8 Summary and Conclusions

In this thesis, fabrication and ferroelectric properties, leakage current, photoconductor behavior, and transistor performance of the lead free multiferroic bismuth ferrite-BiFeO₃ based thin films and nanofibers were investigated. Thin films were fabricated by sol-gel solution and pulsed laser deposition (PLD) methods. Nanofibers were fabricated by electrospinning of sol-gel solutions.

The optimum deposition conditions for BiFe_{1-x}Mn_xO₃ (x=0.00 to 0.15) thin films by sol-gel are as follow: spin coating at 3000 rpm for 30 seconds, pyrolysis at 200 °C for 2 minutes, and heat treatment at 550 °C for 10 minutes.

Epitaxial (100) oriented thin films of 0.6BiFeO₃-0.4(Bi_{0.5}K_{0.5})TiO₃ were prepared by PLD under different oxygen background pressure of 300, 400, and 500 mTorr, 10 Hz laser fluency, 800 °C substrate temperature, and 170 mJ laser energy. Under similar deposition method, bi-layered epitaxial (100) oriented thin films with targets compositions of 0.88(Bi_{0.5}Na_{0.5})TiO₃ -0.08(Bi_{0.5}K_{0.5})TiO₃-0.04BaTiO₃ (BNT-BKT-BT) and BiFeO₃ were deposited on SrRuO₃ coated SrTiO₃ substrate. In this investigation, first, BNT-BKT-BT film with thickness of 150 nm, was deposited with following deposition parameters: substrate temperature 800 °C, oxygen partial pressure 400 mTorr, laser energy 170 mJ, laser repetition rate 10 Hz. In second step, BFO thin film with thickness of 150 nm was deposited on top of the BNT-BKT-BT layer with following deposition parameters: substrate temperature of 750 °C, 20 mTorr oxygen pressure, 170 mJ laser energy, and 10 Hz laser repetition.

BFO based nanofibers were fabricated by electrospinning technique and nanofibers morphology, structure, and electrical behavior were studied for possible high power electronics devices applications. The optimized electrospinning processing conditions for the deposition of pure BFO nanofibers with an excellent morphology, free of beads, smooth, and uniform surface are: 0.2 ml/hr flow rate, 10 kV driving voltage, and 20 cm separation between the needle tip and collector.

Detailed conclusions were drawn from the numerous experiments carried out on BFO thin films and nanofibers which are presented as follows:

A) Bismuth ferrite thin films by sol gel

- BFO-Mn thin films exhibited pure perovskite structure up to 15 mol% Mn doped.
- The films structure go through a transition from rhombohedral to tetragonal when Mn increased above 5%
- The surface microstructure for higher Mn content resulted in pillar growth.
- The leakage current of 5% Mn doped BFO films two orders of magnitude suppressed.

B) $0.6\text{BiFeO}_3\text{-}0.4(\text{Bi}_{0.5}\text{K}_{0.5})\text{TiO}_3$ thin films by pulsed laser deposition

- Films deposited at different oxygen partial pressure show a pure perovskite structure with no impurities.
- The films grown under 300 mTorr exhibited a Bi/Fe ratio very close to the target composition. Surface morphology of the films is dense, uniform and pinhole or crack free.
- The leakage current of the films grown at 300 mTorr was $10^{-4} \text{ A.cm}^{-2}$ at 200 kV.cm^{-1} which is suppressed by four orders of magnitudes compared to the films grown at 500 mTorr oxygen partial pressure.
- The optimum electrical and ferroelectric properties are as: Oxygen Pressure 300 mTorr, $P_r = 16.6 \mu\text{C.cm}^{-2}$, $E_C = 100 \text{ kV.cm}^{-1}$, and $J_{sc} = 1 \times 10^{-4} (\text{A.cm}^{-2})$ at 200 kV.cm^{-1} , and $\epsilon_r = 400$ at 1 kHz.

C) $0.88(\text{Bi}_{0.5}\text{Na}_{0.5})\text{TiO}_3\text{-}0.08(\text{Bi}_{0.5}\text{K}_{0.5})\text{TiO}_3\text{-}0.04\text{BaTiO}_3/\text{BiFeO}_3$ bi-layered thin films by pulsed laser deposition

- The BNT-BKT-BT/BFO bi-layered thin films exhibited a pure perovskite phase.
- The surface morphology of the top layer (BFO) shows a pillar type growth.
- Films exhibited remnant polarization values of $22.0 \mu\text{C.cm}^{-2}$, $E_C = 100 \text{ kV.cm}^{-1}$, and $\epsilon_r = 140$ at 1 kHz.
- The leakage current of the bi-layered film was $10^{-3} \text{ A.cm}^{-2}$, which is three orders of magnitudes lower than un-doped BFO films.

D) Bismuth ferrite nanofibers by electrospinning

- The nanofibers diameter was well controlled with the precursor solution concentration, in a range of 20 to 110 nm.
- Iron valence state was found to vary with nanofiber diameter which could be related to the shell/core ratio or organic polymer removal.
- EELS experiments revealed that iron valence state for a 20 nm nanofiber was mostly 3^+ while iron valence state for nanofibers with larger diameter (80 nm or thinner) was mostly 2^+ . However, the iron valence state for nanofibers in a range of 20-80 nm in diameter are a combination of 3^+ and 2^+ which was confirmed by TEM and XPS.
- The I - V increases from 10 to 80 nA for single BFO nanofibers with diameters of 20 and 50 nm respectively.
- The photoresponse (I - t) upon illumination, for nanofibers mat was dependent on the nanofiber average diameter. For samples with nanofibers of ± 20 nm, the Light On/Light Off ratio was four hundred times higher than of nanofibers with ± 100 nm diameter.
- The BFO nanofiber field effect transistor devices exhibited a p-type semiconductor behavior, and the conduction channel is well controlled. The device is OFF for $V_{GS} > 0V$ and it is switched ON for $V_{GS} < 0V$.
- The device carrier mobility is found to be as 0.20 to 0.25 $\text{cm}^2/\text{V.s}$ for multiple and single nanofiber FET respectively. However, the required operating voltage for a single nanofiber is 100V while for a multiple-nanofiber is 10V.

According to the obtained results in this thesis, it can be concluded that lead free multiferroic bismuth ferrite binary system and bi-layered thin film could be utilized in for memory applications. Bismuth ferrite as mid band gap semiconductor in the form of nanofibers is a potential candidate for photoconduction applications and high power electronic devices.

9 Suggestions for Future Work

Bismuth ferrite and its multiferroic properties have been extensively studied in the form of thin films through many years. However, its multiferroic origin still is not well understood and more research needs to be done in this area. The development of BFO in one dimensional structure is at its early stage. Most of the work being done in BFO nanofibers attempts to enhance the ferromagnetic behavior. It has been found that the multiferroic properties of BFO are size and structural dependent. The weak spiral spin structure and antiferromagnetic ordering can be suppressed and high magnetoelectric coupling may be observed if the size of the nanostructure is less than the spiral periodicity (62 nm). Considering the ferroelectric-semiconductor multi-functionality of BFO, novel applications in the field of optoelectronics are being studied recently.

In this section few suggestions are made to conduct research in the area of BFO thin films and nanofibers as continuation of the presented work.

E) Bismuth ferrite thin films

1. Improve the surface quality of BFO thin films by lowering the deposition temperature and/or increasing the oxygen partial pressure by PLD. Characterize the thin films (PLD and sol-gel) electromechanical properties at low temperature and/or high frequency.
2. Considering that the development of BFO-BKT thin films is not being extensively studied by others group, further experiments could be revealing. Deposition of BFO-BKT thin films by PLD at lower oxygen pressure and investigation of better ferroelectric properties are achievable.

F) Bismuth ferrite nanofibers

1. Characterize the multiferroic properties of BFO: single nanofibers, nanofibers mat, and aligned nanofibers using piezo-atomic force microscopy.
2. The carrier mobility in nanostructures becomes size dependent when the size is reduced below the excitation Bohr atom radius. Fabrication of nanostructures below such radius to obtain higher carrier mobility on transistor devices.
3. Investigate the photo-catalytic behavior of nanofibers.
4. Fabrication of BFO based solar cell.
5. Fabrication and characterization of other lead free piezoelectric materials such as BNT, BKT, BT and combination of them.